BIOLOGICAL REDESIGN OF VIRUS PARTICLES FOR A NEW ERA OF CATALYTIC MATERIALS

by

Paul Campion Jordan

A dissertation submitted in partial fulfillment
of the requirements for the degree

of

Doctor of Philosophy

in

Biochemistry

MONTANA STATE UNIVERSITY
Bozeman, Montana

December 2015

TABLE OF CONTENTS

TABLE OF CONTENTS – CONTINUED

TABLE OF CONTENTS – CONTINUED

LIST OF FIGURES

Figure Page

LIST OF FIGURES – CONTINUED

Figure Page

LIST OF FIGURES – CONTINUED

Figure Page

LIST OF FIGURES – CONTINUED

Figure Page

ABSTRACT

Biology has designed a suite of compartments and barriers that confine fundamental biochemical reactions. Such barriers include the membrane-bound organelles but also a suite of protein-based compartments that architecturally and chemically integrate catalytic processes. These compartments co-polymerize from multiple protein subunits to form polyhedral structures that spatially separate enzymatic processes. Protein compartments confine volatile intermediates, trap toxic reaction products, and co-localize multiple enzymatic processes for catalytic enhancements. The protein-based compartments represent, advantageously, a combination of form and function that has inspired the synthesis of new, designer materials.

The self-assembly of cage-like structures, the structures of which are reminiscent of the compartments, has been used for the directed encapsulation of active enzymes. We have used the capsid from bacteriophage P22, as a nanocontainer for directing the encapsulation of a variety of gene products, including active enzymes.

The P22 capsid assembles from a coat protein (CP) and a scaffold protein (SP) which templates its assembly. Using the simplicity of the P22 expression system, a strategy was developed and implemented for the directed encapsulation of an active, [NiFe] hydrogenase. We hypothesized and proved the enzyme active site needed to be matured by accessory proteins found within the expression host. A two plasmid expression system was designed, where the hydrogenase cargo was under the control of a different inducer than the P22 CP. The [NiFe]-hydrogenase is a heterodimer and each enzyme subunit was fused to different SP. The resultant packaging of the two SP fusions, with the hydrogenase large and small subunits fused to them stabilized a weak heterodimeric structure. Remarkably, the stabilizing effects of the capsid allowed us to probe the infrared signatures associated with the hydrogenase active site.

Finally, the progress made here in developing a virus capsid for H_2 production left room to build increased complexity into the P22-Hydrogenase system while also taking inspiration from the innate, biological function of the hydrogenase. We incorporated a cytochrome/cytochrome reductase pair to drive H_2 production using NADH. These designs, built at the molecular level, represent inherently renewable catalysts that pave the way for a new era of catalytic materials synthesized entirely by biology.

CHAPTER ONE

INTRODUCTION

Overview

Biology has designed and programmed the capacity to differentiate between self and foreign through distinct barriers. A fundamental example of such barriers is the cell, whose boundaries are the cell wall. This barrier separates itself from other cells and keeps cellular machinery and genetic material localized. The definition of what defines a biological barrier is not static, however, and is continually evolving with advances in structural biology. These advances combined with electron microscopy data from nearly 60 years ago have begun to shed light on a set of prokaryotic, subcellular based compartments. These structures, which can combine supramolecular architecture with catalytic function, have prompted interdisciplinary work by molecular biologists, chemists, and materials scientists to build new complex biomaterials which take inspiration from these biological containers.

Intracellular Bacterial Microcompartments

Bacterial microcompartments (BMCs) are protein-based structures, ranging in size from 50-250 nm, that polymerize and assemble from multiple protein components to form a protein-based shell with an interior enzyme that produces a volatile or toxic metabolite that is consumed by another interior enzyme (*1*). This biological polymerization is advantageous for the enzymatic cargo and host cell alike in that it

creates a high local concentration of enzymes and substrates, allows for the substrates (and products) of inefficient biochemical reactions to be trapped on the inside of these structures, and toxic intermediates are sequestered. The chemistry catalyzed by these remarkable structures, some of which have been characterized using structural biology, have inspired new design strategies for biomaterials design and synthetic biology (*2-8*).

Subcellular compartments, some of which are structurally reminiscent of viral capsids, were initially discovered, almost serendipitously approximately 50 years using electron microscopy(*9*). These protein shells were initially thought to be virus capsids but subsequent structural, genetic, and biochemical studies of these structures (later called the carboxysome microcompartment) found they contained ribulose-1,5-bisphosphate (RuBisCO) and carbonic anhydrase (CA) co-localized within the protein shell (Figure 1.1). While most of the BMCs are polymerize to form polyhedral structures, the carboxysome contains a second conserved domain which forms pentamers(*5*). These pentamers assemble with hexamers to adopt icosahedral geometry. Carbon fixation by the carboxysome is completed in two steps: first, bicarbonate is actively transported across the cell membrane into the cytosolic space followed by diffusion across the carboxysome shell into the crowded interior space of the carboxysome, second, bicarbonate is converted to carbon dioxide (CO_2) by carbonic anhydrase(*1*). RuBisCO converts CO_2 to 3-phosphoglycerate by capitalizing upon the crowded interior of the carboxysome and colocalization of CA to enhance its normally poor substrate selectivity. Subsequent studies have shown the RuBisCO enzymes cluster and nucleate the assembly of the carboxysome shell(*10, 11*).

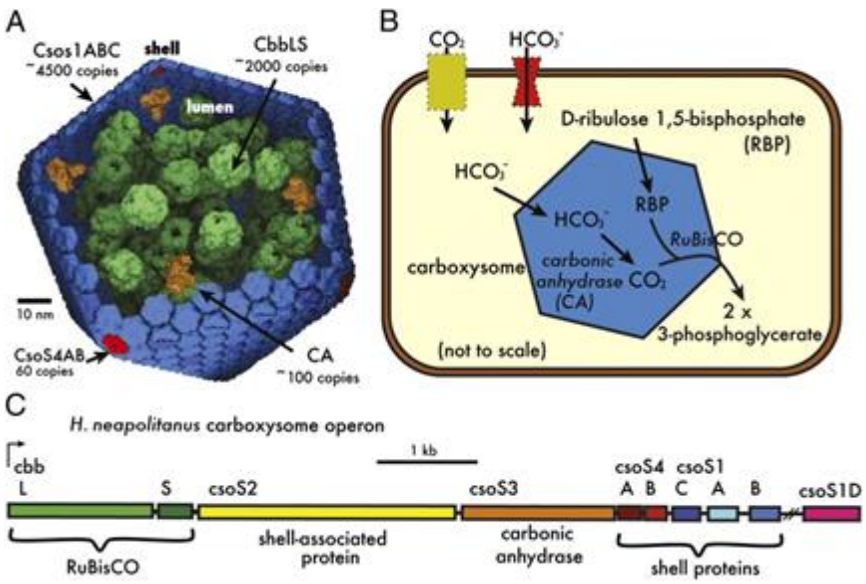

Figure 1.1 The Physical and Genetic Makeup of the Carboxysome (from *Bonacci et al PNAS* (2012)). The shell exterior (a) of the carboxysome (blue) is composed of multiple proteins which copolymerize and protect two enzymes, RuBisCO and carbonic anhydrase. The biochemistry of the carboxysome (b) starts with the transport of hydrogen carbonate across the carboxysome exterior which is a substrate for carbonic anhydrase. Carbonic anhydrase transforms hydrogen carbonate to carbon dioxide, which serves as a substrate for RuBisCO. RuBisCO transforms carbon dioxide into 3-phosphoglycerate. The organization of the carboxysome operon (shown in c) from H. neapolitanus, an example organism.

The enzymes found within microcompartments are not limited to carbon fixation. The chemistry and structure of two bacterial microcompartments, the ethanolamine utilization (Eut) and propanediol utilization (Pdu) microcompartment has initiated many new structural and biochemical efforts(*4*). While the Eut and Pdu share the same working theme as the carboxysome, they are considerably more complex.

In brief, the Pdu BMC in a first step, 1,2-propanediol is converted to propionaldehyde(*10*). Propionaldehyde is a trapped, toxic intermediate and is converted to propionyl-CoA and propanol, thereby circumventing its release(*1*). In the Eut BMC,

ethanolamine is initially converted to acetaldehyde, which is a toxic, fortuitously short-lived substrate for aldehyde dehydrogenase and alcohol dehydrogenase. The genes encoding for the Pdu and Eut BMCs show strong sequence similarity to the genes encoding for the carboxysome(*12*). The Eut shell assembles from 4 protein components (EutS, EutL, EutK, and EutM) and the Pdu shell assembles from 6 proteins (PduA, PduB, PduJ, PduK, PduT, PduU). Both contain a common structural motif in the form of a α/β fold(*7*) and are assembled from hexamers but do not possess the regular icosahedral features of the carboxysome.

As a final example, a set of smaller bacterial microcompartments (24 nm) from *Thermotoga maritima* form a group called the encapsulins which have functional similarities to the larger microcompartments(*13*). The encapsulins are spherical T=1 icosahedral structures that package a peroxidase and ferritin-like protein (containing a ferroxidase active site). These proteins are directed to the interior of their shells using C-terminal peptide tag.

Encapsulation of Enzymatic and Other Cargos Using Protein Cages

A set of biological architectures, virus-like particles (VLPs) and protein cage nanoparticles (PCNs), are set of nanocontainers that are structurally similar to the BMCs, and they have a long history as synthetic containers and reaction vesicles. The VLPs and PCNs have distinct symmetries, defined and homogenous sizes, and large internal volumes. These properties have prompted many scientific efforts in molecular display due to their innate multi-valency, their potential ability to spatially localize cargo on the inside , and their tunable mechanical properties. VLPs and PCNs have three discrete

areas for modification: the inside, the interfaces between residues, and exterior proteins through chemical and/or genetic modification (Figure 1.2).

The structures of BMCs, where catalytic cargos are confined, sequestered in a crowded interior space, has inspired and initiated many efforts in bio-inspired materials chemistry using PCN and VLPs in a biomimetic fashion(*14*). While a focus here will be on the internal encapsulation of catalytic cargo, it should be noted that these containers have been extensively exploited for molecular display of peptides on the exterior and the encapsulation of polymers, minerals, and other, smaller nanoparticles on their interior (*15-31*).

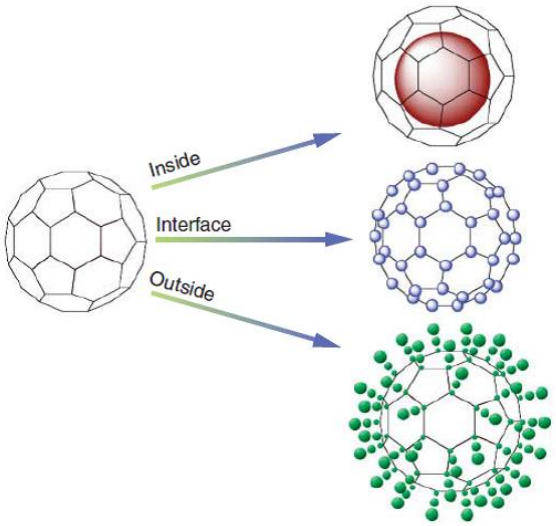

Figure 1.2 Three Possible Modes Exist for Protein Cages and Virus-Like Particles. Protein cages and virus-like particles can be modified in three discrete ways: (1) the encapsulation of artificial cargo(s) on the interior; (2) modification at the interface between exterior proteins; and (3) through site specific modification of exterior residue(s). From Douglas and Young, *Science* (2012). Reprinted with permission from AAAS.

Finally, new work has focused on understanding how enzymatic reactions can be modulated through confinement in the potentially crowded, cell-like interior of a protein cage in a similar way that the carboxysome co-localizes carbonic anhydrase and RuBisCO. Enzyme kinetics has historically been studied in dilute solutions and limited by the assumptions of this reductionist approach. The ability to direct multiple copies of an enzyme to the interior of a reaction container presents a large opportunity for scientific explorations in the crowding effects of enzymes which could contribute to fundamental biochemistry and building new materials.

Nanoparticles and Protein Cage Architectures with Catalytic Properties

The ability to constrain a reaction environment within a hollow protein cage is a unique strategy for the synthesis of new materials. This approach has been extensively utilized to trap inorganic nanoparticles, minerals, and branched polymers. An important approach is one that could use the simple building block of the protein cage for the generation of fuels using catalytic cargo trapped on the inside.

The small heat shock proteins (HSPs) are well-studied examples of constrained reaction environments. HSPs are 12-24 kDa proteins which oligomerize to form 12-20 nm nanoparticles(*32*). In biology, these protein cages are expressed under cellular stress conditions, such as heat and impart a thermotolerance to recombinant proteins co-expressed with the HSP by acting as a chaperone. As a specific example, the sHSP from *Methanococcus jannaschii* assembles from 24 copies of a 16.5 kDa subunit to form a 12 nm protein cage that can be used as a constrained container for chemistry. The sHsp contains a porous 6.5 nm interior cavity that allows free exchange with the bulk medium.

In work that mimics the hydrogenase enzymes while also utilizing the properties of molecular confinement, platinum was mineralized on the inside on the Hsp (Figure 1.3)(*33*). Platinum is a well-established metal used for industrial hydrogen production.

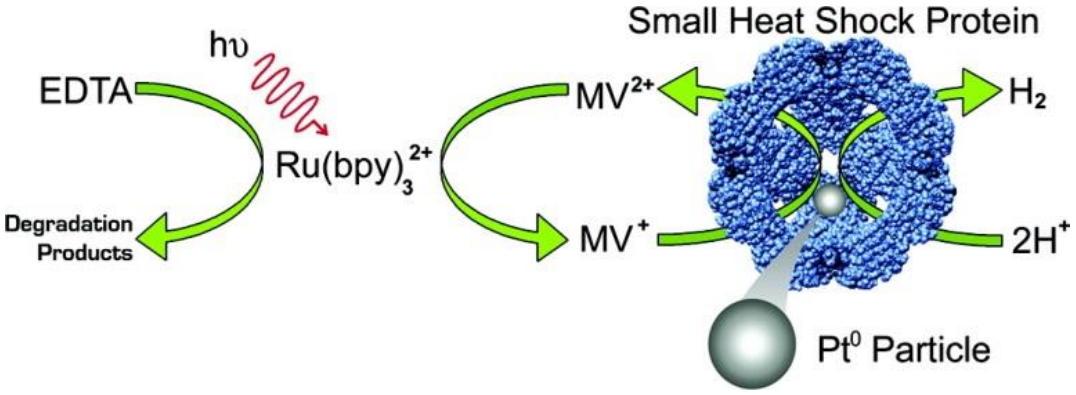

Figure 1.3 The Light-Mediated Hydrogen Production of Platinum Loaded Small Heat Shock protein (from Varpness *et al. Nano Letters* (2005)). The $Ru(bpy)_3^{2+}$ is excited by light resulting in electron transfer to an electron mediator (methyl viologen; MV) which is reduced from its oxidized state to a reduced, radical form following by electron transfer to the platinum inside the protein cage.

In order to mineralize platinum, the assembled protein cage was incubated with $PtCl_4^{2-}$ with heat and then reduced using dimethyl amine borane resulting in platinum nanoclusters trapped on the inside, without altering the cage structure. Hydrogen production was measured using a ruthenium cocatalyst, methyl viologen electron mediator, and EDTA as a sacrificial reductant. The authors reported rates of hydrogen production comparable to the most active hydrogenases with significantly enhanced thermal stability in their construction of an artificial hydrogenase.

Listeria innocua Dps (LiDps) (DNA binding protein from starved cells) is an additional protein cage that has been used for the nucleation and growth of platinum

nanoclusters, as well as for the constrained mineralization of other metal oxides(*34*). LiDps assembles from 12 subunits to form a tetrahedral protein cage with a 9 nm diameter and 0.8 nm pores at the three-fold axis which allows for free exchange with the bulk. In contrast to work with sHSP, platinum was loaded in LiDPS through site specific labeling. In this approach, an interior serine residue was mutated to a cysteine and then modified through conjugation with 5-iodoacetamido-1,10-phenanthroline, a metal binding ligand. Upon the addition of Pt^{2+}, Pt nanocluster formation would occur facilitating easy monitoring of the reaction by mass spectrometry. This work was an important advance because it was the first to monitor this reaction within a protein cage by noncovalent mass spectrometry(*34*).

Enzyme Encapsulation Within Virus Capsids

As an alternative strategy, using PCNs and VLPs for the encapsulation of enzymes and protein-based cargo can take the form of two general routes: *in vitro* and *in vivo* encapsulation. One of the first efforts using an *in vitro* encapsulation technique used the capsid from cowpea chlorotic mottle virus (CCMV), a single stranded RNA plant virus(*31*). CCMV is a T=3 icoshedral virus which has diameter of 28 nm. It assembles from 180 copies of a coat protein and is versatile platform for encapsulation of cargo due to reversible, metal ion and pH dependent assembly. At a pH greater than 6.5, the capsid swells and forms sixty 2 nm pores thus allowing cargo to be encapsulated on the inside through exchange with the bulk medium(*35*). Upon transition to more acidic pH (< pH 6.5), the capsid can contract and trap cargo on the inside. This approach was used to encapsulate a single horseradish peroxidase within the virus-like particle CCMV. This

was important because it showed the first proof of principle demonstrating the free diffusion of substrates and products across a porous capsid barrier(*36*). Additional updates to this research theme using CCMV, as well as other VLP platforms for *in vitro* have since been reported(*37*, *38*).

In contrast to the *in vitro* assembly, *in vivo* encapsulation has the advantages of programmed assembly using facile cloning and expression vectors. Through these expression vectors, potentially difficult, non-native proteins can be expressed and direct cargo to the inside. These strategies are built upon an attraction, which is often electrostatic, between the cargo protein and the capsid interior. An early example of *in vivo* encapsulation is where the interior of the non-viral VLP lumazine synthase was mutated to negatively charged glutamic acid residues. In this work, the negatively charged lumazine synthase monomer was co-expressed with green fluorescent protein that had been tagged with a positively charged arginine tag(*39*). A follow up to this work used directed evolution to optimize the encapsulation of HIV protease. Through the encapsulation process, the toxic HIV protease was sequestered on the inside of lumazine synthase but remained inactive(*40*). An additional strategy exploited the SV40 capsid minor coat proteins for the directed encapsulation of active enzymes(*41*).

In a similar approach, the bacteriophage Qβ capsid has been used to package proteins in order to examine the effects of encapsulation on catalytic activity (Figure 1.4). The bacteriophage Qβ assembles from 180 copies of a 14 kDa coat protein (CP) to form a T=3 icosahedral virus-like particle(*42*). In the infectious form of the virus, RNA is packaged due to an attraction between a hairpin loop and exposed, interior amino acids of

the CP. In their expression system for the packaging of enzymes, two IPTG inducible plasmids are co-expressed in *E. coli*; one plasmid contains the enzyme of interest with an N-terminal arginine-rich (Rev) tag while the other plasmid contains Rev aptamer with the CP and a packaging hairpin loop(*43*). Through the expression of these genes, the Rev-tagged enzyme binds to the aptamer and the hairpin is bound to CP. In their system, the N-terminal aspartate dipeptidase (PepE), a firefly luciferase (Luc), and a themrostable mutant firefly luciferase (and their free purified counterparts, as controls) were encapsulated within Qβ(*43*).

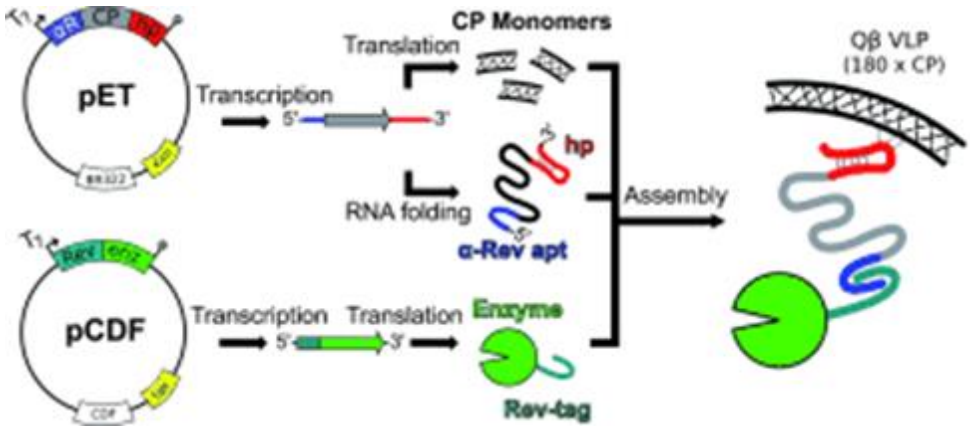

Figure 1.4 The Encapsulation of Enzymes Within the Qβ Capsid Using Two Plasmids (adapted from Fielder *et al. Angew. Chem. Int. Ed.* (2010)). One plasmid induces the expression of mRNA, and the coat protein (CP) of Qβ. A second plasmid induces expression of the Rev-tagged enzyme.

The directed encapsulation showed loading of 2-18 PepE per capsid and reduced the turnover of the enzyme while leaving the apparent K_m unaffected. The packaging of the Luc proteins was significantly lower at 4-8 copies per particle. Interestingly, upon encapsulation of the firefly luciferase or thermostable mutant firefly luciferase

demonstrated increases in K_m of up to 5-fold. Upon encapsulation of greater copies of the respective enzymes, K_m increased while the overall turnover decreased from 35 s^{-1} to 20 s^{-1} in the case of the thermostable mutant.

Conclusions and Future Outlook

Bacterial microcompartments, consist of a protein shell that spatially separates and confines enzymes with their substrates and products to an interior space. Their remarkable structures allow volatile or toxic intermediates to be trapped and through this can catalytic processes can be potentially enhanced. The entrapment which is built on the idea of directed self-assembly has inspired the design and synthesis of a new class of biomaterials. These new biomaterials may enhance turnover of normally fragile enzymes, allow for milder synthetic reaction conditions, and permit the union of only the most favorable properties of many materials. Virus-like particles and protein cage nanoparticles are especially attractive molecular handles for mimicking either synthetically or biochemically some of the characteristics of BMCs. These nanoparticles are advantageous because they spatially separate the reaction environment from the bulk, possess innate multi-valency for site-specific chemistry, and are compatible with a wide range of reaction conditions.

CHAPTER 2

THE CAPSID FROM BACTERIOPHAGE P22 AND ITS USE AS A NANOMATERIAL

Bacteriophage P22 – An Overview

The bacteriophage P22, a classic short-tailed phage, is a double stranded DNA virus which infects *Salmonella enterica* and it has been extensively used as a model for virus assembly (Figure 2.1)(*44*, *45*). The mature virion assembles into a T=7 icosahedral capsid from numerous gene products (termed 'gp'): a scaffold protein (SP; gp8), coat protein (CP; gp5), portal protein (gp1, and 12 copies each of three minor ejection proteins (gp7, gp16, gp20) (*45*). Assembly of the infectious phage passes through a procapsid intermediate which is composed of 415 copies of the coat protein and 100-300 copies of the scaffolding protein. The scaffold protein is directed to the interior of the capsid shell and templates the assembly of the coat protein. This procapsid intermediate is approximately 56 nm in diameter. Interestingly, a procapsid form of the P22 can be generated from a variable number of scaffold protein and 420 copies of coat protein (*in vitro* or *in vivo* using *E. coli* or *Salmonella* expression) yielding virus-like particle (VLP). This VLP does not harbor infectious properties.

In the infectious bacteriophage, prior to DNA packaging, the dodecameric portal (gp1) protein is situated at a five-fold vertex which works in concert with two additional proteins (gp2 and gp3) to drive the packaging of 43.5 thousand base pairs of DNA with high fidelity (*46*). The dodecameric portal protein results in a symmetry mismatch since

it is situated at a 5-fold axis. It is thought this symmetry mismatch helps drive the rotational motion required for the packaging of DNA(*45*). As DNA is packaged the scaffold protein is released, leading to the formation of a larger, more angular capsid shell. The capsid packages specific amount of DNA and terminates the DNA packaging process through a pressure sensor inside the capsid, which signals the terminase complex (gp2 and gp3) to cleave the DNA.

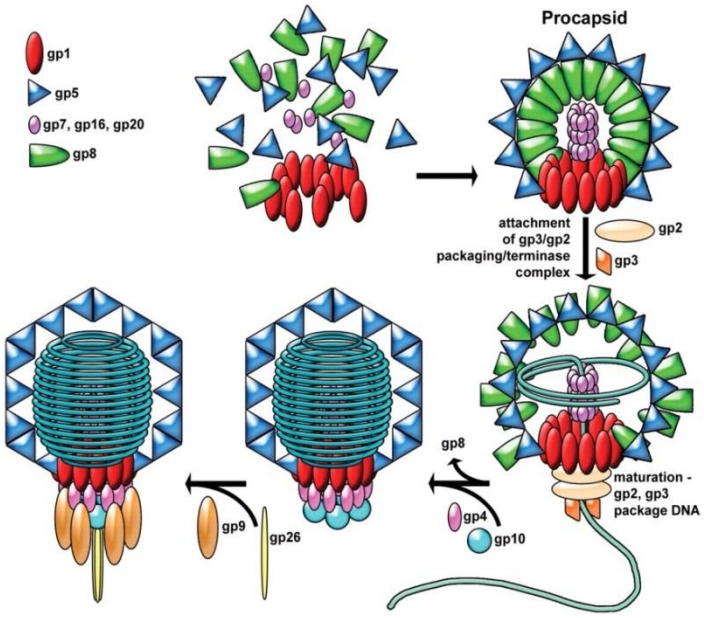

Figure 2.1 Bacteriophage P22 Assembles From Many Gene Products to Form an Infectious Virion (from Lander *et al. Science* (2006); reprinted with permission from AAAS). The procapsid is assembled from 415 copies of the coat protein (blue; gp5), and 100-300 copies scaffold protein (green; gp8) to form a T=7 icosahedral particle. The portal complex is situated at a single five-fold axis which, with the assistance of other gene products, packages DNA through a headful packaging mechanism to form the infectious P22.

The terminase complex is then released from the capsid assembly after this splicing event (*46*). This initiates attachment of tail assembly to the portal protein, built from the gene products of four other proteins (gp4, gp10, gp26, and gp9).

The Scaffold Protein

The virus-like particle assembly has provided insights into the role and purpose of the scaffold protein, a critical, structural component of the assembly. The scaffold protein is thought to lower the concentration of coat protein necessary to polymerize into procapsids, thereby templating the assembly of properly formed T=7 icosahederal particles(*47*). A structure of the full length scaffold protein does not exist and it is thought that only a portion of the C-terminal region is ordered (Figure 2.2)(*48*). The scaffold protein in its full length form is 303 amino acids and the extreme C-terminus, with a helix-turn-helix is composed of 11 carboxy-terminal amino acids. The helix-turn-helix is responsible for interacting with the coat protein (*48-50*) to generate procapsids. It has been proposed that through electrostatic interactions associated with the basic amino acids found at the carboxy terminal, coat proteins are triggered for the assembly process through dimerization(*51*).

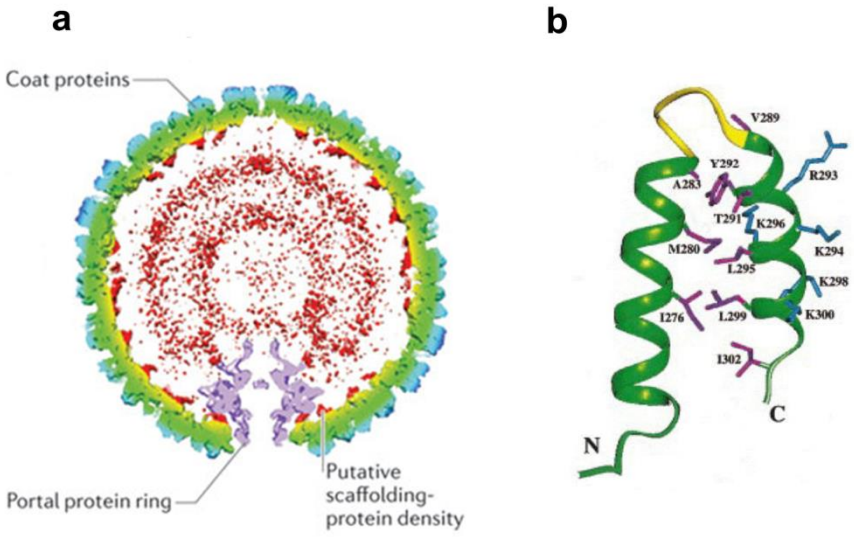

Figure 2.2 A central sliced cryo-EM reconstruction of the P22 procapsid and structure of the scaffold protein from bacteriophage P22 (adapted from *Casjens et al. Nature Reviews Microbiology* (2011) and Sun *et al. J. Mol. Bio.* (2000)). (a) A central slice of the P22 procapsid showing inner coat protein density in red with yellow indicating scaffold protein density. (b) The NMR structure of the scaffold protein helix-turn-helix showing hydrophobic residues in purple and basic residues in blue.

In the full length scaffold protein, dimerization of scaffold protein monomers may further aid the coat protein subunits as they adopt their quasi-equivalent conformations during conformational switching (*52*). Interestingly, in the *in vitro* assembly of proheads, where scaffold protein and coat protein monomer are mixed together, it is thought scaffold protein dimers direct the assembly but SP monomers are required to complete the assembly processs (*52*). If there is insufficient (monomeric) SP, the assembly process reaches a kinetic trap leading to the formation of aberrant assemblies.

The P22 VLP can be heterologously expressed in *E. coli* with the assistance of 100-300 copies of the full-length scaffold protein or an N-terminal truncated form of the scaffold protein. Truncation at either the 141or 238 position generates T=7 icosahedral

capsids identical to those assembled with a wild-type scaffold protein. This has effectively proven that the first 237 amino acids are not essential for procapsid formation and allowed for increased interior space for the potential directed encapsulation of 'cargo' proteins.

Engineering P22 as a Nanomaterial

Cargo proteins, such as folded proteins or polypeptides can be fused to the N or C-terminus of the scaffold protein and directed to the capsid interior without disrupting the capsid assembly. This design strategy makes use of a simple molecular biology toolbox. An upper size limit for cargo proteins is likely in the range of 200 kDa although some evidence suggests the limit could be even larger. This directed self-assembly approach strongly parallels and complements chemical conjugation approaches using P22 as a handle. Given the multi-valency of the capsid, the ability to easily mutate interior coat protein residues to more reactive ones (without modifying the assembly process) and conjugate small molecules to 420 sites, is a powerful technique for high-loading of the capsid. In brief, the capsid has been utilized for the constrained synthesis of polymers(*22, 53*), minerals(*15, 24*), functional proteins genetic based approaches(*54-57*), and higher order materials(*58*).

In vivo the P22 undergoes a unique morphological transition during the DNA packaging process, progressing from a spherical capsid to angular icosahedral phage devoid of scaffold protein and packaged with DNA. This transformation can be mimicked *in vitro* resulting in a 10% increase in diameter. This is known as "expanded shell" and is replicated in the laboratory by heating the capsid at 65^0C for 20 minutes.

An additional morphology, "wiffleball," can be formed by further heating of the capsid at 75˚C for 15 minutes resulting in the release of subunits found at the pentamer vertices. The release of these pentamers creates 12 10-nm holes in the capsid but still maintains the stability of the expanded shell morphology.

The first published result using the P22 capsid in an *E. coli* expression system showed the packaging of two fluorescent proteins: green fluorescent protein (GFP) and mCherry (Figure 2.3)(*59*). In this design, GFP or separately, mCherry was fused to the N-terminus of a truncated scaffold protein (SP_{141}) on a plasmid containing the P22 coat protein. A flexible linker (containing a thrombin cleavage site) between the GFP and the SP was also added. The expression and purification of the capsids showed packaging of 281 GFP and 233 mCherry per capsid after analysis by multi-angle light scattering (MALS).

The capsids were subjected to gentle heating at 65˚C leading to the expanded form of the capsid and then treated with thrombin resulting in the cleavage of the SP with rentention of the GFP on the inside. A separate group of capsids were heated to 75˚C, the expanded structure is transformed into the wiffleball conformation containing twelve 10 nm pores, resulting in the controlled release of the GFP-SP. A subsequent follow-up study co-encapsulated the mCherry and GFP within the same capsid with the careful design of linkers between the fluorescent proteins(*60*). The two fluorescent proteins were a FRET pair within the capsid and the high local concentration inside the capsid lead to an increased FRET response compared to the free, linked pair of fluorescent proteins.

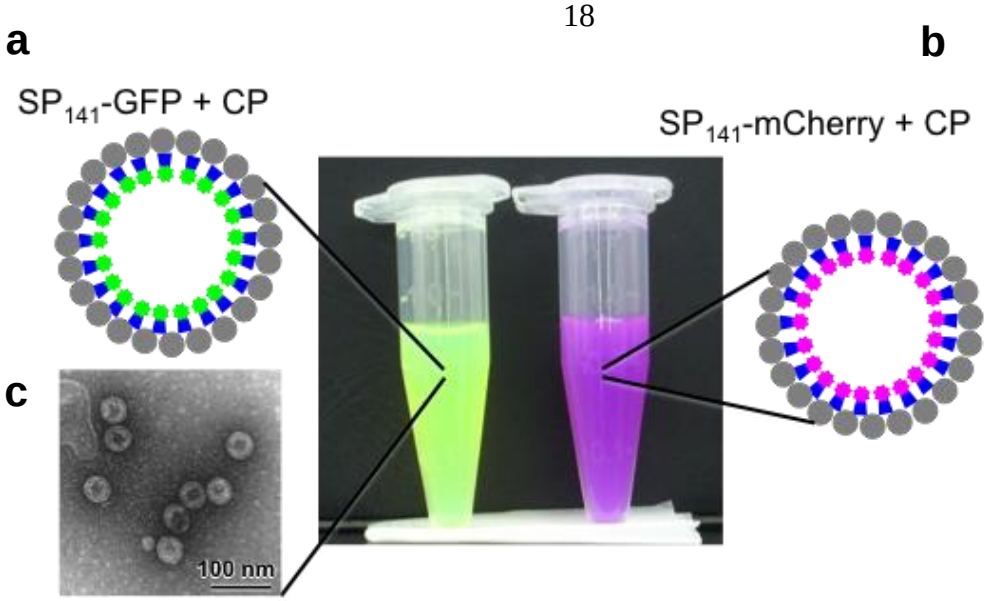

Figure 2.3 The directed encapsulation of mCherry and GFP within the P22 capsid (adapted from O'Neil *et al* (2011)). Using molecular biology cargo protein can be fused to the scaffold protein, which is directed to the interior during *in vivo* expression. In this example green fluorescent protein (a) or mCherry (b) can be encapsulated within the P22 capsid, resulting in virus-like particles indistinguishable from wild-type particles (c).

The P22 capsid has been explored for the directed encapsulation of enzymes and this work has achieved the highest loading of active enzymes (on a per particle basis) reported. Using an *in vivo* expression method, where cargo is fused to the N-terminus of the scaffold protein using genetic means. The initial example of this was the alcohol dehydrogenase D (AdhD) isolated from a hyperthermophile, *Pyrococcus furiosis* (Figure 2.4) *(61)*. The enzyme catalyzes the reduction of ketones and alcohols using an NADH cofactor that becomes hydrolyzed and acts as a facile method of measuring activity. As in previous encapsulation work with GFP, the monomeric enzyme was fused to the N-

terminus of the scaffold protein.

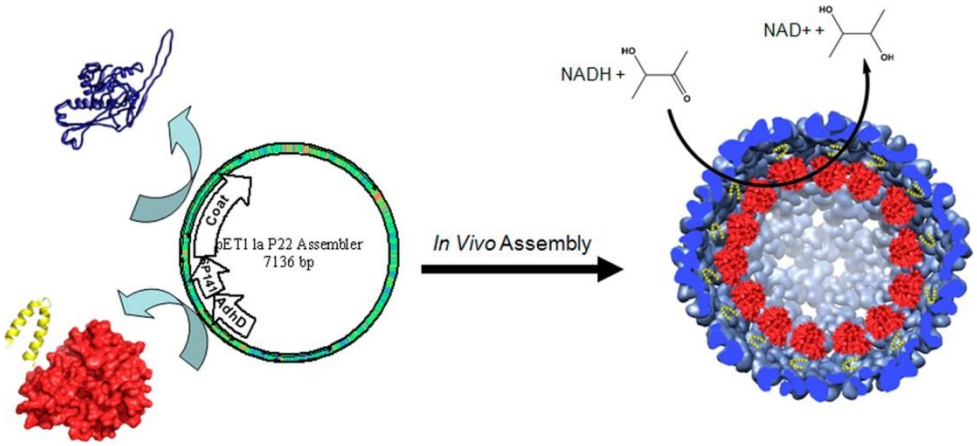

Figure 2.4 Plasmid expression system for the expression and packaging of alcohol dehydrogenase D in the capsid from bacteriophage P22 (from Patterson *et. al. ACS Nano* (2012)). A single plasmid used for the dual expression of AdhD-SP and the P22 coat protein under the control of single promoter.

The protein was expressed in *E. coli* and after purification revealed encapsulation of nearly 250 copies of the enzyme. This is the highest that has ever been reported in an enzyme encapsulated virus-like particle and is equivalent to an internal concentration of 7 mM or nearly 350 mg/mL. The activity of the encapsulated enzyme was assayed through the three different form of the P22 capsid thus gaining control over the internal concentration. When the enzyme was assayed at 50˚C and all three forms of the enzyme showed a decrease in k_{cat} when compared to the free AdhD. The apparent K_m decreased in all three forms of the enzyme. This resulted in the efficiency of the reaction, k_{cat}/K_m very similar to the free enzyme, despite significant decreases in concentration in the expanded and wiffleball forms of the enzyme.

An additional example of enzyme encapsulation using the P22 capsid made use of the tetrameric beta-glycosidase, CelB, isolated from *Pyrococcus furiosis* (*62*). The CelB hydrolyzes lactose to glucose and galactose. The directed encapsulation of CelB was an attractive next step for enzyme encapsulation due to its robust quaternary structure, wide range of substrate selectivity and temperature dependence. Analysis of the CelB-P22 demonstrated packaging of up to 87 copies of enzyme within the procapsid form of the enzyme. The kinetics of enzyme were quantitated using 4-nitrophenyl-β-D-glucopyranoside, which upon cleavage by CelB, produces the easily detectable 4-nitrophenol. The turnover (k_{cat}) of CelB was largely unchanged upon encapsulation (40.3 ± 1.07 for free CelB vs. 34.6 ± 0.898 for procapsid CelB). A general goal of enzyme encapsulation is in increase in the catalytic properties but the results here show consistent maintenance of activity through encapsulation. Howver, the expression technique used and choice of a highly robust enzyme led to little loss in activity. Many encapsulated enzymes using protein cages or virus-like particles show significant loss in activity upon encapsulation.

A final example to be discussed here shows the ability to engineer increased complexity to create a synthetic P22 metabolon built from two or three enzymes, all co-encapsulated within one capsid (Fig. 2.5). The metabolon was constructed from three enzymes: CelB (discussed previously), a monomeric ATP-dependent galactokinase (GALK) and a dimeric ADP-dependent glucokinase (GLUK). GALK phosphorylates galactose transforming it into galactose-1-phosphate while GLUK transforms glucose into glucose-6-phosphate. The proteins were fused together using flexible linkers and

fused as a unit to the scaffold protein. Separately, a construct consisting of CelB-GLUK-P22 was examined as a negative control. The triple enzyme fusion showed a rate that was up to two times faster than the two-enzyme fusion, indicating that all three enzymes are active.

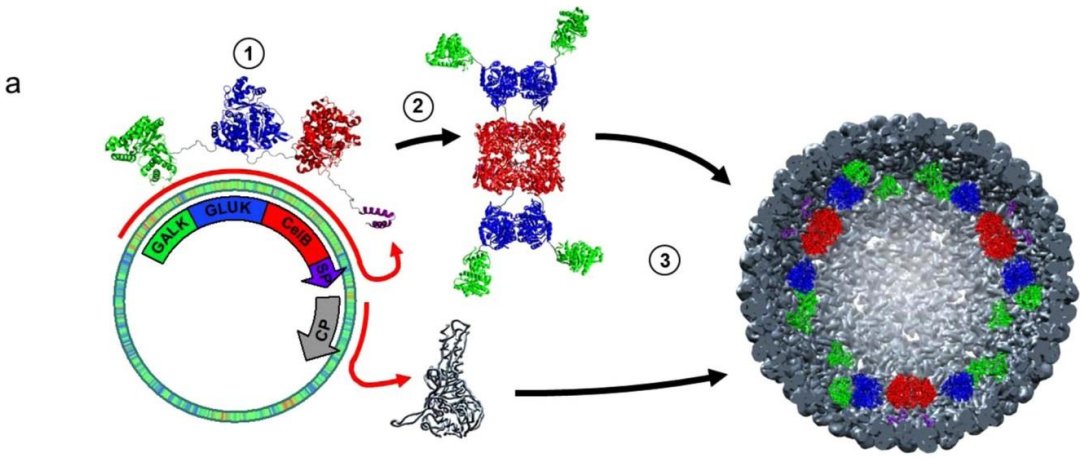

Figure 2.5 The expression and packaging of a triple enzyme fusion within the P22 procapsid (from Patterson *et al. ACS Chem. Bio.* (2014)). A single enzyme was used for the expression of a triple enzyme fusion consisting of GALK-GLUK-CelB-SP and the P22 coat protein (CP) resulting in the packaging of the enzyme fusion.

Conclusions and Future Outlook

The infectious bacteriophage P22 assembles from many gene products to form an infectious virion with remarkable complexity. By decoupling the two most important components of the virus, the scaffold protein and coat protein, a virus-like particle can be expressed in *E. coli* in high yields with cargo fused to the N- or C-terminus of the scaffold protein. This cargo is directed to the interior of the capsid. This directed self-assembly approach has been used for a suite of folded proteins, including those with

enzymatic properties in order to study the effects of confinement and crowding on enzymatic processes.

A brief selection of packaged proteins has been discussed here. The expression and packaging process is still being fine-tuned to encapsulate even more complex systems. Through genetic or chemical modification of the capsid exterior, it may be possible to combine these catalytic capsids to form soft materials with different degrees of order.

CHAPTER THREE

THE HYDROGENASES

Overview

A branch of biological hydrogen production utilizes a set of highly complex enzymes called hydrogenases(*63*). Hydrogenases are enzymes that catalyze the selective, often reversible interconversion of protons and electrons. They are found in the three domains of life and their highly specialized redox centers provide energy for the cell either through the oxidation of hydrogen or the removal of cellular based reducing agents for hydrogen production.

Three main classes of hydrogenases are found in nature (Figure 3.1), organized based on their metallic active site: [FeFe], [NiFe], and [Fe]-only. As a group, these enzymes possess metal-based active site cofactors and biologically unusual ligands which help maintain an oxidation state necessary for the reduction of protons or oxidation of molecular hydrogen(*63*). The catalytic mechanism of these enzymes varies by their class and is studied by biochemical and spectroscopic techniques.

[FeFe]-Hydrogenase

The first to be discussed is the [FeFe]-hydrogenase, which has been isolated from bacteria and some eukaryotes, and is biased towards hydrogen production. The reduction of protons and electrons takes places at the H cluster – a complex, bridged FeS cluster(*64*, *65*). This bridge, linked by a cysteine thiolate, consists of two parts: a 2Fe

subcluster, coordinated by biologically unusual ligands, connected to a [4Fe-4S] subcluster (Figure 3.1)(*65*). The quaternary structure of these enzymes is variable between organisms. While this class of hydrogenases is biased towards hydrogen evolution, it is highly sensitive to oxygen, necessitating strict anaerobic purification. Initial hypotheses have shown that upon exposure to oxygen, inactive intermediates are formed with the loss of the 2Fe subcluster leading to protein inactivation. Initial, new work with the [FeFe] hydrogenase from *Chlamydomonas reinhardtii* ($HydA^{\Delta EFG}$) suggests that even after oxygen exposure intermediates can be reactivated by maturation proteins associated with the 2Fe subcluster(*64*). This has sparked interest in and new work integrating the [FeFe] hydrogenase with photosynthetic machinery for photobiological hydrogenase(*3*).

[Fe]-Only Hydrogenase

A second hydrogenase is the [Fe]-only hydrogenase and is relegated to methanogenic archaea(*66*). The enzyme provides reducing equivalents, through the reduction of hydrogen, for transforming carbon dioxide into methane. The enzyme contains an iron atom without iron sulfur centers. The enzyme catalyzes the heterolytic cleavage of hydrogen followed by a hydride transfer to 5,10-meth-enyltetrahydromethanopterin.

[NiFe]-Hydrogenase

A third class of hydrogenases is the [NiFe]-hydrogenase which contains a bimetallic active site containing nickel and iron. Three iron sulfur clusters in series act as

an electron wire leading to or from the active site. The catalytic bias of this electron wire and the [NiFe] center varies amongst different organisms and groups of hydrogenases.

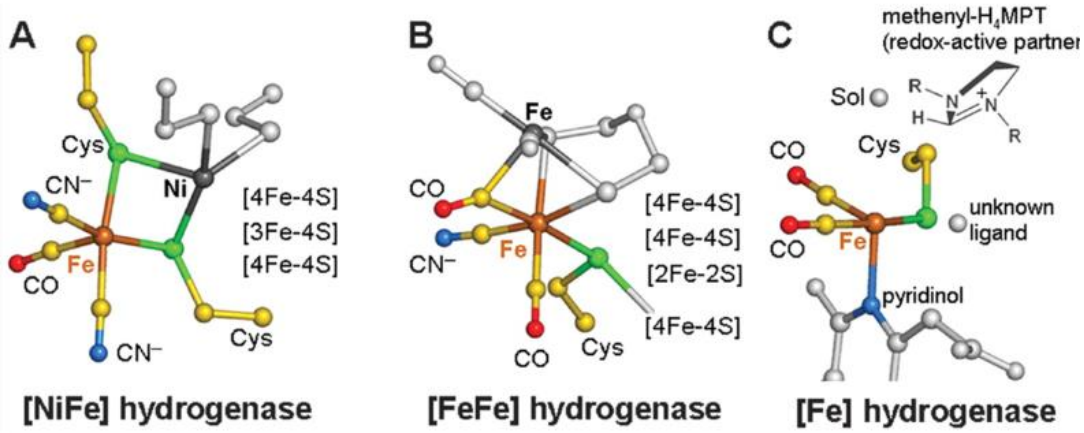

Figure 3.1 The Three Classes of Hydrogenases Found in Nature are the [NiFe], [FeFe], and [Fe]-Hydrogenases (from Shima *et al. Science* (2008) Reprinted with permission from AAAS). They are identified by their unique metallic active site with biologically unusual ligands coordinating the metal. The [NiFe] hydrogenases (in the core active site) consist of a bimetallic center where the iron atom is coordinated by two CN- ligands and one CO ligand. The [FeFe] hydrogenase are composed of the 2Fe subcluster, coordinated by biologically unusual ligands, connected to a [4Fe-4S] subcluster. The [Fe]-only hydrogenase contains an iron atom with CO ligands but is devoid of iron sulfur centers.

There are four main groups of NiFe hydrogenases: group 1 is the membrane-bound hydrogen oxidizing (uptake) hydrogenases; group 2 is composed of sensory and uptake hydrogenases; group 3 contains heteromultimeric hydrogenases; and group 4 is an energy conserving group of hydrogenases(*63*). The [NiFe] hydrogenases are often heterodimeric with a small and large subunit. The small subunit contains three [FeS] centers, termed the proximal [4Fe-4S], medial [3Fe-4S], and distal [4Fe-4S] clusters. The small subunit also contains a C-terminal alpha-helical membrane anchoring domain, which physically links it to a cytochrome b(*67*). There is a recent crystal structure of the

E. coli [NiFe] hydrogenase 1 in complex with its native cytochrome indicating – the first crystal structure of its kind and indicating a close contact between the heme of the cytochrome and the proximal iron sulfur center. Electrons are transferred from the small subunit to or from the large subunit which contains a [NiFe] center. The proximal iron sulfur center has been implicated in the oxygen tolerance of some [NiFe] hydrogenases, determined using mutational studies complemented by spectroscopy(*68-71*).

In the large subunit, the nickel is coordinated by 4 conserved cysteine residues - two of these bridge to the Fe iron. The oxidation state of nickel is predominantly Ni^{2+} or Ni^{3+} depending on the stage of the catalytic cycle. The iron atom is also coordinated by three biologically unusual diatomic ligands: one CO and two CN^{-}(*72*). The cyanides are sigma donor ligands that hydrogen bond to surrounding residues within the active site(*63, 73, 74*). These ligands are essential for maintaining the oxidation state of the Ni and Fe through its catalytic cycle.

There is an additional bridging ligand found more oxidized redox states of the hydrogenase. The bridging ligand is OH^{-} in an oxidized, inactive form of the enzyme. There are three catalytic states for the active form of the enzyme: Ni-R, Ni-SI, and Ni-C. The Ni-R state is the most reduced form the enzyme; additional one electron reductions following this state form the Ni-C and Ni-SI states.

The identity of the carbon monoxide and cyanide ligands amongst the O_2-sensitive and O_2-tolerant hydrogenases was determined primarily by Fourier Transform Infrared Spectroscopy (FTIR) (*68, 73-76*). These ligands produce diagnostic bands in the infrared region between 1850-2100 cm^{-1}, making them well-suited for study by infrared

spectroscopy (Figure 3.3). Small variations between depending upon protein origin (for example *Desulfovibrio* vs. *E. coli*) protein origin but the CO ligands typically produce bands between 1900-2010 cm^{-1} while the CN^- ligands produce bands between 2010-2100 cm^{-1}.

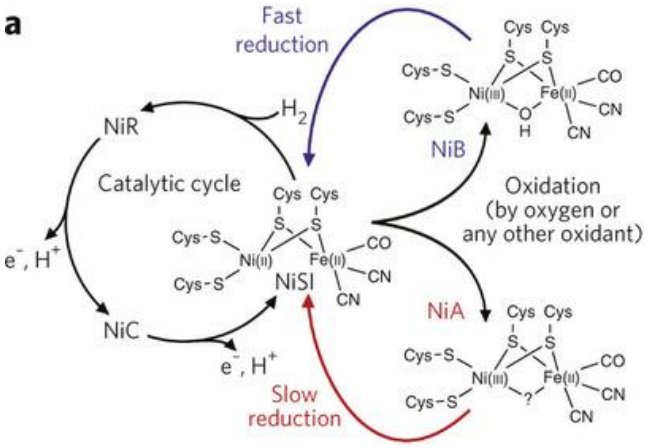

Figure 3.2 An Abbreviated Version of the Catalytic Cycle of the [NiFe]-Hydrogenases Showing the Inactive and Active Catalytic States (from Hamdan *et al. Nature Chemical Biology* (2013)). The [NiFe]-hydrogenases consist of a complex redox cycle consisting of the as-isolated, inactive form of the enzyme (Ni-B or Ni-A) that can be slowly or quickly be reactivated. The Ni-SI state ("silent ready" is formed upon reduction of either of these species. Upon the addition of substrate (H_2), two additional forms of the enzyme (Ni-R and Ni-C) are observed.

These bands shift to higher or lower frequencies depending on the state of the hydrogenase in the redox cycle. The shifts act as an important diagnostic of active site fidelity and provide insights into potential inhibitors and light sensitive states of the [NiFe]-hydrogenases.

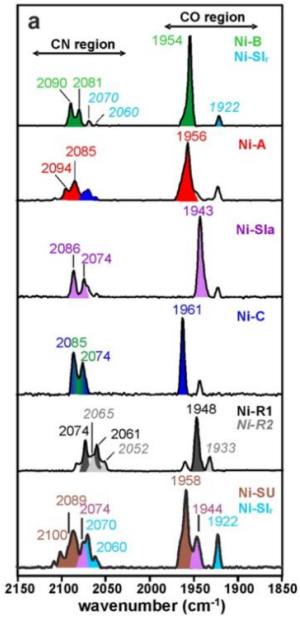

Figure 3.3 FTIR Spectroscopy of the Distinct Catalytic States of the [NiFe]-Hydrogenases Provides an Active Signature (from Lubitz *et al. Chemical Reviews* (2014)). FTIR spectroscopy of the [NiFe]-hydrogenases probes the CO and CN^- ligands which coordinate the Fe atom within the active site. The CO ligand produces bands between 1900-2000 cm^{-1} while the CN^- ligands produces bands between 2000-2100 cm^{-1}. The peaks associated with these ligands shift through the catalytic cycle of the hydrogenase and can be correlated to other spectroscopic techniques.

It has been proposed that the sources of the ligands have different metabolic origins through infrared spectroscopy of maturation proteins associated with [NiFe]-hydrogenases(*75*). The origin of the cyanide ligands has been proven in numerous studies to be carbamoylphosphate. In the *E. coli* hydrogenases, the HypF-HypE and HypC-HypD maturation proteins catalyze ATP-dependent the biosynthesis and insertion of the cyanide ligands(*77*). The origin of the carbon monoxide ligand remains elusive.

The oxygen tolerant membrane associated hydrogenases have gained attention for their use in potentially biotechnology for use in hydrogen production and hydrogen

oxidation in fuel cells(*78*). Among these is a branch of *E. coli* hydrogenases that when grown both aerobically and anaerobically can exhibit hydrogenase activity, as either whole cells or in the isolated protein. There are three distinct *E. coli* hydrogenase enzymes: Hyd-1 ("EcHyd-1"), Hyd-2, and Hyd-3(*79*). Hyd-1 is encoded by a six gene operon hyaABCDEF, of which hyaA and hyaB form the small and large subunits of the enzyme while hyaC endodes for its associated cytochrome. Hyd-2 is encoded by a four gene operon (hybOABC) part of a larger hybOABCDEFG operon and Hyd-3 is encoded by hycBCDEFG. HypB, D, E, and F are responsible for maturation of all hydrogenases in addition to the other genes found within the operon.

The [NiFe]-hydrogenases are more biased toward H_2 oxidation instead of proton reduction due to strong product inhibition. However, intriguing spectro-electrochemical work has shown that above pH 5 Hyd-1 and Hyd-2 are irreversibily biased toward hydrogen production(*80*). From pH 3-5 both enzymes exhibited reversibility of Hyd-1 and Hyd-2, at strong overpotentials demonstrating their potential use for clean yet efficient hydrogen production(*80*).

Assaying for Hydrogen

Hydrogenases can be assayed for hydrogen oxidation or evolution. Hydrogen oxidation can be measured electrochemically or with an electron acceptor, such as methylene blue, which exhibits an easily monitored change using absorbance spectroscopy. Hydrogen evolution for the hydrogenases is traditionally measured using an electron mediator and a sacrificial reductant. Historically, the most common electron mediator/sacrificial reductant is methyl viologen and sodium dithionite. Under anaerobic

conditions, sodium dithionite reduces methyl viologen from a dication to a radical form which then transfers an electron to the hydrogenase. Hydrogen is then measured using gas chromatography.

A complicating but often overlooked factor in this highly used assay technique is the diminished reducing power of dithionite at lower pH values(*81*). This is challenging for measuring enzymes which reduce protons and electrons to hydrogen more favorably at acidic pH. While older literature has given greater attention to the effects of pH on the reaction rate, newer work has not(*82*). Additionally, the pH optimum for hydrogenases differs greatly based on the source of the hydrogenase and the assay technique.

Conclusions and Future Outlook

The hydrogenases are a highly complex branch of metalloenzymes that can oxidize hydrogen to provide an electron source for the cell or reduce protons and electrons to yield hydrogen gas. Structural and spectroscopic approaches have yielded advances in understanding the biochemistry, microbiology, and often elusive structures of these complex metalloproteins. For example, previous evidence had suggested that the CO ligands of all [NiFe] are photolabile while only a portion of the [NiFe] hydrogenases possess a photolabile ligand(*83*). Significant attention has been placed on the [NiFe]-hydrogenases which are less efficient in H_2 oxidation or the reduction of proton and electrons) but are less easily degraded by oxygen damage.

An increased understanding of the hydrogenases has generated interest in fuel cell technologies, photoelectrochemical cells, or integrating them with components of the photosynthetic machinery for light driven hydrogen production(*84, 85*). There have also

been advances in synthetic approaches in mimicking the active site of the [NiFe] and [FeFe] hydrogenases.

CHAPTER FOUR

SELF-ASSEMBLING BIOMOLECULAR CATALYSTS FOR HYDROGEN PRODUCTION

Contribution of Authors and Co-Authors

Manuscript in Chapter Four

Author: Paul C. Jordan

Contributions: Developed the concept, designed the experiments, analyzed the data, co-wrote the paper

Co-Author: Dustin P. Patterson

Contributions: Developed the concept

Co-Author: Kendall N. Saboda

Contributions: Assisted in characterization of the P22-Hyd_{opt}

Co-Author: Ethan J. Edwards

Contributions: Assisted with the ICP-MS and TEM

Co-Author: Heini M. Miettinen

Contributions: Cloned the genes for the 6xHis-hyaB-SP & 6xHis-hyaA-SP

Co-Author: Gautam Basu

Contributions: Assisted with the spectroscopy

Co-Author: Megan C. Thielges

Contributions: Supervised the spectroscopy

Contribution of Author and Co-Authors - Continued

Senior Co-Author: Trevor Douglas

Contributions: Developed and conceived the concept, analyzed the data, obtained funding, co-wrote the paper

Manuscript Information Page

Paul C. Jordan, Dustin P. Patterson, Kendall, N. Saboda, Ethan J. Edwards, Heini M. Miettinen, Gautam Basu, Megan C. Thieleges, Trevor Douglas

Journal Name: Nature Chemistry

Status of Manuscript:
____ Prepared for submission to a peer-reviewed journal
____ Officially submitted to a peer-review journal
_X_ Accepted by a peer-reviewed journal
____ Published in a peer-reviewed journal

Nature Publishing Group
Submitted: July 23, 2015

CHAPTER FOUR

SELF-ASSEMBLING BIOMOLECULAR CATALYSTS FOR HYDROGEN PRODUCTION

Accepted In: *Nature Chemistry*

Paul C. Jordan[1,2], Dustin P. Patterson[3], Kendall N. Saboda[2], Ethan J. Edwards[1,2], Heini M. Miettinen[4], Gautam Basu[5], Megan C. Thielges[1], Trevor Douglas[1]

[1] *Department of Chemistry, Indiana University, Bloomington, Indiana 47407*
[2] *Department of Chemistry and Biochemistry, Montana State University, Bozeman, Montana 59717*
[3]*Department of Chemistry and Biochemistry, University of Texas at Tyler, Tyler, Texas 75799*
[4]*Department of Microbiology and Immunology, Montana State University, Bozeman, Montana 59717*
[5]*Department of Biophysics, Bose Institute, Kolkata 700054, India*

Supporting Information Contained in Appendix A

Abstract

The chemistry of highly evolved protein-based compartments has inspired the design of new catalytically active materials that utilize and self-assemble from biological components. A frontier of this biodesign is the potential to contribute new catalytic systems for production of sustainable fuels, such as hydrogen. Here we show the encapsulation and protection of an active hydrogen producing and oxygen tolerant [NiFe]-hydrogenase, sequestered within the capsid of the bacteriophage P22 through directed self-assembly. We co-opted *E. coli* for biomolecular synthesis and assembly of this nanomaterial by expressing and maturing the EcHyd-1 hydrogenase prior to expression of the P22 coat protein, which subsequently self assembles. By probing the

infrared spectroscopic signatures and catalytic activity of the engineered material we demonstrate that the capsid provides stability and protection to the hydrogenase cargo. These results illustrate how combining biological function with directed supramolecular self-assembly can be used to create new materials for sustainable catalysis.

Introduction

Biology has evolved to create discrete spaces, through the use of well-defined barriers and compartments, in order to localize and constrain certain chemical processes. These include organelles bounded by membranes, but also recently discovered micro- and nano- protein compartments capable of catalyzing remarkable chemistry(*4, 5, 13, 86*). These protein-based compartments are assembled from multiple subunits and can harbor catalytically active components while also controlling the access of reactants and products, making them models for efficiency, chemical plasticity, and an inspiration for biomimetic design.

There are a growing number of examples of protein-based compartments in nature and their structures and morphologies are as diverse as the reactions they catalyze. The carboxysome is a protein cage with a diameter of 80-140 nm, which encapsulates the enzymes ribulose-1,5-bisphosphate carboxylase-oxygenase (RuBisCO) and carbonic anhydrase to enhance CO_2 fixation inside many cyanobacteria and chemoautotrophs(*87-89*). Lumazine synthase, from *Aquifex aeolicus*, assembles into icosahedral capsids and catalyzes the penultimate step of riboflavin biosynthesis(*90*) while ferritin, an octahedral protein cage, catalyzes the formation of iron oxide nanoparticles as a component of iron homeostasis(*91*). These intriguing natural designs, where biological function is

integrated with supramolecular self-assembly, have initiated new efforts in bioinspired chemistry(*14, 92-96*).

The ability to improve upon the efficiency of natural containers, mimic or perhaps redesign them for new synthetic purposes presents a powerful opportunity for the development of catalytic materials. Self-assembly of a range of cage-like architectures have been described for the encapsulation of active enzymes(*36, 40, 41, 43*) and we have previously demonstrated that the capsid from the bacteriophage P22 is a particularly powerful platform for the directed assembly and encapsulation of a wide range of gene products, including active enzymes(*55, 61*). The P22 capsid assembles from 420 copies of a coat protein (CP) and a variable number of scaffold proteins (SP), which direct capsid assembly(*97*). By truncating the SP and genetically fusing a cargo protein of interest to the N-terminus, we have shown that we can maintain the SP directed self-assembly and direct the encapsulation of the cargo protein in high copy number within the T=7 icosahedral capsid(*51, 98*). The advantages offered by this and other encapsulated enzyme systems, are protection of active catalytic species, control over substrate access, and the inherently renewable biosynthesis of these unique nanoparticles. With these advantages, design and synthesis at the level of molecular biology can be utilized in conjunction with bacterial overproduction to produce a new class of designer catalysts.

At the frontier of this work is the development of sustainable and clean fuel production, a priority for science in the next century. Hydrogen has emerged as a focal point for the development of energy rich, renewable fuels but its production, using non-

precious metal catalysts remains a challenge. Current work has focused on hydrogen storage, oxidation, and generation but even the most efficient catalysts for hydrogen generation are hindered by costs and the use of the rare earth metals. There is increased attention to harnessing a set of highly evolved, complex biocatalysts, known as hydrogenases, which catalyze the reduction of protons to form H_2 (and the reverse reaction)(*63*). Many successful efforts have elucidated both the structure and function of a number of these catalysts. Three classes of hydrogenases are found in nature ([FeFe], [Fe]-only, and [NiFe]), classified by the transition metals and biologically unusual ligands contained within their active sites. The [FeFe]-hydrogenases are highly efficient catalysts but low yields in their isolation and purification with their oxygen intolerance remain large barriers to their use as functional catalysts(*99*). The [Fe]-only hydrogenases are H_2-generating methylene-tetrahydromethanopterin dehydrogenases found only in methanogenic archaea, but are inactivated by O_2 and have a thermal and photolabile cofactor(*100*). In contrast, the [NiFe]-hydrogenases, involved in both hydrogen uptake and evolution, are oxygen tolerant(*69*, *71*), can be integrated into biomaterials(*101*), and show great promise as functional catalysts(*78*).

The formation of a robust and stable renewable hydrogen producing catalyst represents a powerful new target. We have demonstrated here the expression and maturation of *E. coli* hydrogenase 1 (EcHyd-1), a highly active [NiFe]-hydrogenase(*67*, *71*), which is sequestered and stabilized within the P22 capsid through directed self-assembly. EcHyd-1 is encoded by a 6 gene operon (*hya*ABCDEF), of which the first two genes, *hya*A and *hya*B, encode for the small and large subunits of the hydrogenase

enzyme, respectively(*102*). While the [NiFe] active site of EcHyd-1 resides in the large subunit, it has been shown that the small subunit, with a hydrophobic membrane-anchoring C-terminal extension, confers oxygen tolerance due to a unique [FeS] cofactor(*69, 71*). Biologically unusual cyanide (CN^-) and carbon monoxide (CO) ligands, first identified by Fourier transform infrared spectroscopy (FTIR) coordinate the iron atom in the large subunit(*72, 74, 75*). The gene products of *hya*CDEF play essential roles in maturation of the organometallic [NiFe] active site and are required for an active EcHyd-1(*67, 79, 103, 104*).

By co-opting *E. coli* as an expression system for hyaA and hyaB, with each subunit individually fused to a P22 scaffold protein, we have used the cells as biomolecular factories for the formation of this catalytic nanomaterial. By expressing and maturing the EcHyd-1 heterodimer prior to expression of the P22 coat protein (CP) we have achieved control over the production, maturation, and self-assembly of this new and stable nanocatalyst (P22-Hyd). The facile, aerobic biosynthesis and purification from *E. coli* together with the stability of this Hyd-P22 catalyst offsets the use of an enzyme that is not the most active known hydrogenase. This approach paves the way for a new generation of renewable catalysts inspired and synthesized by biology.

Results

Here we have shown the directed self-assembly and encapsulation of multiple copies of the heterodimeric EcHyd-1 [NiFe]-hydrogenase within the confines of the P22 capsid resulting in an active and stable nanoparticle catalyst (Fig. 4.1). The optimal encapsulation was achieved through the expression of the small subunit (hyaA), lacking

the membrane anchoring C-terminal extension(*67*), and large subunit (hyaB) of the EcHyd-1 hydrogenase, each fused to a P22 scaffold protein (SP), followed by the induced expression of the coat protein (CP). Importantly, these events must be temporally separated allowing enough time for the active sites of the enzyme to fully mature (Fig. 4.1a) before capsid assembly and packaging inside P22 (Fig. 4.1b). The fusion of the SP to the C-terminus of each hydrogenase subunit directs the assembly of the P22 capsid, as we have previously shown(*59*), and the heterodimeric hydrogenase is sequestered on the capsid interior, resulting in catalytically active P22 particles (P22-Hyd). A single plasmid was engineered to harbor the two SP fusions, hyaA-SP and hyaB-SP, while the CP gene was present on a second plasmid with a different promoter. Expression of the hyaA-SP and hyaB-SP was induced with IPTG for 4 hours followed by the induction of the CP with L-arabinose for 1 hour. This staggered expression of cargo and coat allowed time for sufficient maturation of the active sites of the hydrogenase enzyme subunits (hyaA, hyaB) by taking advantage of the basal expression of the accessory proteins in the EcHyd-1 operon found in the *E. coli* expression host(*103*). This $P22_{hyaA\text{-}SP,\ hyaB\text{-}SP}$ construct exhibits maximal catalytic activity for H_2 production and is termed $P22\text{-}Hyd_{opt}$.

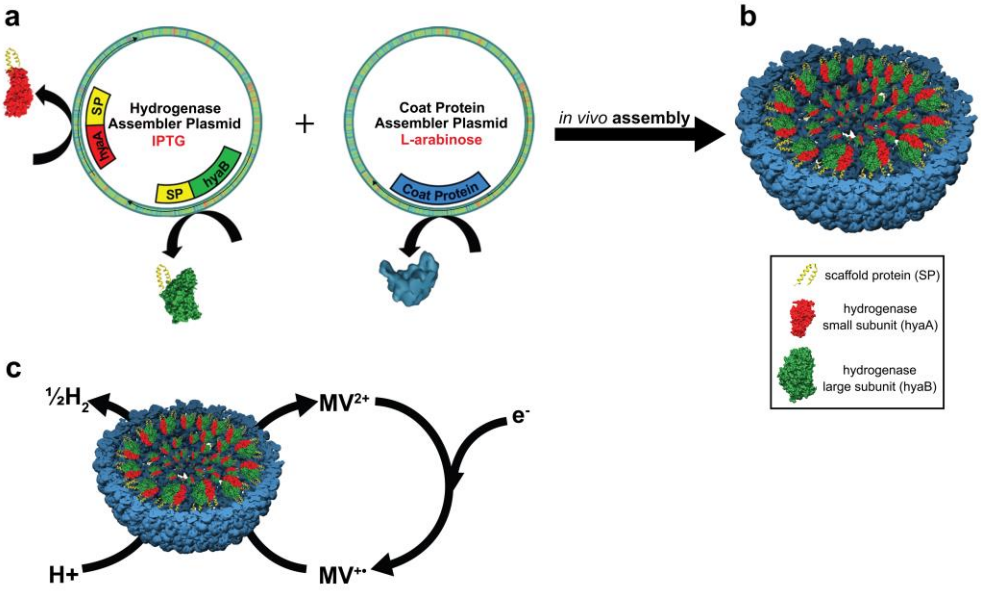

Figure 4.1 An Expression Schematic Showing a Cartoon Representation of EcHyd-1 with Both Subunits (hyaA and hyaB) Fused to Scaffold Protein Encapsulated Within the P22 capsid. **a,** Two plasmids separately containing the hydrogenase cargo (hyaA-SP and hyaB-SP) and coat protein (CP), under the control of different promoters were expressed to generate **b,** the P22 capsid packaged with both subunits of EcHyd-1. **c,** The particles were assayed for H_2 production by gas chromatography using methyl viologen ($MV^{+\bullet}$) as an electron transfer mediator and an e- source (dithionite or electrochemical reduction). The structures are derived from PDB entries 2XYY. 3USE. and 2GP8.

When expression of the hydrogenase subunits and the CP was induced simultaneously, assembled P22 particles (P22-Hyd) that packaged roughly equivalent numbers of each subunit were formed. However, the catalytic activity of this P22-Hyd was significantly diminished relative to the P22-Hyd_{opt} (Fig. A.1). This strongly supports the hypothesis that the accessory proteins in the EcHyd-1 are crucial for generating an active hydrogenase and that we could utilize our flexible expression system to achieve enzyme maturation and particle self-assembly.

The P22-Hyd_{opt} capsids were purified as described previously(*59*) using

ultracentrifugation, taking advantage of the unique size and particle homogeneity of the P22 capsid. Initial analysis of these materials by size-exclusion chromatography (SEC) revealed a population of assembled native-like P22 capsid particles (Fig. A.2). Analysis of the eluting fractions by SDS-PAGE showed that the assembled capsids packaged both hyaA-SP and hyaB-SP in roughly equivalent numbers, consistent with the formation of the EcHyd-1 heterodimer within the P22 capsid (Fig. 4.2a). These purified materials were subsequently analyzed by SEC-multi-angle light scattering (MALS)/quasi-elastic light scattering (QELS), which revealed an average particle molecular weight of 31.9 MDa for the P22-Hyd_{opt} and 27.6 MDa for the P22-Hyd (Fig. 4.2b). After consideration of the known M_w (molecular weight) of the empty capsid (19.7 MDa), the mass difference corresponds to a 'cargo' loading of, on average, 88 copies of the heterodimer within the P22-Hyd_{opt} and 67 copies of the heterodimer within the P22-Hyd capsids. The particle size determined from the angular dependence of the light scattering of P22-Hyd_{opt} showed values similar to wild-type capsids (R_{rms} 22.3 nm ± 0.1 nm; R_h 27.0 nm ± 0.1 nm; R_{rms}/R_h = 0.83). R_{rms}/R_h values close to 1 are consistent with spherical particles with infinitely thin walls, while values less than 1 are characteristic of spherical particles with thicker walls or solid spheres(*105, 106*). Empty P22 exhibits R_{rms}/R_h values of 0.95 and the ratio found for the P22-Hyd_{Opt} of 0.83 indicates dense packaging of hyaA-SP and hyaB-SP inside P22. Similar sizes were obtained for the P22-Hyd (R_{rms} of 26.3 ± 0.04 nm; R_h of 28.5 ± 0.2 nm; R_{rms}/R_h = 0.92). When imaged by transmission electron microscopy (TEM), the P22-Hyd_{opt} and P22-Hyd particles were both observed to be

monodisperse with particle diameters of 56 ± 3 nm and 58 ± 3 nm respectively, nearly identical to the wild type capsids having T=7 icosahedral symmetry (Fig. 4.2c).

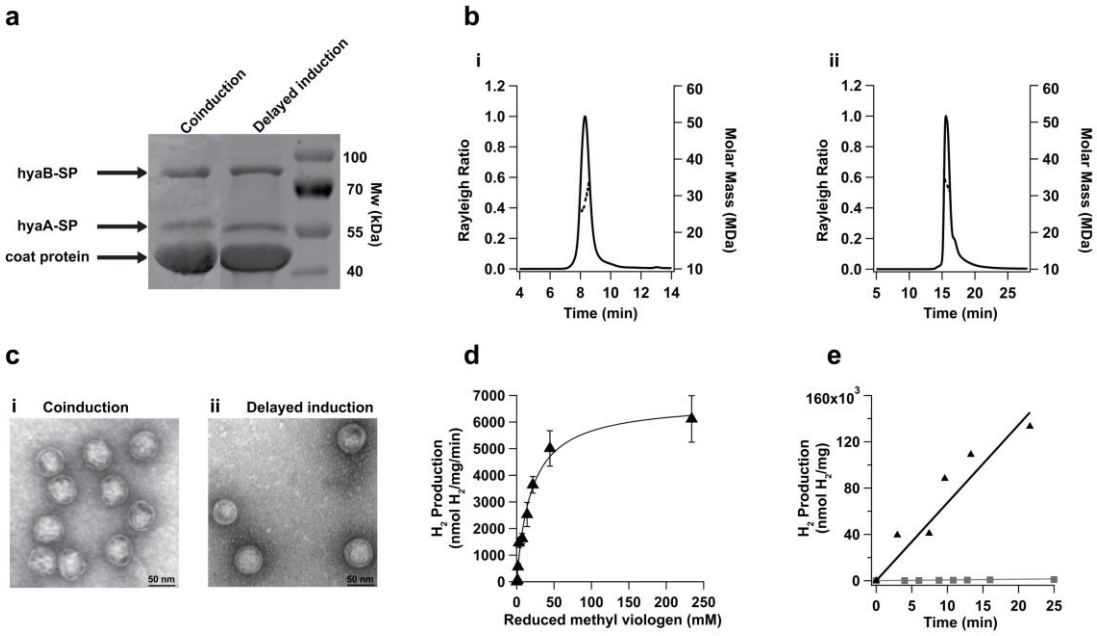

Figure 4.2 The Expression and Characterization of P22-Hyd$_{opt}$/P22-Hyd. **a,** Analysis of P22-Hyd and P22-Hyd$_{opt}$ by SDS-PAGE has bands corresponding to hyaB-SP (85 kDa), hyaA-SP (55 kD), and coat protein (46 kDa). **b,** i. Size-exclusion chromatography-multiangle light scattering (SEC-MALS) of P22-Hyd and ii. P22-Hyd$_{opt}$ reveals a monodisperse population of encapsulated P22 particles. **c,** TEM (negative stain) of **i.** P22-Hyd and **ii.** P22-Hyd$_{opt}$ shows monodisperse particles with T=7 icosahedral symmetry.**d,** The specific activity (nmol H_2/mg/min) of P22-Hyd$_{opt}$ as a function of different concentrations of electrochemically reduced $MV^{+\bullet}$ (electron mediator) at pH 5 follows Michaelis-Menten kinetics. Error bars are the standard deviation of the mean. **e**, The specific activity of P22-Hyd$_{opt}$ (black triangle) and free hydrogenase (grey square) using electrochemically reduced $MV^{+\bullet}$ at pH 5.

The metal content (Ni and Fe) of the encapsulated hydrogenase (both P22-Hyd$_{opt}$ and P22-Hyd) as well free hydrogenase was measured by ICP-MS in order to determine

active site loading. Through analysis of the P22-Hyd_{opt} by SEC-MALS we anticipated roughly 88 Ni and 1065 Fe per capsid. Metal analysis of the P22-Hyd_{opt} construct showed 41 Ni and 546 Fe per capsid, indicating approximately 46 ± 0.1% of the [NiFe] active sites were fully loaded. The co-induced P22-Hyd showed 37 ± 0.1% active site loading (25 Ni and 421 Fe per capsid), which corresponds to the trends observed in activity. Nickel and iron analysis of the free, unencapsulated, hydrogenase revealed 0.27 mol Ni and 0.46 mol Fe per heterodimer. While loading of related [NiFe] hydrogenases are in the range of 2-4 mol Fe/mol protein, previous reports have not detected Ni suggesting that the P22 capsid protects the complex hydrogenase active sites upon encapsulation (*77*).

The activity of the encapsulated EcHyd-1 was assayed for H_2 production (Fig. 4.1c) by gas chromatography using electrochemically (controlled potential coulometry) or chemically (sodium dithionite) reduced methyl viologen (MV). MV is a well-established electron mediator for hydrogenase and dithionite (DT) is a convenient sacrificial reductant but with diminished reducing power of DT below pH 6. Electrochemical reduction allowed us to probe the pH dependence of hydrogen evolution catalyzed by the Hyd-1, which revealed an optimal of pH 5 (Fig. A.3). The EcHyd-1 enzyme has been reported as a hydrogen oxidation catalyst and we have also found it to be active for H_2 oxidation with a specific activity of 34.5 ± 7 μmol $MV^{+\cdot}$•mg^{-1}•min^{-1} *(80)* at pH 8. However, when the P22-Hyd_{opt} capsids were expressed under conditions allowing optimal maturation of the hydrogenase, the enzymes were very active towards proton reduction and evolution of hydrogen. The maximal specific activity was 6773 ± 372

nmol H_2•mg^{-1}•min^{-1} at pH 5 (Fig. 4.2d), corresponding to a turnover of 41 s^{-1} per hydrogenase, which compares very favorably to other [NiFe] hydrogenases(*107-109*). The activity of the P22-Hyd_{opt} at pH 5 at 234 mM methyl viologen was found to be 6118 ± 860 nmol H_2•mg^{-1}•min^{-1} (Fig. 4.2e). When assayed at pH 8.0, with MV/DT, the construct maintained significant activity of 3218 ± 394 nmol H_2•mg^{-1}•min^{-1} (Fig. S1). This reflects over a 100-fold increase over reported activities for the free enzyme(*110*), which are in the range of 12-38 nmol H_2•mg^{-1}•min^{-1}. When hyaA-SP, hyaB-SP and CP were co-induced to form the P22-Hyd capsid, the measured activity was reduced roughly 4-fold to 757 ± 39 H_2•mg^{-1}•min^{-1}, when assayed with the DT/MV at pH 8 (Fig. A.1). This does not take into account that only 46% of the [NiFe] active sites were fully loaded; the reported rates for fully loaded Hyd-1 would be double. There is also clear evidence for product (H_2) inhibition of the enzyme, and upon removal of hydrogen from the reaction, the rate of proton reduction could be substantially increased (Fig. A.4). This is consistent with the known bi-directional activity of the hydrogenase enzymes.

As a comparison, an unencapsulated hydrogenase sample (hyaA-SP, hyaB-SP) was recombinantly expressed in *E. coli* and purified with affinity chromatography. The apparent instability of the recombinant protein made purification of the rEcHyd-1 challenging and highlights a major advantage of the P22 encapsulation approach. The rEcHyd-1 revealed a specific activity of 46 ± 6 at pH 5 (Fig. 4.2e) and 12.6 ± 4 nmol H_2•mg^{-1}•min^{-1} at pH 8 (Fig. A.1), which is markedly lower than the EcHyd-1 encapsulated within the P22 capsid (either P22-Hyd_{opt} or P22-Hyd).

In order to understand the key parameters for assembling an active EcHyd-1

within the P22 capsid, two other hydrogenase constructs were examined (Fig. 4.3). Since the [NiFe] active site of the EcHyd-1 resides in the large subunit hyaB, a construct was made with only hyaB, and not hyaA, fused to SP (hyaB-SP), and expressed with the CP on a separate plasmid using the differential expression in *E. coli* as described above (Fig. 4.3a). The capsids were purified in a similar manner and found to have a specific activity of 108 nmol $H_2 \bullet mg^{-1} \bullet min^{-1}$ (Fig. A.1) at pH 8.

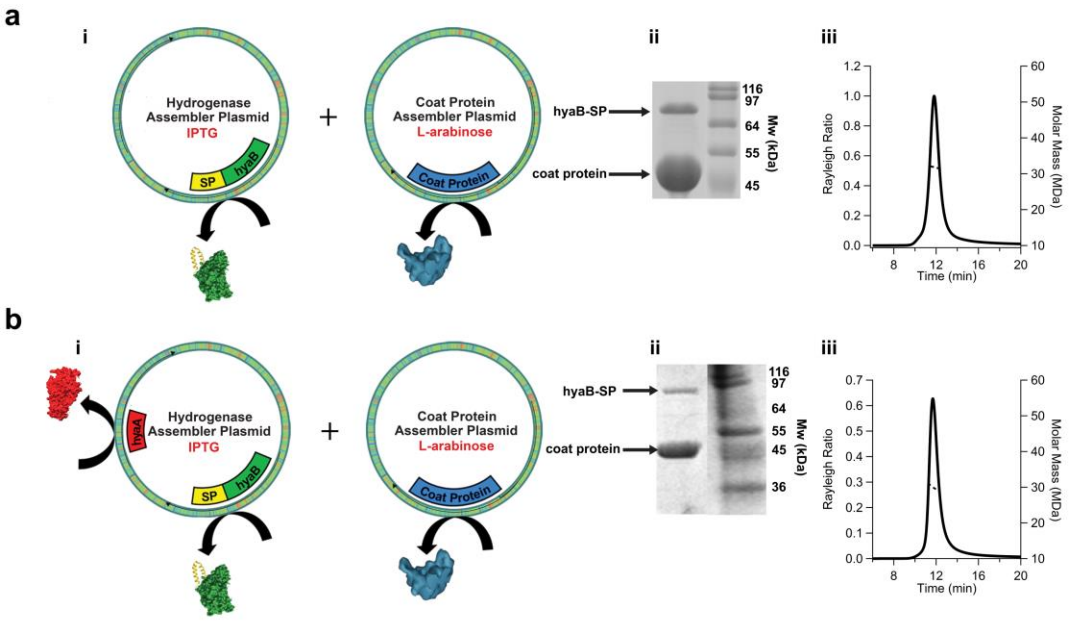

Figure 4.3 The Expression and Characterization of Two Other P22 Hydrogenase Constructs. **a, i,** Schematic of the plasmids for incorporation of only hyaB-SP into the P22 capsid, **ii,** SDS-PAGE demonstrating the packaging of hyaB-SP encapsulated in P22 (hyaB-SP 85 kDa; CP 46 kDa) after purification, **iii,** Size-exclusion chromatography-multiangle light scattering (SEC-MALS) of P22-hyaB-SP reveals a monodisperse population of encapsulated P22 particles, **b, i,** Schematic of the plasmids for incorporation of hyaB-SP and hyaA (without a second SP) into the P22 capsid, **ii,** SDS-PAGE of purified P22 particles reveals packaging of only hyaB-SP (hyaB-SP 85 kDa; CP 46 kDa) with no visible band for hyaA at 35 kDa, suggesting a weak dimer interaction between hyaA and hyaB-SP, **iii,** SEC-MALS of the P22 hyaB-SP hyaA construct demonstrates monodisperse encapsulated P22 particles.

A construct with hyaB-SP and hyaA lacking the C-terminal hydrophobic extension, but without the additional SP fusion, was expressed with CP using the temporally staggered expression system (Fig. 4.3b). We reasoned that if the native quaternary structure of heterodimeric EcHyd-1 was robust it would form and, upon subsequent expression of the CP, the SP would template the capsid assembly and both the

subunits would be packaged as cargo in the assembled capsid. The capsids were purified in a similar manner and SDS-PAGE revealed hyaB-SP and CP but little to no hyaA incorporation (Fig. 4.3b). This hydrogenase-packaged P22 was found to have a specific activity of 754 nmol H_2•mg^{-1}•min^{-1} (pH 8), which is higher than the construct having only the hyaB encapsulated (Fig. A.1). Since we could not detect hyaA on SDS gels, the subunit is likely present only in trace amounts but is nevertheless important to the overall activity of the EcHyd-1, consistent with previous reports citing its importance for O_2 tolerance(*69*). Clearly, both subunits are critical for producing an optimally active EcHyd-1 within the P22 capsid. The encapsulation experiments suggest that the association between hyaB and hyaA is weak. We hypothesized that upon purification of the free rEcHyd-1 enzyme this weak association between subunits would be observed.

A previous report suggested that the small subunit in *E. coli* [NiFe] hydrogenase 1 and other hydrogenases is lost during the purification process(*111*). We tested our hypothesis that the P22 capsid stabilizes the quaternary structure of EcHyd-1 by purification of the free enzyme (hyaA-SP, hyaB-SP) using SEC and analysis of the eluting proteins (Fig. A.5). The heterodimer eluted at approximately 12 mL followed by hyaB-SP at approximately 25 mL (Fig. A.5) when probed by Western blot using antibodies against EcHyd-1. The fractions showing the presence of both subunits (the presumed assembled heterodimer) were pooled and subjected to a second purification by SEC, which yielded a chromatogram with similar features to the first. Analysis of these fractions by Western blot again showed fractions consistent with the heterodimer and later fractions where only the large subunit was detectable (Fig. A.5). This indicates that

the heterodimer exists in a dynamic equilibrium with its constitutive subunits. This directed assembly approach, with each hydrogenase subunit fused to separate SP could therefore be responsible for enhanced encapsulation and enforced dimerization, resulting in the observed stable and catalytically active nanoparticles.

A major advantage of the [NiFe]-hydrogenases for materials applications lies in the fact that these enzymes can be stably produced under aerobic conditions and are relatively oxygen tolerant even after activation. We investigated the oxygen tolerance of the P22-Hyd_{opt}, after activation (dithionite/MV) by exposing the material to air for 24 hours. After oxygen exposure the P22-Hyd_{opt} sample was degassed, reactivated with additional dithionite, and assayed for activity. While there was a loss of activity, the material retained activity measured at 340 ± 26 $H_2 \bullet mg^{-1} \bullet min^{-1}$ at pH 8 (Fig. 4.4a). When a similar experiment was performed on the purified unencapsulated hydrogenase sample, no hydrogen evolution was detected.

EcHyd-1 has been structurally characterized and the Fe atom in the bimetallic active site within the large subunit is coordinated by two CN^- ligands and one CO ligand(*71*). These ligands are essential and biologically unique components of the active site. The clear advantages of our expression and directed self-assembly system to produce stable hydrogenase prompted us to investigate these unique ligands in the active site using FTIR.

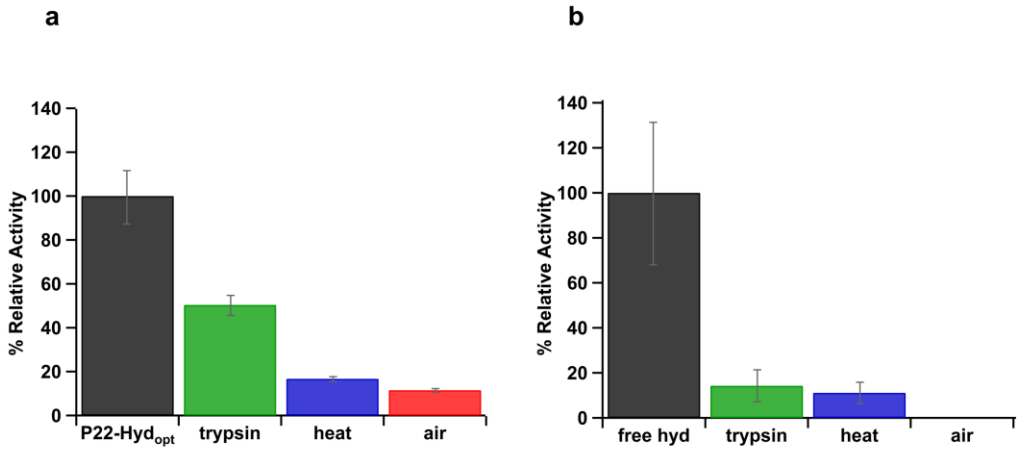

Figure 4.4 The P22 Capsid Provides Protection from Protease, Thermal Denaturation, and Air Exposure with Subsequent Reactivation to its Hydrogenase Cargo. The activity (as a relative percent with error bars associated with the standard deviation of the mean) of **a,** P22-Hyd$_{opt}$ (pH 8) after proteolytic digestion with trypsin, heating, or air exposure with reactivation with identical conditions for the **b**, free hydrogenase demonstrating an inability to be reactivated after air exposure.

The spectrum of P22-Hyd$_{opt}$ in its reduced, catalytic form shows bands between 1900 and 2100 cm^{-1} (Fig. 4.5a) due to the stretching vibrations of the CO and CN$^-$ ligands, in agreement with literature reports for this enzyme and other members of the [NiFe] hydrogenase family(*63, 72, 74, 75*). A number of intermediates have been spectroscopically assigned in the catalytic cycle of [NiFe] hydrogenases (Fig A.8). We observed two νCO bands (1904 cm^{-1} and 1945 cm^{-1}) in the P22-Hyd$_{opt}$ spectrum suggesting the presence of two Ni-SI populations (Ni-SI$_I$, Ni-SI$_{II}$) of the P22-Hyd$_{opt}$ (Fig. 4.5a). The Ni-SI is favored under our conditions but we cannot exclude Ni-R from this

assignment.

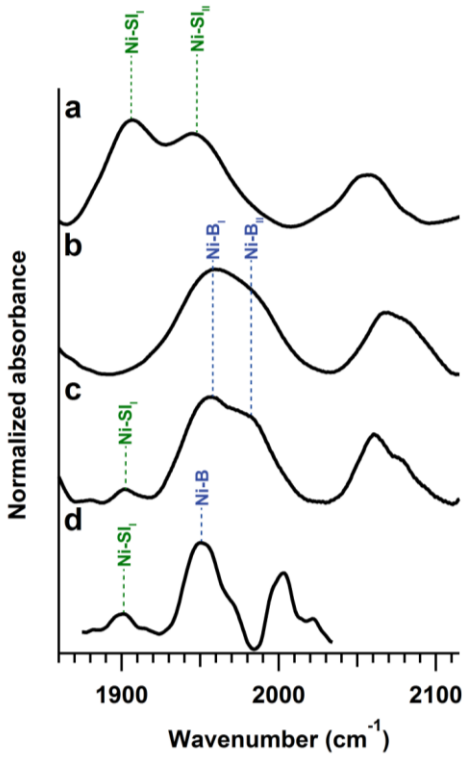

Figure 4.5 The FTIR Spectra of P22-Hyd$_{opt}$ and Free, Purified Hydrogenase. **a,** P22-Hyd$_{opt}$ in its reduced, catalytically active form shows two CO bands associated with two populations of Ni-SI **b,** after exposure to air, shifts in the frequencies of all bands accompany formation of a mixed population of Ni-B states **c,** P22-Hyd$_{opt}$ after rereduction with dithionite shows only partial recovery of the CO band associated with the Ni-SI state **d,** Free, purified hydrogenase showing spectroscopic signatures similar to encapsulated hydrogenase.

Two corresponding pairs of nitrile bands are expected, but are not well resolved due to spectral overlap. A similar, lower intensity *ν*CO band was seen in the free hydrogenase spectrum at 1904 cm^{-1} (Ni-SI) with a larger *ν*CO band at 1952 cm^{-1} corresponding to Ni-B (Fig. 4.5d).

Exposure of the P22-Hyd$_{opt}$ to air leads to the formation of a broadened peak with

overlapping bands attributed to a mixture of Ni-B states (Fig. 4.5b). These oxidation-induced frequency changes are consistent with previous studies of [NiFe] and [FeFe] hydrogenases[34,36,51]. Addition of reductant has little effect on this oxidized state. However, the spectrum (Fig. 4.5c) does show evidence for a small absorbance at 1904 cm^{-1} (Ni-SI_I). Thus the IR spectrum indicates that partial recovery occurs upon re-reduction, and is confirmed by the specific activity of the re-reduced sample, which exhibits 12% (pH 8) of the freshly reduced P22-Hyd_{opt} activity.

The P22 capsid is also known to be protease-resistant. To test whether this would provide an additional protective effect on the encapsulated EcHyd-1, the P22-Hyd_{opt} was treated with trypsin(*112, 113*). The capsid showed protection of the encapsulated hydrogenase from degradation (Fig. A.6) and the P22-Hyd_{opt} particles maintained 51% of their initial activity (1623 ± 148 nmol H_2•mg^{-1}•min^{-1}; pH 8) in contrast to the free hydrogenase sample which showed a 86% decrease in activity down to near background levels (1.8 ± 0.3 nmol H_2•mg^{-1}•min^{-1}; pH 8) (Fig. 4.4b).

The capsid provides an enhanced thermal stability to the encapsulated EcHyd-1 enzyme. When heated at 60˚C for 45 minutes, the free hydrogenase samples demonstrated a dramatic 89% decrease in activity and activity levels of 1.4 ± 0.6 nmol H_2•mg^{-1}•min^{-1} (pH 8) were measured (Fig. 4.4b). In contrast, when the P22-Hyd_{opt} was exposed to the same heating conditions, 17% of the activity (pH 8) was maintained (537 ± 35 nmol H_2•mg^{-1}•min^{-1}). The thermal protection afforded by the P22 capsid may be analogous to a chaperone-like activity or a consequence of the crowded interior environment within the packaged P22(*113, 114*).

Discussion

We have taken inspiration from the chemically and architecturally integrated structures of protein compartments for the programmed synthesis of a highly active biomolecular catalyst for hydrogen production. The combination of enzymatic catalysis with new materials for generating fuels exemplifies a broad interdisciplinary goal. Our work here highlights a sustainable approach to biomaterials design through the integration of the desirable properties of the *E. coli* hydrogenase-1 for proton reduction and hydrogen evolution with the robust capsid from bacteriophage P22. We used an optimized protein expression system demonstrating that hydrogenase maturation prior to encapsulation is required for the optimal activity. The directed assembly of EcHyd-1 to the P22 interior also led to a stabilization of its quaternary structure. This P22-Hyd_{opt} is nearly 100-fold more active than the purified, free enzyme and confers thermal and proteolytic protection to its cargo. Our system showed some ability to be reactivated after air exposure prompting us to examine the changes in the IR spectrum before and after air exposure to interpret the degree of enzyme reactivation.

Methods

Recombinantly Expressed Small Subunit-Scaffold Protein Fusion (hyaA-SP), Large Subunit-Scaffold Protein Fusion (hyaB-SP), and Coat Protein

E. coli strains containing both plasmids were grown at 37 °C in LB medium supplemented with 1 mM ammonium iron (II) sulfate hexahydrate and 1 mM nickel(II) chloride monohydrate in the presence of ampicillin (50 mg/mL) and kanamyacin (15

mg/mL). The expression of hyaB-SP + hyaA-SP was induced by addition of IPTG to a final concentration of 40 μM at OD_{600}=0.6. Cultures were grown for 4 hours after addition of IPTG, and then the expression of the pBAD /HisA (A^R) vector containing the CP was induced with L-arabinose (0.02%, final) and grown for 1 hour . For P22-Hyd, hydrogenase proteins and CP were simultaneously induced by addition of the same concentrations of IPTG and L-arabinose and grown for 3 hours.

Fourier Transform Infrared Spectroscopy (FTIR)

All FTIR spectra were recorded at 4 cm^{-1} resolution with a dry $N_{2(g)}$ -purged Agilent Cary 670 FTIR spectrometer and $N_{2(l)}$-cooled mercury-cadmium-telluride (MCT) detector. Apodization with a 4-term Blackman Harris function and zero-filling by factor of 8 were performed on the interferograms, and the Mertz phase correction method with 32 cm^{-1} resolution was utilized for Fourier transformation. Three to six sets of 4000 scans were recorded and averaged for all samples. To prepare the background sample, P22-Hyd_{opt} was exchanged using an Amicon Ultra Centrifugal Filter into deuterium oxide buffer (Acros Organics, New Jersey, USA), degassed under vacuum, flushed with argon, and loaded between two CaF_2 windows separated by a 50 μm PTFE spacer. P22-Hyd_{opt} was then mixed with methyl viologen (1 mM, final concentration, pH 8), degassed under vacuum, purged with argon, reduced with previously degassed sodium dithionite (1mM, final concentration, pH 8), and loaded into the sample cell. The same procedures were followed for free, purified hyaA-SP, hyaB-SP but without deuterium oxide. The FTIR spectra were also recorded after exposure of P22-Hyd_{opt} to air at 4 $^{\circ}$C overnight and upon re-reduction with sodium dithionite. A polynomial fit to the baseline was performed on

both the 1870-2000 cm^{-1} and 2000-2100 cm^{-1} spectral regions and subtracted from each of the spectra to correct for the slowly varying background absorbance. Background-corrected spectra were smoothed using a 4^{th} order smoothing spline function (MatLab) and averaged.

Acknowledgements

This research was supported by a grant from the U.S. Department of Energy, Office of Basic Energy Sciences, Division of Materials Sciences and Engineering (DE-FG02-08ER46537). We acknowledge the generous gift of EcHyd-1 antibodies from Professor Frank Sargent (University of Dundee).

CHAPTER FIVE

REDESIGN OF A VIRUS PARTICLE FOR NADH-DRIVEN HYDROGEN PRODUCTION

Contributions of Authors and Co-Authors

Manuscript in Chapter Five

Author: Paul C. Jordan

Contributions: Expressed and characterized P22-Hyd_{cyt}, designed studies, and co-wrote the manuscript

Co-author: Joseph C-Y Wang

Contributions: Completed 3D reconstruction of the P22-Hyd_{cyt}

Co-author: Ethan J. Edwards

Contributions: Completed biophysical characterization and analysis of the P22-Hyd_{cyt}, read and edited the manuscript

Co-author: Heini M. Miettinen

Contributions: Cloned the hyaA-Cb5-SP and hyaB-CB5R-SP into the pRSF plasmid

Co-author: Amanda L. Le Sueur

Contributions: Assistance with the design and expression of the cytochrome.

Senior Co-author: Megan C. Thielges

Contributions: Provided the pEC86 plasmid and assistance in cytochrome expression

Senior Co-author: Adam Zlotnick

Contributions: Supervised structural work on the P22-Hyd_{cyt}

Senior Co-author: Trevor Douglas

Contributions: Obtained funding, designed studies, and co-wrote the manuscript

Manuscript Information Page

Paul C. Jordan, Joseph C-Y Wang, Ethan J. Edwards, Heini M. Miettinen, Amanda L. Le Sueur, Megan C. Thielges, , Adam Zlotnick, Trevor Douglas

Status of Manuscript:
_X_ Prepared for submission to a peer-reviewed journal
___Officially submitted to a peer-reviewed journal
___Accepted by a peer-reviewed journal
___Published in a peer-reviewed journal

CHAPTER FIVE

REDESIGN OF A VIRUS PARTICLE FOR NADH-DRIVEN HYDROGEN PRODUCTION

Paul C. Jordan[1,2], Joseph C-Y Wang[3], Ethan J. Edwards[1,2], Heini M. Mietten[4], Amanda L. Le Sueur[1], ,Megan C. Thielges[1], Adam Zlotnick[4], Trevor Douglas[1]

[1]Department of Chemistry, Indiana University,
Bloomington, Indiana 47405
[2]Department of Chemistry and Biochemistry, Montana State University,
Bozeman, Montana 59717
[3]Department of Molecular and Cellular Biochemistry, Indiana University, Bloomington,
Indiana 47405
[4]Department of Microbiology and Immunology, Montana State University,
Bozeman, Montana 59717

Supporting Information Contained in Appendix B

Abstract

The ability to predictably make designer materials that combine multiple, hierarchically arranged components into a single, coupled and stable reaction environment is an especially attractive goal for materials synthesis. New and undiscovered reaction environments with the ability to increase the efficiency and stability of catalytic processes for fuel production are a vital but challenging area of biomaterials research. With these goals in mind, we have used the directed self-assembly properties of a viral capsid to build a multi-component enzymatic process for hydrogen production from readily available molecular precursors. The reaction container is the capsid from bacteriophage P22, which assembles from multiple copies of a coat protein and whose assembly is templated by a scaffold protein, which is directed to the interior to

spontaneously generate a T=7 icosahedral capsid. We have taken inspiration from the spatial arrangement of the innate cytochrome from the *E. coli* [NiFe]-hydrogenase 1 to engineer a cytochrome b_5 together with an NADH-dependent cytochrome b5 reductase in close proximity to the hydrogenase protein to build a new biomaterial, P22-Hyd_{cyt}. Through intricate control of *E. coli* recombinant protein overexpression, we have demonstrated hydrogen production using this multi-component system driven by NADH oxidation. This new biomaterial exemplifies the catalytic advantages of integrating complex materials within defined reaction spaces for hydrogen production.

Introduction

Biological compartments, consisting of lipid or proteins shells, segregate and protect biological catalysts in order to structurally mediate efficient metabolism. The design and synthesis of catalysts inspired by biological compartments and machineries is an attractive yet challenging target for bio-inspired materials chemistry (*1, 4-6, 8, 37, 92, 115*). Multi-step processes, such as enzymatic production of hydrogen from readily available molecular precursors could benefit from hierarchically arranged components to increase the efficiency and stability of the constituent catalytic processes. A group of microbial enzymes, the hydrogenases, has garnered interest for efficient and clean hydrogen production but often require chemical mediators, which could potentially be addressed through biomimetic compartmentalization. Previously, we have demonstrated the increased catalysis of a [NiFe] hydrogenase through localization to the interior of a bacteriophage-derived protein cage. Herein, we build on that system by facilitating

hydrogen production from NADH precursors by the co-localization of a cytochrome b_5/cytochrome b_5 reductase with the hydrogenase.

Two main types of hydrogenases are found in nature, differentiated by their inorganic active sites: the [FeFe]-hydrogenase and the [NiFe] hydrogenase (*63*). The [FeFe]-hydrogenases are found in a small group of prokaryotes and algae while the [NiFe]-hydrogenases are more ubiquitous amongst the three domains of life. A remarkable set of oxygen tolerant [NiFe]-hydrogenases has inspired new molecular design in fuel cells for hydrogen oxidation and the combination of these biocatalysts with photosynthetic machinery for light driven hydrogen production (*3*).

The [NiFe]-hydrogenases are typically composed of a heterodimeric large and small subunit with the small subunit containing iron-sulfur centers which funnel electrons to (and from) the large subunit (*116*). The large subunit contains a highly complex [NiFe] active site coordinated by biologically unusual ligands (CN^- and CO) which play a critical role in the catalytic cycle of the hydrogenase (*74*). An O_2-tolerant hydrogenase from *E. coli*, EcHyd-1, is attached to the cytoplasmic membrane through a C-terminal transmembrane α helix in its small subunit and a membrane associated b-type cytochrome containing a heme center (*67*). While the exact biological function of EcHyd-1 is not completely known, it is thought to oxidize hydrogen, which is coupled to quinone reduction through its innate cytochrome (*67*).

Biological redox pathways, such as photosynthesis or oxidative phosphorylation, transfer and accept electrons in sequence across a structural scaffold such as a membrane. Transfer processes are protected from potential oxidative interruption by using electron

carriers such as NADH which shuttle electrons into complex membrane domains composed of iron sulfur clusters and heme centers (*117*). The efficiency of these processes is facilitated by precise co-localization and recognition of subsequent molecular mediators. Cytochrome-hydrogenase complexes are unstable once removed from the membrane making their structural biology and thus, biochemistry challenging (*67*). However, a crystal structure of a hydrogenase (EcHyd-1) in complex with its innate redox partner (cytochrome b) has recently been solved (*67*) with evidence showing the cytochrome b can be reduced by H_2 (*67*). This shows the first direct electronic coupling of a hydrogenase redox partner to a hydrogenase guided by high resolution structural biology.

Previously, we fused the subunits of the EcHyd-1 heterodimer (hyaA; hyaB) to the N-termini of different scaffold proteins and enforced the heterodimer through directed self-assembly of the P22 capsid (Fig. 5.1a).

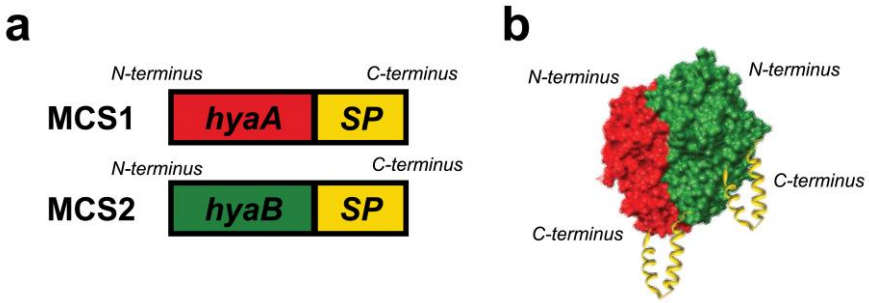

Figure 5.1 The Molecular Biology Design for Encapsulation of the EcHyd-1 using Two SP. The molecular biology deisgn for the hydrogenase assembly plasmid (a) consists of two multiple-cloning sites (MCS). The EcHyd-1 small subunit (hyaA) was fused, at its C-terminus, to the N-terminus of the P22 scaffold protein (SP). The C-terminal transmembrane domain of the hyaA was removed. The EcHyd-1 large subunit (hyaB) was fused to the N-terminus of the scaffold protein.

The expression design used a maturation of the hydrogenase components on one plasmid, under the control of IPTG prior to expression of the P22 coat protein under the control of different inducer, L-arabinose. The active site components (hyaA; hyaB) were matured using basal expression of endogenous accessory proteins found within the *E. coli* expression host. As an extension of this P22-encapsulated hydrogenase design, here we functionally integrated a biological electron mediator (cytochrome b_5; Cb_5) and its associated reductase (NADH-dependent cytochrome b_5 reductase; Cb_5r) with the EcHyd-1 hydrogenase within the P22 capsid.

The Cb_5 contains a heme center that is reduced by its natural redox partner, Cb_5r(*118*). The monomeric Cb_5r is an NADH-dependent flavoprotein that naturally catalyzes the two electron transfer from NADH to the heme containing $Cb_{5(119)}$. Inspired by the orientation and proximity of the cytochrome b on the C-terminal extension of the EcHyd-1 small subunit, we used molecular biology (Fig. 5.2b) to attach the Cb_5 to the EcHyd-1 small subunit, by placing the gene for the Cb_5 in between the scaffold protein (SP) and the small subunit of the hydrogenase with a flexible linker (Fig. 5.2b). In the EcHyd-1 dimer, the hyaB N-terminus points away from the C-terminus. Therefore, the redox partner of the Cb5, the NADH-dependent cytochrome b_5 reductase, was cloned onto the on the C-terminus of hyaB, with a small flexible linker (Figure 5.2b). The extreme C-terminus of the P22 scaffold protein composed of a helix-turn-helix and is responsible for binding with the coat protein, but the N-terminus can be modified without affecting assembly of the P22 capsids. Our previous work demonstrated the directed encapsulation of an active hydrogenase within the P22 capsids using two different

scaffold proteins with the two subunits of the EcHyd-1. The new design presented here builds upon this success through the addition of a redox pair in order to catalyze the production of hydrogen from NADH and avoiding the use of small molecule electron mediators. This approach exemplifies the advantages of co-localizing a multi-component system using a bacterial expression system.

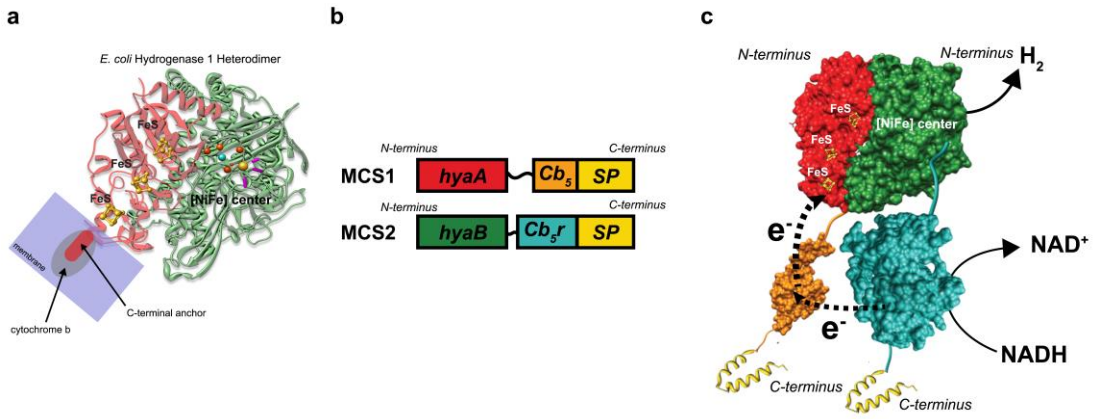

Figure 5.2 The Biological Inspiration, Design Strategy Using Molecular Biology, and Bio-Inspired Synthetic Target. The *E. coli* [NiFe]-hydrogenase 1 ("EcHyd-1") is a heterodimer (a) built from a large subunit (green) and small subunit (red) with an associated redox-partner on its extreme C-terminus, cytochrome b. The design strategy (b) uses an alternative cytochrome b_5 with its associated NADH-dependent cytochrome b_5 reductase (MCS = multiple-cloning site). The Cb_5/Cb_5r was incorporated with EcHyd-1 using molecular biology to facilitate electron transfer (c) between the components.

Results

Molecular biology was used to engineer the cytochrome b_5 and NADH-dependent cytochrome b_5 reductase into the hydrogenase plasmid (containing the large and small subunits of [NiFe]-hydrogenase 1, "EcHyd-1") to maximize electron flow (Fig. 5.2b). In

the *in vivo* assembly of the P22 procapsid, the scaffold protein (SP) directs cargo to the interior, generating particles nearly identical to wild-type P22 procapsids. We used this established approach to package both subunits of the EcHyd-1 heterodimer with each subunit of the heterodimer fused to a different SP, in roughly equal proportions.

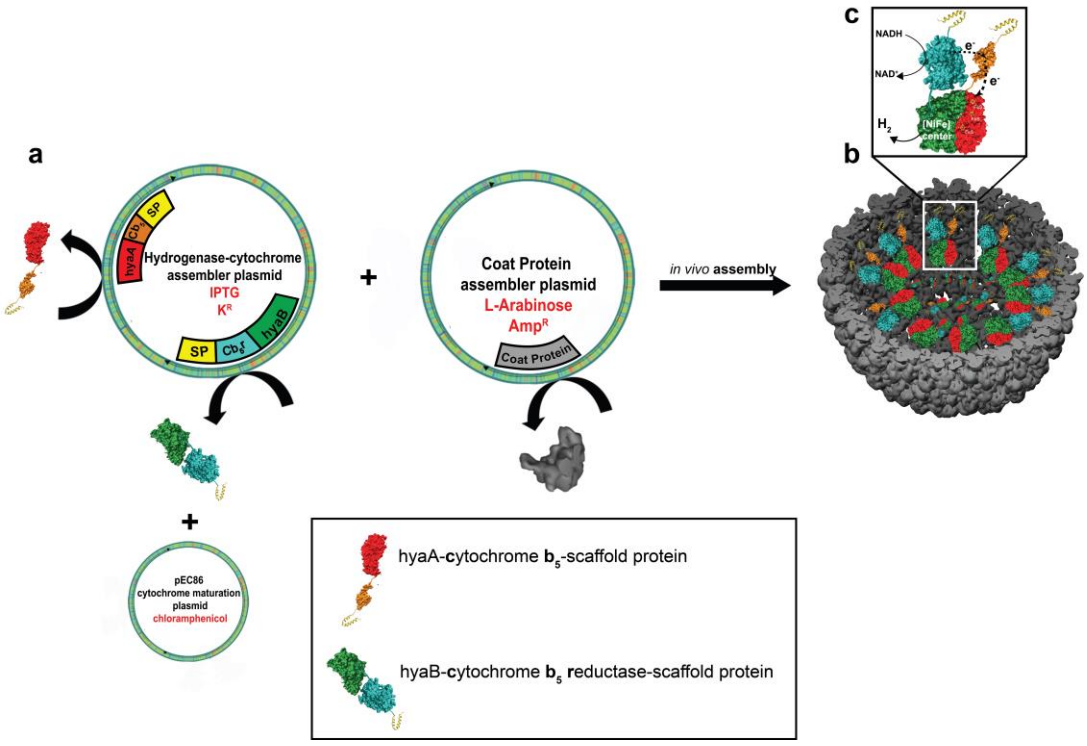

Figure 5.3 The Generation of P22-Hyd$_{cyt}$ Through a Multi-Plasmid Expression System. A plasmid (a) harboring the hyaA-Cb$_5$-SP and hyaB-Cb$_5$r-SP is co-expressed with the pEC86 cytochrome maturation plasmid under the control of IPTG prior to the expression of the P22 coat protein which is under the control of a separate promoter. This expression system yields the P22-Hyd$_{cyt}$ as shown in (b) that generates hydrogen through the addition of a single substrate NADH as depicted in (c) through an extended electron wire.

Previous work has shown the catalytic importance of a delayed, differential expression of the hydrogenase alone prior to expression of the coat protein using a two plasmid expression system. This delay allowed for maturation of the EcHyd-1

hydrogenase by endogenous accessory proteins found in the expression host prior to expression of the P22 coat protein and packaging within the P22 capsid interior. *E. coli* hydrogenase 1 (EcHyd-1) is encoded by a 6 gene operon (*hya*ABCDEF). Two of these genes (*hya*A and *hya*B) encode for the small and large subunits of the hydrogenase heterodimer. The gene products of *hya*CDEF and other maturation proteins found in the *E. coli* expression host play essential roles in maturation of the [NiFe] active site. They are essential for an active hydrogenase. In this complex extension of the hydrogenase construct, where a cytochrome b_5/cytochrome b_5 reductase has been incorporated, we again used this delayed, differential expression of the cargo prior to encapsulation and expression of the CP (under the control of a different promoter). Our hypothesis was that this would allow for the maturation and loading of the hydrogenase active sites, as well as the cytochrome b_5 containing a heme center.

E. coli expression and loading of heme containing cytochromes is often low and to overcome this we introduced a third plasmid, pEC86, which is known to enhance this process(*120*). The pEC86 contains the genes for a set of *E. coli* cytochrome maturation genes *ccmABCDEFGH*. Co-expression of this plasmid in *E. coli* with a separate plasmid containing a cytochrome is known to enhance heme loading of cytochromes.

In order to generate P22-$Hyd_{cyt,}$ we co-expressed three plasmids (all with different resistances) in one cell: (1) the plasmid containing the cytochrome/hydrogenase (hyaA-Cb_5-SP; hyaB-Cb_5r-SP) with (2) a plasmid (pEC86) for the expression of cytochromes in *E. coli* and (3) the P22 coat protein (CP). BL21(DE3) *E. coli* were co-transformed with the 3 plasmids, grown at 22˚C in a modified terrific broth to mid-log and induced with

IPTG with δ-Aminolevulinic acid to aid in heme biosynthesis(*121*). The growth media was supplemented with nickel, iron, and thiamine to aid in hydrogenase and cytochrome active site loading. The *E. coli* were grown for 48 hours, consistent with previous expression times of cytochromes reporting in the literature, followed by the induction of the coat protein for 2 hours under the control of L-arabinose(*121*). Experiments where the pEC86 plasmid was not expressed with the cytochrome-hydrogenase plasmid or when the expression and maturation of the cargo proteins was shortened to between 2-20 hours did not result in heme loaded cytochrome. This led to our hypothesis that 48 hours under IPTG control followed by 2 hours under L-arabinose was a nearly-optimized expression duration.

The capsids grown for this nearly-optimized time were purified by ultracentrifugation using a 35% sucrose cushion and size-exclusion chromatography followed by CsCl gradient. The purified P22-Hyd_{cyt} particles were subjected to SDS-PAGE (5.4c), which demonstrated bands matching expected molecular weights of the CP (46 kDa), hyaA-Cb_5-SP (68 kDa), hyaB-Cb_5r-SP (116 kDa). This clearly indicates the packaging of both components of the cargo expression. Further analysis of this purified P22-Hyd_{cyt} by SEC-MALS/QELS showed an average particle molecular weight of 32.3 MDa (5.3b). After accounting for the molecular weight of the coat protein (19.7 MDa), this indicates the packaging of approximately 69 copies of cargo protein. The particle diameters (R_g = 23.3 ± 0.1; R_h = 26.1 ± 0.3; R_g/R_h = 0.89) were similar to wild-type P22 virus particles (54-58 nm). When visualized by transmission electron microscopy (TEM), the purified capsids revealed a population of particles similar in diameter and

morphology to wild-type P22 procapsids (Fig. 5.4a). The results of these biophysical tools prove that the packaging of this multimeric cargo does not disrupt the assembly of icosahedral procapsids.

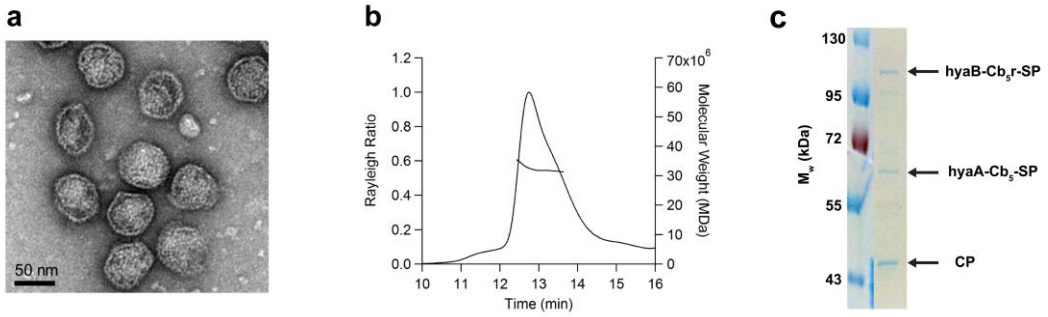

Figure 5.4 Biophysical Characterization of the P22-Hyd_{cyt} Reveals a Monodisperse Population of Particles. Transmission electron microscopy (TEM) of the P22-Hyd_{cyt} (a) when stained using uranyl acetate show a monodisperse set of virus-like particles consistent with T=7 icosahedral symmetry. Analysis by size-exclusion chromatography-multi-angle light scattering (b) indicates particles have an average molecular weight of (32.3 MDa) demonstrating packaging of the hyaA-Cb5-SP and hyaB-Cb5r-SP.

The hypothesis of this catalytic system was that upon addition of substrate for the reductase (NADH), electrons would be transferred by the two electron carrier NADH through the noncovalently bound flavin (FAD). It is well established in non-encapsulated systems that two electrons are transferred to the oxidized flavin which becomes fully reduced ($FADH^-$) and transfers single electrons to the one electron acceptor, Cb_5, which contains a heme center (Fig 5.5). A previous report has also shown that the Cb_5 cannot be reduced by NADH alone and it only accept electrons through the cytochrome b_5 reductase(*121*). Upon electron transfer to the cytochrome, electrons would then flow through the three FeS centers of the small subunit hydrogenase, critical for the oxygen

tolerance of the [NiFe]-hydrogenase 1, then into the [NiFe] center generating hydrogen.

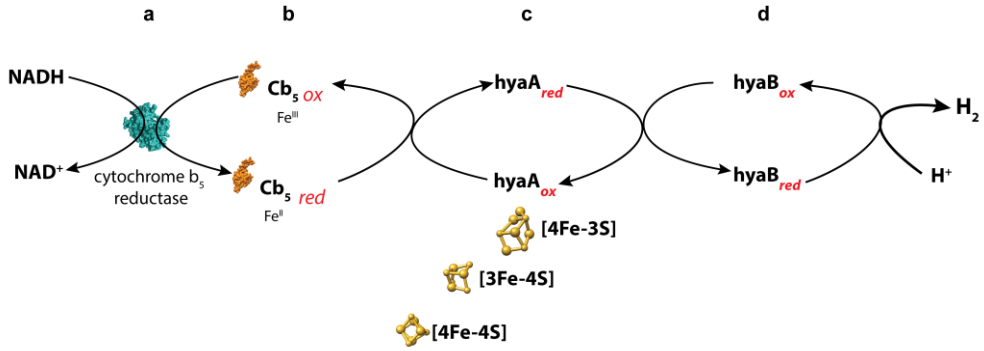

Figure 5.5 The Proposed Catalytic Cycle of the P22-Hyd$_{cyt}$. The catalytic cycle of the P22-Hyd$_{cyt}$ is composed of the cytochrome b_5 reductase (a) which catalyzes the two electron transfer from NADH to cytochrome b5 (b). Electrons passed through the iron sulfur clusters (c) which are then fed into the large subunit active site (d) for hydrogen production driven by NADH input.

We expected that upon encapsulation, given the crowded capsid interior, that this sequence of electron transfer events would likely be maintained.

Cb$_5$r activity was monitored (Fig. 5.6a) through NADH loss at 340 nm, using concentrations of NADH well-above the reported K_m, (1.1 μM) for similar enzymes (*122*) which revealed an activity of 27.4 ± 3.2 nmol NADH lost/min at pH 5. The P22-Hyd$_{cyt}$ was assayed for hydrogen production (Fig. 5.6b) and demonstrated a rate of 20.9 ± 3 nmol H_2/min. The activity of EcHyd-1, a component of this system, is pH dependent and the activity of both the Cb5/Cb5$_r$ with the cytochrome was assayed for activity between pH 5 and 6 (Fig. 5.5).

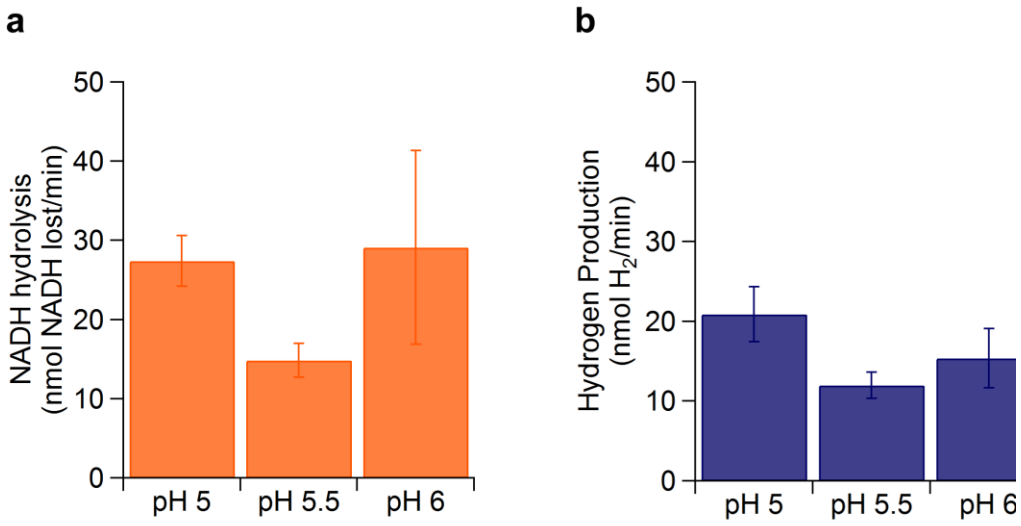

Figure 5.6 The Activities of the Cytochrome b_5 Reductase and Hydrogenase Components of the P22-Hyd_{cyt}. The two component system of the P22-Hyd_{cyt} consists of the NADH-dependent cytochrome b5 reductase (Cb_5r) and the hydrogenase. The activity of the Cb5r was monitored by NADH loss at 340 nm (a) simultaneously with the activity of the hydrogenase component measured by gas chromatography (b).

Previous 3D Cryo-Electron Microscopy (Cryo-EM) work on cargo loaded P22 has probed cargo-protein and cargo-cargo interactions using either monomeric (EGFP) or tetrameric (CelB) proteins packaged within the P22 capsid(*123*). The results of this work show that the CelB-P22 and EGFP-P22 constructs, when analyzed by Cryo-EM, exhibit electron density corresponding to the cargo that is confined to the interior capsid lumen. The P22-Hyd_{cyt} is more complex in terms of cargo size and enzymatic function than these previous systems. This prompted us to investigate using Cryo-EM the effects of packaging the cytochrome-hydrogenase multimeric complex on both the capsid and cargo structure (Fig. 5.7). 3D reconstruction (11.8 Å) of the purified P22-Hyd_{cyt} with

icosahedral averaging clearly shows T=7 icoshedral particles (5.7a). This indicates the directed encapsulation of two concatenated fusions (hyaA-Cb_5-SP; hyaB-Cb_5r-SP) does not disrupt the assembly of the capsid shell.

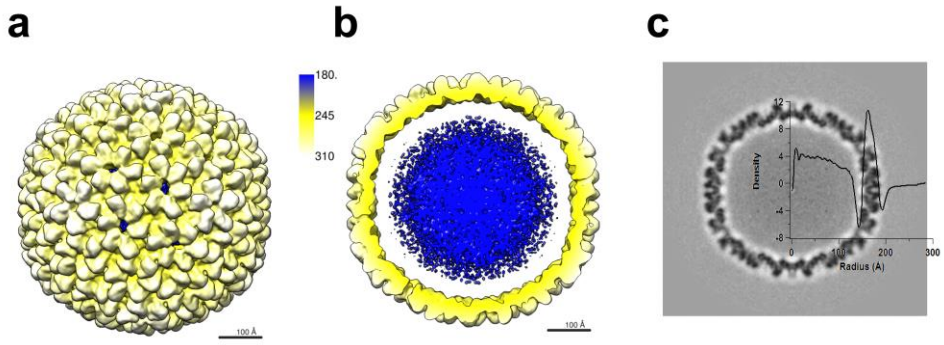

Figure 5.7 3D Cryo-Electron Microscopy of P22-Hyd_{cyt}. The structure (a) of the P22-Hyd_{cyt} clearly shows a T=7 organization. Central slices of representative particles in (b) and (c) at 11.8Å with imposed icosahedral symmetry clearly shows internal density concentrated towards the center of the particles.

It known that the SP without a cargo protein binds to the interior P22 capsid walls through highly defined interactions. Central slices of the P22-Hyd_{cyt} show internal density that is higher than outside the particles. Yet, central slices of the P22-Hyd_{cyt} with imposed icosahedral averaging (Fig. 5.7b and 5.7c) show distributed electron density on the capsid interior that is not strictly confined to the interior capsid lumen as in data observed with EGFP-P22 and CelB-P22. Clearly, the size and possibility the complexity of the cytochrome-hydrogenase is affecting the electron density observed. While the 3D reconstruction does not provide insights into the quaternary structure of the hyaA-Cb_5-SP, hyaB-Cb_5r-SP on the capsid interior, further work may elucidate the structural effects

of confinement complex enzymatic systems like this for the development of capsid-based materials.

Discussion and Conclusions

In the present work, we have shown the extension of an electron wire of the hydrogenase with a cytochrome b_5/cytochrome b_5 reductase designed within a robust virus capsid. In its native form, the electron wire of the EcHyd-1 hydrogenase consists of a cytochrome b linked through a transmembrane domain to the small subunit FeS clusters linked to the [NiFe] center. We have taken inspiration from this example from nature to enhance a highly active, encapsulated hydrogenase using the P22 capsid. Using design at the level of molecular biology, the electron wire was extended by directly linking a heme protein, cytochrome b_5 to the small subunit of the hydrogenase with its associated NADH-dependent cytochrome b_5 reductase attached to the C-terminus of the large subunit. This design incorporates a different scaffold protein onto the two components of this system to drive packaging to a confined, capsid interior and spatially separating from the environment. The quaternary structure of the previous construct (P22-Hyd) consisting of the only the hydrogenase components was important for the greatest activity. While we cannot comment on the resulting quaternary structure of this updated cytochrome b_5/cytochrome b_5 reductase/hydrogenase on the capsid interior, we have shown that all components of this system (Cb_5r and hydrogenase) are active to drive the production of hydrogen.

This data presents a large step forward from the initial design of the hydrogenase. Further characterization of the P22-Hyd_{cyt} will require a further optimization of the cargo/capsid expression timing with a more detailed analysis of the metal loading, an understanding of the quaternary structure, guided by the structure, of the encapsulated species with the possibility of enforcing the dimerization of the two components through a designed dimerization domain. It will also be necessary to provide initial spectroscopic data to conclusively identify the hydrogenase active site if this cannot be completed using Cryo-EM.

Acknowledgements

We acknowledge Marcellus Ubbink (Leiden University, Netherlands) and Miguel De la Rosa (University of Seville, Spain) for the generous gift of the pEC86 plasmid.

Methods

Cloning and Molecular Biology

A previous plasmid (MCS2: 6x-His-hyaB-SP; MCS1: 6xHis-hyaA-SP; pRSF K^R) was linearized between hyaA and SP by digestion with *Bgl* II and dephosphorylated with Antarctic Phosphatase. Cb_5 was digested with *Bgl* II from a pUC57 containing the genes for the Cb_5/Cb_5r (*Sus scrof*a) that were synthesized and codon optimized by Genewiz (South Plainfield, NJ). The Cb_5 insert was ligated into the vector and the insert orientation was confirmed by restriction enzyme mapping (*Sca I* and *Xho* I double digestion). The 6xHis-hyaB-SP insert was removed from the plasmid with *Nco* I and *Sac* I and ligated into the corresponding site of a transfer pBAD vector. An *Spe* I cloning site

was inserted between hyaB and SP by site-directed mutagenesis [*Forward* primer: GGT GGC ACT AGT GGT CGC AGC AAT GCC GTA GCA GAA CAG]; [*Reverse* primer: ACC CGC GCT GCC ACG CAC CTG CAC GGA GAT CAG] using the Q5 Site-Directed Mutagenesis Kit (New England Biolabs, Inc., Ipswich, MA). The new *Spe* I-site was confirmed by restriction enzyme digestion. Cb_5r was amplified from the same pUC57 plasmid using the following primers containing *Spe* I-site for cloning: [*Forward* AAA AAA ACT AGT AGC ACC CCT GCC ATT ACC CTG]; [*Reverse* AAA AAA ACT AGT AAA GGC AAA ACA GCG CTC CTT CGG].

The PCR product was gel purified, digested with *Spe* I, column purified, and ligated into the *Spe* I-digested and Antarctic Phosphatase dephosphorylated vector. The orientation of the Cb_5r was determined by digestion with *Bgl* II. The 6xHis-hyaB-Cb_5r-SP insert was digested from the vector with *Nco* I and *Sac* I and ligated into the corresponding site in pRSFDuet1::hyaA-Cb_5-SP142-303. The construct was confirmed by DNA sequencing. (Eurofins, Louiseville, KY). All enzymes were from New England Biolabs, Inc.

Protein Expression, Purification, and Characterization

E. coli strains containing three plasmids ([*hyaA-Cb_5-SP] + [hyaB-Cb_5r-SP]* in pRSF, pEC86 and P22 CP in pBad HisA were grown at 100 rpm at 22˚C in terrific broth supplemented with ammonium iron (II) sulfate hexahydrate (1 mM, final), nickel(II) chloride monohydrate (1 mM, final), and thiamine (1 mM, final) in the presence presence of carbenicillin (50 mg/mL), kanamyacin (15 mg/mL), and chloramphenicol (34 mg/mL). The expression of hyaA-Cb_5-SP + hyaB-Cb_5r-SP was induced by addition of IPTG to a

final concentration of 40 μM at OD_{600}=0.6 with delta-aminolevulinic acid (1 mM final). Cultures were grown for 48 hours followed by induction of the CP was under L-arabinose control (0.02%, final) and grown for 1 hour. The cells were harvested by centrifugation at 3700 rpm for 20 min, resuspended in a lysis buffer (100 mM Trizma Base, 100 mM NaCl, pH 7.6) and frozen at -80˚C overnight. The resuspended cell pellet was thawed, treated with DNase (20 mg/mL), RNAse (30 mg/ML), and lysosome (15 mg/mL) for 30 min at room temperature with rocking. The cell suspension was lysed by sonication and centrifuged at 12,000 rpm for 45 minutes at 4°C. The supernatant was then loaded onto a 35% (w/v) sucrose cushion and ultracentrifuged at 45,000 rpm for 50 minutes using a FiberLite F50L-9X39 rotor on a Sorvall WX Ultra 80 Series Centrifuge. The resulting pellet was resuspended in 100 mM Trizma base, 100 mM NaCl (pH 8), purified by an isopycnic 1.20-1.40 (g/mL) CsCl density gradient, followed by SEC on a Sephacryl S-500 column using a Biologic DuoFlow FPLC (Bio-Rad, Hercules, CA) running at 0.5 mL/min. Fractions were pooled, concentrated by ultracentrifugation and resuspended in the buffer (50 mM Trizma Base, 50 mM NaCl, pH 7.6).

SEC-MALS/QELS

Samples (25 μL) were separated (0.7 ml/min) over a WTC-200S5 (Wyatt Technologies, Santa Barbara, CA) size exclusion column utilizing an Agilent 1200 HPLC in buffer (50 mM sodium phosphate, 100 mM NaCl, 200 ppm sodium azide, pH 7.2). Samples were detected using a UV detector (Agilent), a Wyatt HELEOS Multi Angle Laser Light Scattering (MALS) detector, a Wyatt Quasi Elastic Light Scattering detector and Wyatt Optilab rEX differential refractometer (Wyatt Technologies, Santa Barbara,

CA). Using the elution-profile data, the number-averaged molecular mass was calculated using Astra 6.1.2 software (Wyatt Technologies, Santa Barbara, CA) using a dn/dc for protein of 0.185.

P22-Hyd_{cyt} Cryo-EM

For reference-free 2-D classification, a total of 4483 particles were classified using maximum likelihood algorithm in the Relion program (version 1.4)(*124*). Two classes (1698 particles) having more internal density were combined for further classification. For 3-D image reconstruction, an initial 3-D model was generated from 350 particles using *ab initio* random model method implemented in AUTO3DEM (version 4.05)(*125, 126*). Origin and orientation searches were carried out iteratively using PPFT and further refined by PO2R. A total number of 7805 particles were used to generate the final 3-D reconstruction. The resolution was estimated to 11.8Å using Fourier shell correlation at 0.5. The 3-D reconstruction were visualized using Robem and Chimera(*127*).

Cb_5r and Hydrogenase Activity Assay

The protein sample (20-100 μL, 1-5 mg/mL) in buffer (50 mM sodium citrate, 50 mM NaCl, pH 4-6) was combined with 50 μM FAD (Acros Organics, Morris Plains, NJ) and degassed using vacuum and flushed with argon in either a crimp top cuvette to simultaneously monitor NADH loss and H_2 production. The sample was treated with hydrogen to prime the hydrogenase and then extensively degassed and purged with argon to remove all residual hydrogen. NADH (GoldBio, St. Louis, MO) was previously degassed under vacuum and purged with argon and added to the solution (5 μL, 300 μM,

final). Hydrogen evolution was measured in the space of the respective apparatuses using a Shimadzu GC-8A TCD with a 0.61 m x 0.64 cm 40/60 Carboxen 1000 Supelco column using an argon carrier gas. Bulk H_2 gas was used to quantify the H_2 production. NADH loss was monitored by absorbance at 340 nm using an Agilent 8453 UV/Vis Spectrophotometer with a multi-cell changer.

Amino Acid Sequence of the 6xHis-hyaB-Cb_5r-SP

MGSSHHHHHHMSTQYETQGYTINNAGRRLVVDPITRIEGHMRCEVNIND
QNVITNAVSCGTMFRGLEIILQGRDPRDAWAFVERICGVCTGVHALASVYAIEDA
IGIKVPDNANIIRNIMLATLWCHDHLVHFYQLAGMDWIDVLDALKADPRKTSEL
AQSLSSWPKSSPGYFFDVQNRLKKFVEGGQLGIFRNGYWGHPQYKLPPEANLM
GFAHYLEALDFQREIVKIHAVFGGKNPHPNWIVGGMPCAINIDESGAVGAVNME
RLNLVQSIITRTADFINNVMIPDALAIGQFNKPWSEIGTGLSDKCVLSYGAFPDIA
NDFGEKSLLMPGGAVINGDFNNVLPVDLVDPQQVQEFVDHAWYRYPNDQVGR
HPFDGITDPWYNPGDVKGSDTNIQQLNEQERYSWIKAPRWRGNAMEVGPLART
LIAYHKGDAATVESVDRMMSALNLPLSGIQSTLGRILCRAHEAQWAAGKLQYFF
DKLMTNLKNGNLATASTEKWEPATWPTECRGVGFTEAPRGALGHWAAIRDGKI
DLYQCVVPTTWNASPRDPKGQIGAYEAALMNTKMAIPEQPLEILRTLHSFDPCLA
CSTHVLGDDGSELISVQVRGSAGGGTSSTPAITLENPDIKYPLRLIDKEVVNHDTR
RFRFALPSPEHILGLPVGQHIYLSARIDGNLVIRPYTPVSSDDDKGFVDLVIKVYFK
DTHPKFPAGGKMSQYLESMKIGDTIEFRGPNGLLVYQGKGKFAIRPDKKSSPVIK
TVKSVGMIAGGTGITPMLQVIRAIMKDPDDHTVCHLLFANQTEKDILLRPELEEL
RNEHSARFKLWYTVDRAPEAWDYSQGFVNEEMIRDHLPPPEEEPLVLMCGPPPM

IQYACLPNLERVGHPKERCFAFTSGRSNAVAEQGRKTQEFTQQSAQYVEAARKH
YDAAEKLNIPDYQEKEDAFMQLVPPAVGADIMRLFPEKSAALMYHLGANPEKA
RQLLAMDGQSALIELTRLSERLTLKPRGKQISSAPHADQPITGDVSAANKDAIRK
QMDAAASKGDVETYRKLKAKLKGIR

Amino Acid Sequence of the 6xHis-hyaA-Cb_5-SP

MGGSHHHHHHGGGNNEETFYQAMRRQGVTRRSFLKYCSLAATSLGLGA
GMAPKIAWALENKPRIPVVWIHGLECTCCTESFIRSAHPLAKDVILSLISLDYDDT
LMAAAGTQAEEVFEDIITQYNGKYILAVEGNPPLGEQGMFCISSGRPFIEKLKRAA
AGASAIIAWGTCASWGCVQAARPNPTQATPIDKVITDKPIIKVPGCPPIPDVMSAII
TYMVTFDRLPDVDRMGRPLMFYGQRIHDKCYRRAHFDAGEFVQSWDDDAARK
GYCLYKMGCKGPTTYNACSSTRWNDGVSFPIQSGHGCLGCAENGFWDRGSFYS
RVVDIPQMGTRSGSAGGGGTGGAGAEQSDKAVKYYTLEEIQKHNNSKSTWLILH
HKVYDLTKFLEEHPGGEEVLREQAGGDATENFEDVGHSTDARELSKTFIIGELHP
DDRSKIAKPSETLITTVESNSSAGGGTGRSCRSNAVAEQGRKTQEFTQQSAQYVE
AARKHYDAAEKLNIPDYQEKEDAFMQLVPPAVGADIMRLFPEKSAVLMYHLGA
NPEKARQLLAMDGQSALIELTRLSERLTLKPRGKQISSAPHADQPITGDVSAANK
DAIRKQMDAAASKGDVETYRKLKAKLKGIRS

CHAPTER SIX

LOCATION OF THE BACTERIOPHAGE P22 COAT PROTEIN C-TEMRINUS PRIVIDES OPPORTUNITIES FOR THE DESIGN OF CAPSID-BASED MATERIALS

Contribution of Authors and Co-Authors

Manuscript in Chapter 6

Author: Amy Servid

Contributions: Carried out genetic modifications, expressed and characterized each of the P22 capsids, designed studies, and wrote the manuscript.

Co-Author: Paul Jordan

Contributions: Cloned the 6xHis-SP141 into the pRSF vector used for expression, critically read, and edited the manuscript.

Co-Author: Alison O'Neil

Contributions: Provided an expression vector containing mCherry=SP141(C140), critically read and edited the manuscript.

Senior Co-author: Peter Prevelige

Contributions: Critically read and edited the manuscript.

Senior Co-author: Trevor Douglas

Contributions: Obtained funding for the research, designed studies, assisted with writing and editing of the manuscript.

Manuscript Information Page

Amy Servid, Paul Jordan, Alison O'Neil, Peter Prevelige, Trevor Douglas
ACS Biomacromolecules
Status of Manuscript:
____ Prepared for submission to a peer-reviewed journal
____ Officially submitted to a peer-review journal
____ Accepted by a peer-reviewed journal
__X_ Published in a peer-reviewed journal

Published by ACS Biomacromolecules
Appeared in print: August 20, 2013
Published in: Volume 14, Issue 9, Pages 2989-2995

CHAPTER SIX

LOCATION OF THE BACTERIOPHAGE P22 COAT PROTEIN C-TERMINUS PROVIDES OPPORTUNITIES FOR THE DESIGN OF CAPSID-BASED MATERIALS

Published In; *Biomacromolecules,* **2013**, 14, 2989-2995

Amy Servid[1], Paul Jordan[1], Alison O'Neil[1], Peter Prevelige[2], Trevor Douglas[1]

[1]*Department of Chemistry and Biochemistry, Montana State University, Bozeman, Montana, 59717*
Department of Microbiology, University of Alabama at Birmingham, Birmingham, Alabama, 35294

Supporting Information Containing in Appendix C

Abstract

Rational design of modifications to the interior and exterior surfaces of virus-like particles (VLPs) for future therapeutic and materials applications is based on structural information about the capsid. Existing cryo-electron microscopy based models suggest that the C-terminus of the bacteriophage P22 coat protein (CP) extends towards the capsid exterior. Our biochemical analysis through genetic manipulations of the C-terminus supports the model where the CP C-terminus is exposed on the exterior of the P22 capsid. Capsids displaying a 6xHis tag appended to the CP C-terminus bind to a Ni affinity column, and the addition of positively or negatively charged coiled coil peptides to the capsid results in association of these capsids upon mixing. Additionally, a single cysteine appended to the CP C-terminus results in the formation of intercapsid disulfide bonds and can serve as a site for chemical modifications. Thus, the C-terminus is a

powerful location for multivalent display of peptides that facilitate nanoscale assembly and capsid modification.

Introduction

Viruses are increasingly recognized as useful templates for both hard and soft materials applications(*128-130*). The multifunctional, and highly symmetric organization of subunits in the viral capsids provide for a unique environment for functional group display and modification(*131, 132*). Knowledge about the structure and assembly of virus capsids aids their use as powerful platforms for functional nanomaterials design and synthesis(*133-139*). The assembly of repeating subunits into capsids generates highly monodisperse multivalent nanoparticles with distinct interior and exterior surfaces that can be used for encapsulation and/or display(*140, 141*). Encapsulated cargo is sequestered from the surrounding environment, while modifications on the capsid exterior display functionalities that interact directly with the bulk environment.

The capsid derived from the bacteriophage P22 is a robust nanocontainer that has been extensively used for directed encapsulation(*142*) and surface display(*143*), and its use as a biomaterial is completely decoupled from the infectious virus. The non-infectious P22 procapsid (PC) assembles in vivo (in *E. coli*) from 420 copies of coat protein with the aid of the P22 scaffold protein (SP)(*44*), which can be truncated to include only residues 141-303 and still template assembly of a T=7 virus like particle(*51*). The truncated SP (SP141) is packaged on the interior of the 60 nm diameter procapsid and by fusing cargo proteins to the N-terminus can act as a means to direct the

packaging inside the P22 capsid(*59*). Previously we have genetically engineered cysteine residues into the P22 coat protein on the interior (S39C, K118C)(*53, 144*) and exterior (T183C)(*143*) of the assembled P22 capsid to utilize as sites for chemical conjugation.

For the surface display of peptides, a genetic fusion approach is advantageous over chemical conjugation because the stoichiometry of the peptide display is defined by the quaternary structure, and the capsid self-assembles *in vivo* requiring less processing and a more homogeneous end product. One flexible loop on the capsid exterior has been identified as a potential site for the display of short peptides but does not tolerate large inserts or highly charged peptides(*143*). The availability of another, more robust, site for genetic display on the capsid exterior would expand the versatility and application of the P22 nanoplatform. The available models of the P22 capsid (from cryo-TEM)(*145, 146*) suggest that the C-terminal residues of the CP extend toward the exterior of the capsid. However, the models do not include the location of the last few residues of the P22 CP.

Here we have investigated the location of the CP C-terminus in the P22 procapsid by genetically engineering fusion peptides to the C-terminal of the CP and investigating the biochemical presentation of peptides to the exterior environment of the capsid. Natural and synthetic systems utilize coiled coil motifs(*147-153*) to promote hierarchical assembly, so we have explored the presentation of coiled coil peptides on the C-terminus for directed inter-particle interactions. Through these studies, we show that fusions to the C-terminus of the P22 CP do indeed sample the exterior environment, and we demonstrate the utility of this approach for display of peptides that allow manipulation of

the biophysical properties of the capsid and suggest further development of the P22 platform as a functional nanomaterial.

Results

To probe the location of the structurally unresolved C-terminus of the coat protein (CP) in the bacteriophage P22 capsid, a series of genetic mutations were made and biochemically characterized. In the structural model of the P22 procapsid coat protein, the last 5 amino acids are not resolved and their location is ambiguous (Fig 1). However, the published models of the P22 capsid(*145*, *146*) suggest that the C-terminus of the CP is directed towards the exterior of the capsid (S2).

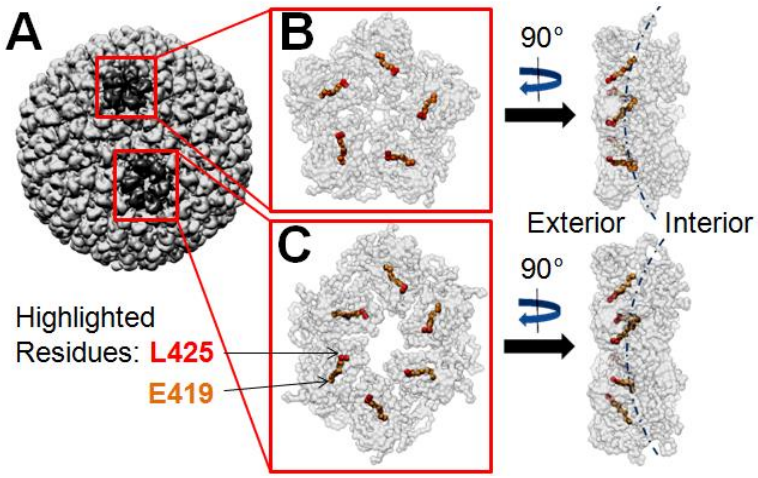

Figure 6.1 A representation of the assembled P22 procapsid (A) from the published cyroEM structure, which includes residues 1-425 of the 430 amino acid P22 coat protein. The residues 419-425 are highlighted in the zoomed versions of the pentamer(B) and hexamer(C) units. In both, it appears that the CP C-terminus extends toward the capsid exterior.

Genetic fusion of short peptides to the C-terminus of the CP was used to test the accessibility of this region to the exterior environment of the P22 procapsid. A 6x-histidine tag, a single cysteine residue, and two coiled coil peptides, were individually fused to the CP C-terminus to create the following new P22 coat protein constructs: CP-431C, CP-6xHis, CP-E-coil, and CP-K-coil. The genetic manipulation was confirmed by DNA sequencing. Each of the four new P22 coat proteins (CP-6xHis, CP-431C, CP-E-coil, and CP-K-coil) were individually co-expressed with a P22 scaffolding protein (SP) to facilitate the self assembly of the procapsids in the *E.coli* expression system. The novel procapsids were purified using the same methodology as used for purification of the wtP22 procapsids(*59*), which included ultracentrifugation through a sucrose cushion, followed by size exclusion chromatography (Sephacryl S-500, Fig. C.3). Analysis of these materials by SDS page gel electrophoresis confirms the presence of both P22 coat protein and scaffold protein (Fig. C.4).

No significant changes in particle assembly were observed upon the addition of amino acids to the C-terminus. The addition of the residues to the CP C-terminus, on the purified P22 constructs, was confirmed by liquid chromatography - mass spectroscopy (LC-MS) analysis (Fig. C.5 and Fig. C.6). By size exclusion chromatography (SEC), all constructs eluted at approximately 65 mL, which is consistent with the elution volume of the assembled wtP22 procapsid (Fig. C.3). The fractions from this peak were pooled and subjected to HPLC-size exclusion chromatography coupled to multi-angle light scattering (MALS) and refractive index detection. Analysis of the light scattering revealed packaged procapsids with particle diameters reflecting that of assembled capsids for each

sample (Fig. C.S7) and all of the capsids had particle RMS radii in the 23-30 nm range and hydrodynamic radii between 25 and 33nm. The mass of each procapsid calculated from multi-angle light scattering was observed to be between 22 and 30 MDa. (Fig. C.7) The radii and mass ranges reflect slight differences in the construct size and packaging of cargo; each individual construct is highly monodisperse (Fig. C.7).

To determine if the coat protein 6xHis tag is exposed on the capsid exterior, three different variants of the P22 procapsid were studied. These P22 variants included CP with C-terminal 6xHis tag combined with a scaffolding protein having a N-terminal 6xHis tag, a wild type CP combined with a scaffolding protein having a N-terminal 6xHis tag, and a wild type CP combined with a wild type scaffold protein (CP-6xHis/6xHis-SP141, wtCP/6xHis-SP141, and wtCP/wtSP, respectively). In each case, the scaffold protein is packaged on the interior of the P22 procapsid. The exposure of the CP-6xHis tag to the exterior of the capsids was probed by binding to a Ni chelate affinity column. The only construct that demonstrated binding to the Ni column was the CP-6xHis/6xHis-SP141, and these capsids could be eluted by an increasing imidazole gradient (Fig 6.2A). In contrast, the wtCP/6xHis-SP141 and wtCP/wtSP samples did not bind to the column (Fig 6.2A). The presence of P22 VLPs in all fractions was confirmed by SDS-PAGE gel (Fig 6.2B). The CP-6xHis/6xHis-SP141 sample exhibited a peak at 2mL corresponding to protein that didn't bind to the column. Analysis of this peak by SDS-PAGE indicates both the absence of P22 CP-6xHis/6xHis-SP141 and the presence of a protein contaminant (Fig 6.2Biv) that appears on an SDS-PAGE gel of the sample prior to affinity chromatography (Fig. C8). The binding of CP-6xHis/6xHis-SP141, but not

wtCP/6xHis-SP141 to the Ni column is a clear indication that the 6xHis tag on the CP is presented to the exterior of the P22 capsid. The lack of binding by the wtCP/6xHis-SP141 construct also strongly suggests that the scaffold protein is sequestered on the interior and does not sample the outside to any significant extent.

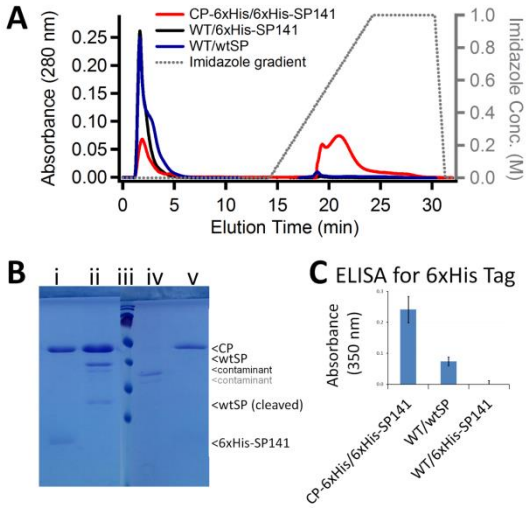

Figure 6.2: Nickel chromatography and ELISA assays with assembled P22 procapsid to determine the exposure of 6xHis tags to the capsid exterior. A) Elution chromatograms of CP-6xHis/6xHis-SP141, wtCP/6xHis-SP141, and wtCP/wtSP from a Ni HisTrap column with increasing imidazole concentration. B) SDS-PAGE analysis of peaks in affinity chromatogram A: i) 2 min elution peak: wtCP/6xHis-SP141, ii) 2 min elution peak: wtCP/wtSP, iii) Page Ruler Molecular Weight standard, and iv) 2min elution peak: CP-6xHis/6xHis-SP141 and v) 21 min elution peak: CP-6xHis/6xHis-SP141. C) Enzyme Linked Immunabsorbent Assay displaying the relative amount of each assembled P22 capsid that interacts with an anti-His antibodv.

Additional data supporting the exposure of the CP-6xHis on the exterior of the procapsid was obtained via an ELISA sandwich assay utilizing a 6xHis tag antibody and a CP specific antibody. A 96 well plate was coated with anti-His tag antibody and each well was subsequently incubated with CP-6xHis/6xHis-SP141, wtCP/6xHis-SP141, or

wtCP/wtSP capsids. The binding of each P22 construct to the anti-His antibody was probed by the CP antibody (rabbit) and subsequently quantified by a secondary goat-anti-rabbit antibody via a horseradish peroxidase/TMB colorimetric assay(*154*). The highest absorbance was observed for the CP-6xHis/6xHis-SP141 construct, while the wtCP/6xHis-SP141 was similar to the background measurement of the assay (Fig 6.2C).

A western blot confirmed that the 6xHis tags were present on 6xHis-SP141, and that they could be recognized by the same anti-His antibody used in the ELISA (Fig. C.8) but only after capsid denaturation. The coat and scaffold proteins were separated by SDS-PAGE and transferred to a nitrocellulose membrane, which was incubated with the mouse anti-His antibody. Bands containing 6xHis tags were subsequently detected using a rabbit-anti-mouse HRP conjugated secondary antibody. Bands corresponding to 6xHis tags on the coat and scaffold were both detectable, while neither the wtCP nor wtSP were highlighted (Fig. C.8). Together, these data are consistent with the suggestion from the structural models and with binding of this construct to the Ni column, indicating that peptides fused to the CP C-terminus are accessible to the capsid exterior while the scaffolding protein is sequestered on the capsid interior. Demonstrating the display of the CP-6xHis on the capsid exterior provides the foundation for future utilization of the CP C-terminal location for the display of targeting peptides or antigenic epitopes.

To further investigate the accessibility of the C-terminus to the capsid exterior, a single cysteine was appended to the C-terminus of the CP (CP-431C/mCherrySP141(C140A)). The addition of a single cysteine residue is less likely to cause alterations in the procapsid structure than longer charged peptides. Successive

quick change mutagenesis steps were carried out on a previously described vector(*59*), resulting in the creation of two unique P22 constructs (wtCP/mCherrySP141 and wtCP/mCherrySP141(C140A), in route to obtaining CP-431C/mCherrySP141(C140A).

To demonstrate the utility of both the C-terminal CP-431C and scaffold protein cysteine (SP-C140) as a sites for chemical conjugation, wtCP/mCherrySP141, wtCP/mCherrySP141(C140A), and CP-431C/mCherrySP141(C140A) were each reacted with fluorescein-5-maleimide (F5M). The F5M labeling of each capsid was quantified by monitoring the UV-visible absorbance of unmodified and F5M reacted capsids under denaturing conditions (Fig. C.9), after separation of free F5M from the capsids by ultracentrifugation through a sucrose cushion. Calculations indicated that F5M labeling resulted in 176 F5M per wtCP/mCherrySP141 capsid and 272 F5M per CP-431C/mCherrySP141(C140A), while only 40 F5M per capsid were observed for the wtCP/mCherrySP141(C140A) capsid (Fig. C.9). Liquid chromatography-mass spectroscopy confirmed the labeling of CP-431C with F5M, while no F5M labeling of the CP was observed for the wtCPmCherrySP141 or wtCP/mCherrySP141(C140A)(S10). These data demonstrate the cysteine packaged inside the wtCP/mCherrySP141 is a useful site for chemical conjugation, and the utility of the procapsid CP C-terminal cysteine chemical conjugation with imaging agents.

In an effort to further confirm the labeling of the wtCP/mCherrySP141, the mass spectroscopy data was analyzed. Under the chromatography and ionization conditions utilized, the P22 CP ionizes much more efficiently than mCherrySP141 or mCherrySP141(C140A). This results in very poor signal intensity and resolution for the

peaks at corresponding to the mCherrySP141 (with a predicted mass of 45962 Da) and mCherrySP141(C140A) (with a predicted mass of 45994 Da) (Fig. C.10). Therefore, any labeling of the scaffold protein could easily be in the baseline noise of the spectrum.

We probed the formation of disulfide bonds in this construct to investigate the ability of the single CP C-terminal cysteine to protrude to the exterior of the capsid, and result in the formation of intercapsid interactions. SEC purified CP-431C/mCherrySP141(C140A) was pelleted by ultracentrifugation and it was observed that, in contrast to the wtCP/mCherrySP141(C140A), this construct did not readily resuspend when incubated at 4ºC overnight. Since the fluorescent protein mCherry is packaged on the capsid interior the difference in the sample behavior was easily observed qualitatively by eye (Fig, C.11), and a comparison of the yield of resupended protein was quantified by UV-visible spectroscopy (Fig. C.11). Relative to the wtCP/mCherrySP141(C140A), only 3% of CP-431C/mCherrySP141(C140A) was recovered (Fig 6.3A).

To confirm that disulfide bond formation played a role in the inefficient resuspension of the CP-431C/mCherrySP141(C140A) construct, the capsid was treated with N-ethyl maleimide to block cysteine thiols. Labeling of the CP subunits was confirmed via liquid chromatography mass spectroscopy analysis, in which all CP subunits were observed to be modified for the CP-431C/mCherrySP141(C140A) construct (Fig 6.3B) while the wtCP/mCherrySP141(C140A) showed no labeling under the same reaction conditions (Fig 6.3C). Excess N-ethyl maleimide (NEM) was purified from the capsids via ultracentrifugation through a sucrose cushion, and SEC-MALS

analysis revealed that the morphology of the capsids was retained after labeling (Fig. C.5).

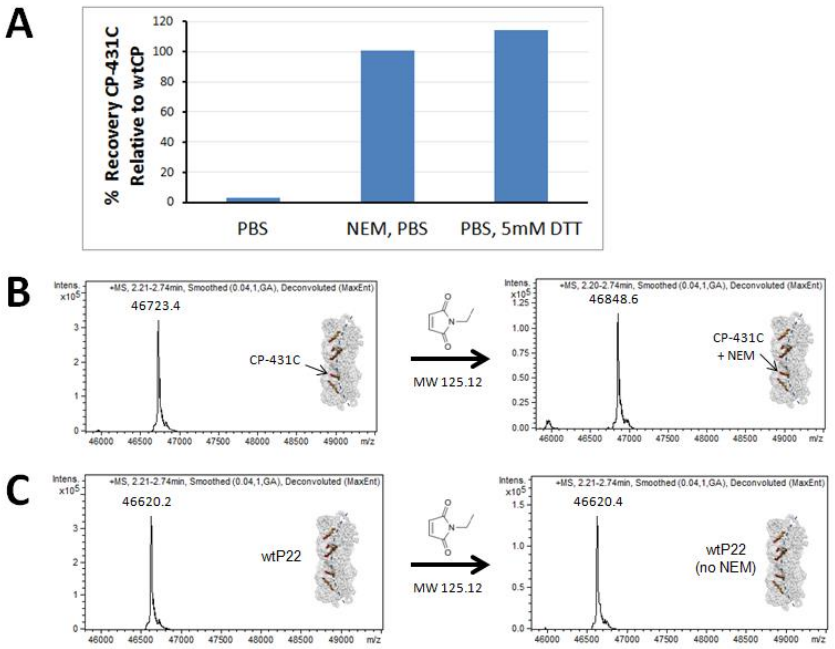

Figure 6.3: Evidence for disulfide bond formation between CP-431C/mCherrySP141(C140A) capsids. A) Bar graph showing the relative yield of soluble CP-431C/mCherrySP141(C140A) protein compared to wtCP/mCherrySP141(C140A) after resuspension in PBS buffer, PBS buffer after blocking CP-431C/mCherrySP141(C140A) with N-ethylmaleimide (NEM) and in PBS buffer and with 5mM DTT. B) Mass spectrum of CP-431C/mCherrySP141(C140A) before and after labeling with NEM. C) Mass spectrum of wtCP/mCherrySP141(C140A) before and after labeling with NEM. The original m/z data is shown in Fig. C.5 and Fig. C.6.

Upon pelleting of the NEM labeled CP-431C/mCherrySP141(C140A), the capsid resuspended in PBS buffer with a recovery identical to wtCP/mCherrySP141(C140A) under these conditions (Fig. 6.3A). This is supporting evidence for the creation of an inter-capsid network from exposed cysteines in CP-431C/mCherrySP141(C140A).

Having evidence for disulfide formation between capsids, we hypothesized that recovery of the CP-431C/mCherrySP141(C140A) construct might be accomplished through the addition of a reducing agent. Upon addition of dithiotheatol (DTT, 5 mM), the CP-431C/mCherrySP141(C140A) construct resuspended with an apparent 114% recovery compared to wt capsid under the same conditions (Fig 6.3A and Fig. C.11). Dynamic light scattering measurements indicated the presence of intact procapsids (average radius of hydration, R_h= 58.6 ± 0.3 nm for wtCP/mCherrySP141(C140A); R_h= 59.3 ± 1.6 nm for CP-431C/mCherrySP141(C140A)) under these reducing conditions for both wtCP/mCherrySP141(C140A) and CP-431C/mCherrySP141(C140A) capsids (Fig. C.12). This provides additional evidence for the existence of disulfide association between CP-431C/mCherrySP141(C140A) capsids.

Building on our demonstrations that peptide extensions to the CP C-terminus are displayed on the capsid exterior and can mediate interparticle interaction, we explored coiled coil motifs to direct interparticle association and assembly. Coiled coil peptides can be described as heptad repeats of amino acids that form superhelical structural motifs when mixed. Strong associations between peptides arise from packing of hydrophobic residues at the interface between the helices and stabilization of the supercoiled structure through electrostatic interactions.

A pair of anti-parallel heterodimeric coiled coil petides was used to transform individual P22 procapsids into building blocks for an extended network structure. Amino acid sequences corresponding to either a positive (CP-K-coil, +TR$(VAALKEK)_3$) or negatively charged (CP-E-coil, +TS$(VAALEKE)_3$) alpha helix of a three heptad

heterodimeric coiled coil motif were appended to the C-terminus of the coat protein. Peptide sequences , $VAALKEK_3$ and $VAALEKE_3$, have been previously described to form a anti-parallel coiled coil heterodimer upon association(*148*). The genetic amenability of the C-terminal location is reflected in the addition of these 23 residues without noticable alterations to the assembly of the P22 procapsid.

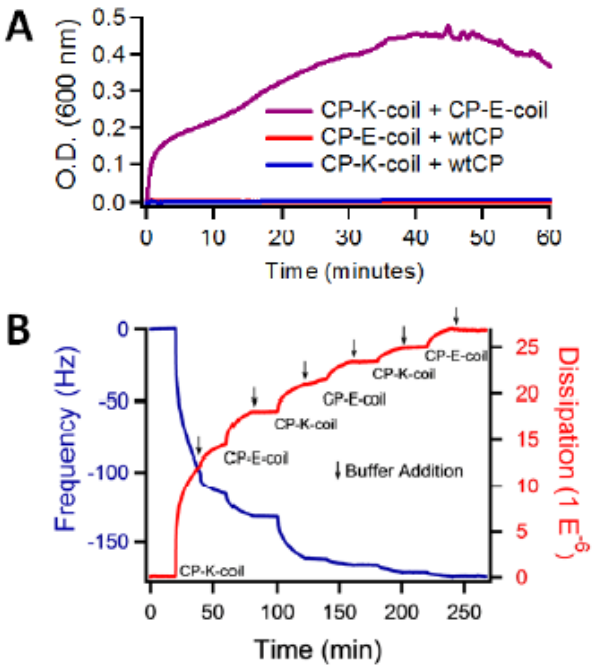

Figure 6.4 Interaction of P22 procapsids displaying K-coil (+TR(VAALKEK)3) or E-coil (+TR(VAALEKE)3) peptides appended to the CP c-terminus. A) UV-visible spectroscopy showing an increase in scattering upon mixing of the E-coil and K-coil capsids relative to each capsid individually or mixtures with wtP22. B) Assembly of K-coil and E-coil capsids on a surface was observed via quartz crystal microbalance with dissipation.

The inherent multivalent interactions between the shorter three heptad-coiled coils on each capsid promote significant capsid interactions, despite having a less thermally stable heterodimer than longer heptad coiled coil repeats(*155*). We used the three-heptad

system in an effort to avoid kinetic traps in material assembly, which are less probable in the particle-particle assembly based upon the cumulative effect of many weak interactions. Upon mixing of solutions containing 0.5 mg/mL of the CP-E-coil and CP-K-coil capsids, a significant increase in light scattering was observed within seconds (Fig. 6.4A), indicating interaction and association of capsids within this mixture to form larger particulates. No increase in scattering was observed with control samples containing each of CP-E-coil or CP-K-coil individually, or the mixture of each coil construct with wtP22 capsid (Fig. 6.4A). Single spectra of the CP-E-coil and CP-K-coil capsids at 1mg/mL individually, and after mixing are shown in Fog. C.13.

The capacity of the coiled coil interaction between the C-termini of adjacent procapsids to facilitate assembly on a surface, using a layer-by-layer approach, was monitored via quartz crystal microbalance with dissipation (QCM-D). The CP-K-coil (20 μg) was deposited on a gold-coated quartz sensor followed by a buffer wash and equilibration and subsequent addition of CP-E-coil (20 μg) and another buffer equilibration. This process was repeated two more times in the layer-by-layer deposition process (Fig. 6.4B). Each addition of P22 resulted in a decrease in frequency (Δf) indicating deposition of the protein on the crystal surface and was also accompanied by an increase in the dissipation (D) at each step.

Conclusions

Here we have shown that the C-terminal region of the coat protein from the bacteriophage P22 is indeed exposed to the exterior environment of the capsid. From the available cryo-electron microscopy models, the exact location of the C-terminus of the CP is slightly ambiguous. Using genetic manipulation of the C-terminus, including the addition of a single cysteine residue to the C-terminus, incorporation of a 6xHis motif, and genetic fusion of complementary coiled-coil peptides we have established that these modifications to the C-terminus are exposed to the exterior of the capsid. This greatly enhances the ability to use the P22 capsid system as a functional nanomaterial and we have demonstrated this unique site on the capsid can be used for small molecule chemical conjugation, as well as for fabrication of capsid-based extended materials through the directed interparticle interaction mediated by disulfide bond formation and directed coiled-coil interactions.

Materials and Methods

Generation of P22 Structural Images

The cryo EM reconstruction coordinates were obtained from the protein data bank (PDB) entries for the procapsid coat protein (PDB: 2XYY), the expanded shell (virion coat protein, PDB: 2XYZ and P22 expanded head coat protein, PDB: 3IYI), and the wiffleball morphology (PDB: 3IYH). Images were created using UCSF Chimera (version 1.6.2) from the Resource for Biocomputing, Visualization,and Informatics at the University of California, San Francisco(*156*).

Expression Vectors

For expression of wtP22/wtSP particles, the previously described assembler plasmid(*97*) that contains genes corresponding to wt scaffold, wt coat protein, and ampicillin resistance was used. The genes for the novel mCherry capsids presented were generated using a previously described pET $11a^{+}$ template containing mCherrySP141, K118C CP, and ampicillin resistance(*59*). From 5' to 3', the mCherrySP141 DNA sequence in the template vector coded for mCherry fluorescent protein, a thrombin proteolytic site, a cysteine (SP-C140), and SP141-303 all in a single reading frame. Established polymerase chain reaction protocols(*157*) using the C118K, SP-C140A, and CP-431C primers (S1) were followed to change or add codons in the template. The C118K primer changes a previously described CP variant (K118C) back to wtCP, the SP-C140A substitutes an alanine for the cysteine to create mCherrySP141(C140A), and the CP-431C adds a cysteine to the CP C-terminus (CP-431C).

Genes for the CP C-terminal additions were ligated into the Novagen pRSFDuet™-1 (Kan^{R}) vector to allow for expression of P22 virus-like particles. The coat protein (CP) from the Bacteriophage P22 and a truncated form of the P22 scaffold protein SP(141-303), hereafter referred to as SP141, were incorporated into each of the two multiple cloning sites. Initially, the gene corresponding to the SP141 was amplified from the assembler plasmid(*59*) and ligated into the first multiple cloning site BamHI and SacI. Ligation into this location yields a 6xHis tag present in the expression vector reading frame directly upstream of the SP141 gene.

Subsequently, the gene for the CP-6xHis was amplified out of the assembler plasmid(*97*), and was inserted into the second multiple cloning site of this vector using BglII and XhoI. An SpeI site incorporated upstream of the 6xHis sequence to allow for the insertion of K-coil and E-coil sequences at this site. The primer used for the amplification is shown in Table S1. K-coil and E-coil flanked by SpeI and XhoI were purchased in a pUC57-Kan vector from Genscript, isolated and ligated downstream of the coat protein gene. Novagen pRSFDuet™-1 vectors containing a gene for kanamycin resistance, a truncated P22 scaffold protein (6xHis-SP141), and a P22 coat protein (CP-6xHis, CP-K-coil, or CP-E-coil) were transformed into *E.coli* strain XL1 electrocompetent cells (Agilent Technologies). Colonies resulting from each ligation were screened for CP amplification by colony PCR. Isolated plasmids from positive colonies were sequenced (Seqwright, TX) for verification.

Capsid Expression and Purification

Expression vectors for wtP22/wtSP, wtP22/mCherrySP141, wtP22/mCherrySP141(C140A), CP-431C/mCherrySP141(C140A), wtP22/6xHis-SP141, CP-6xHis/6xHis-SP141, CP-E-Coil/6xHis-SP141, and CP-K-Coil/6xHis-SP141 P22 capsids were transformed into electrocompentant *E.coli* strain BL21 (DE3, Novagen). One milliliter from an overnight culture was used to inoculate 1 L of LB supplemented with the appropriate antibiotic (ampicillicin or kanamycin). Cells were grown at 37°C, and induced with 1 mM isopropyl β-D-1-thiogalactopyranoside (IPTG) at an OD_{600} of 0.6. Approximately 4h later, cells were collected by centrifugation and lysed with DNase, lysosyme, and RNase (Sigma Aldrich). Sonication was used to disrupt the cells

(3x for 2.5 min at 50% amplitude, pulse 0.5 sec on/off, Branson Digital Sonifier 250, 200W, 20kHz). Large cellular debris were removed through centrifugation (45 min at 12,000 x g). Subsequently, P22 capsids were pelleted through a 35% sucrose cushion for 50 min at 45,000 x g using ultracentrifugation (Sorval WX Ultra 80, Thermo Scientific). Pellets were resuspended in phosphate buffered saline (10-30 mg/mL, pH 7.6), and dialyzed to remove excess sucrose. Size exclusion chromatography using a Sephacryl-500 column was completed as a final purification step using phosphate buffered saline (pH 7.6). The P22 capsid concentration was determined with the absorbance at 280 nm using an extinction coefficient A280 = $1.4(mg/mL)^{-1}$.

Liquid Chromatography-Mass Spectroscopy (LC-MS)

Masses of the P22 coat proteins prior to and after modification were determined by using a micro-TOF (Bruker Daltonics) mass spectrometer. Aproximately 1.5 micrograms (2-4 µL volume) of each P22 sample in PBS buffer (25 mM phosphate, 50 mM NaCl, pH 7.6, purified as described previously) was injected via an Agilent 1100 series high performance liquid chromatography (HPLC) system equipped with a PolyHydroxyethyl A sizing column (100 x 4.6 mm, 5 µm, 500 Å from PolyLC, Inc.). Samples were continuously flowed to the ESI source from the HPLC using an isocratic elution (25% acetonitrile, 75% water, and 0.1% formic acid) and a flow rate of 0.3 mL-min^{-1}. Source parameters were as follows: drying gas 6.0 L-min^{-1}, nebulizer 3.5 Bar, capillary voltage 3500 V, capillary exit 100 V. Spectra were collected in positive mode from 200 to 3000 m/z at a rate of 2 Hz. The resulting multiple charge state distributions

for protein were deconvoluted using a maximum entropy deconvolution algorithm in the Bruker Compass Analysis software.

Ni-NTA Affinity Chromatography

To test for binding of the capsids with 6xHis tags, approximately 0.5 mg (1 mL vol) of each sample was applied to a 1 mL Ni HisTrap® column (Pharmacia) equilibrated in PBS. Bound capsids were eluted from the column at a flow rate of 0.5 $mLmin^{-1}$ with a buffer gradient containing 0 M to 1 M imidazole in 25 mM HEPES, 100 mM NaCl, pH 7.1. Protein elution was monitored via the absorbance at 280 nm, and fractions containing protein were analyzed by SDS-PAGE.

SDS-PAGE and Western Blot Analysis

Samples were mixed with 4x loading buffer containing DTT and heated in a boiling water bath for 10 minutes prior to loading on tris-glycine gels with a 4% polyacrylamide stacking gel and a 15% polyacrylamide running gel (stock solutions made from: Biorad 30% Acrylamide/Bis Solution 29:1, Ammonium persulfate, TEMED, and TRIS base from Fisher). Gels were run at a constant current of 35 mA for approximately 1 hour. Upon completion, gels were either stained with coomassie and imaged with a UVP MultDoc-IT Digital Imaging System, or proteins were transferred (2 h at 200 mA) to a Hybond C nitrocellulose membrane (Amersham Biosciences) for Western blot analysis. Nitrocellulose membranes were incubated in blocking solution (5% milk powder in tris-buffered saline with 0.01% Tween-20) overnight at 4ºC, followed by incubation with a 1:2,000 dilution of anti-6xHis epitope tagged antibody in

blocking solution for 3 hrs at room temperature. Subsequently, a 1:10,000 dilution of anti-mouse HRPO conjugate in blocking solution was added for 30 min at room temperature. The membrane was washed with TBS, 0.01% Tween 20 prior to each incubation step and an Opti-4CN kit (Biorad) was used for detection.

Enzyme Linked Immunosorbent Assay (ELISA)

A 1:10 dilution of a commercially available mouse anti-6xHis tag antibody was made into a 50 mM Carbonate buffer, pH 9.6. Fifty microliters of this antibody solution was loaded into each well on a coated 96 well ELISA plate (Nunc) and incubated for approximately 2.5 hrs at 37ºC. A PBS control containing no protein and each P22 capsid sample at 0.5 mg/mL were diluted 10 fold into buffer (containing 25 mM phosphate, 50 mM NaCl, 0.05% Tween 20, 2% w/v polyvinylpyrrolidone (MW 40,000), 0.2% w/v bovine serum albumin, and 0.02% sodium azide), 150 µL was added to each well, and the plate was incubated overnight at 4ºC. The plate was subsequently incubated for 3 hrs at room temperature with a rabbit antibody recognizing the P22 coat protein in the same buffer used for the capsid incubation. One hundred microliters of anti-rabbit HRP conjugate (Biorad, 1:3,000 fold dilution in 25 mM phosphate, 50 mM NaCl, 0.05% Tween 20, 2% w/v polyvinylpyrrolidone (Mw 40,000), 0.2% w/v bovine serum albumin) was added to each well and incubated at room temperature for 1 hour. The plate was washed 5x with PBS, 0.05% Tween 20 after each incubation step. The presence of P22 capsids was detected with a OptEIA ELISA TMB Substrate Reagent Set (BD Biosciences), and the relative absorbance at 350 nm was recorded using a Spectra Max Plus 384 plate reader (Molecular Devices) with a SoftMax Pro 5.4.4 software package. A

background absorbance value for the PBS control was subtracted from the each average recorded absorbance to yield the data presented in Figure 2C.

Size Exclusion Chromatography Coupled to Multi-Angle Light Scattering (SEC-MALS)

Separation on a size exclusion column (Wyatt Technologies, WTC-0200S) preceded detection using a Wyatt HELEOS Multi Angle Laser Light Scattering (MALLS) detector, equipped with a quasi-elastic light scattering detector (QELS) and an Optilab rEX differential refractometer (Wyatt Technology Corporation). Twenty five microliters of each capsid at approximately 1.5 mg/mL was injected through the SEC column on an Agilent 1200 HPLC with buffer (50mM phosphate, 100mM NaCl buffer, 3mM sodium azide) at a flow rate of 0.7 mL/min. Astra 5.3.14 software from Wyatt Technology Corporation was used to calculate the number average molecular weight (Mn) from the molecular weight distribution.

Reaction of P22 Cysteines with Fluorescein-5-Maleimide (F5M)

Fluorescein-5-Maleimide (Pierce) was reacted with 2 mg (3.1 $mg^{-}mL^{-1}$) of each: wtP22/mCherrySP141, wtP22/mCherrySP141(C140A), and CP+431C/mCherrySP141(C140A) procapsid. A 20 fold molar excess of F5M per P22 subunit was added dropwise from a stock solution in DMSO, and the reaction was stirred vigerously for 2 hours at room temperature. Pelleting of the procapsids through a sucrose cushion, followed by resuspension and an additional pelleting by ultracentrifugation in PBS buffer removed excess F5M from the samples. Unmodified and labeled samples

were diluted 20x into denaturing buffer (6 M Guanidine HCl, 50mM Phosphate, 100mM NaCl at pH 7.7), mixed, and UV-visible spectra of the denatured protein samples were recorded approximately 10 minutes later. The UV-visible absorbance of a series of F5M concentrations in the denaturing buffer was measured to calculate the extinction coefficient of the F5M in these conditions.

Reaction of P22 Cysteines with N-ethyl Maleimide

N-ethylmaleimide (NEM, Pierce) was reacted with P22 capsids to block inter-capsid disulfide formation. From a stock solution of 50mg/mL NEM dissolved in dimethylformamide(DMF), a fifty fold molar excess of NEM per P22 subunit was added dropwise to 2 mg (0.5 mg mL^{-1}) of each wtP22/mCherrySP141(C140A) and CP+431C/ mCherrySP141(C140A) capsids in PBS pH 7.0. Controls for the labeling experiments were carried out by the addition of a corresponding volume of neat DMF. After stirring rapidly for 3 hours at room temperature, P22 capsids were diluted into pH 7.0 PBS buffer, mixed for 1 hr at 4ºC, and pelleted through a 35% sucrose cushion in the ultracentrifuge (50 min at 45,000 x g) to remove unreacted NEM. Samples were subsequently resuspended and pelleted (50 min at 45,000 x g) a second time in pH 7.3 PBS buffer, and left rocking in PBS pH 7.3 overnight at 4°C. Samples of resuspended protein were analyzed from the supernatant solution after a 5 minute centrifugation step at 17,000 x g. Subsequently, 20 uL of DTT stock solution was added to reduce disulfides, resulting in a final concentration of 5mM DTT, and samples were left to resuspend overnight at 4ºC. Samples of resuspended protein were again analyzed from the supernatant solution after a 5 minute centrifugation step at 17,000 x g.

Quartz Crystal Microbalance with Dissipation (QCM-D)

CP-K-coil and CP-E-Coil capsids were injected onto gold coated quartz crystal (Q-Sense, QSX301) positioned in a Q-Sense D300 (Q-Sense AB) quartz crystal microbalance with dissipation. Additions of 600 µL of each sample (CP-K-coil or CP-E-coil) at a concentration of 3.3 µg/mL in 50 mM phosphate, 100 mM NaCl, pH 7.0 was loaded onto the crystal and let equilibrate for 20 min at 25ºC. A 20 minute buffer equilibration step at 25ºC followed each capsid addition. The frequency and dissipation values were recorded using QSoft 301 software program (version 1.6.16.69) interfaced to the instrument.

APPENDICES

APPENDIX A

SUPPORTING INFORMATION FOR CHAPTER FOUR

Supplementary Methods

Materials

DNA restriction enzymes were purchased from New England BioLabs (Ipswich, MA) and Promega (Madison, WI). DNA primers and sequencing were purchased from Eurofins MWG Operon (Huntsville, AL) and GenScript (Piscataway, NJ). PCR was completed using an Applied Biosystems 2720 Thermal Cycler (Life Technologies, Grand Island, NY) and a MJ Research MiniCycler. BL21(DE3) chemically competent *E. coli* and the pRSFDuet-1 (K^R) plasmid DNA was purchased from EMD Millipore/Novagen (Billerica, MA). Chemically competent XL2-Blue Ultracompetent *E. coli* cells and PfuUltra II Fusion HS DNA Polymerase were purchased from Agilent Technologies (Santa Clara, CA). A BTX™ ECM399 electroporator (Harvard Apparatus, Holliston, MA) was used for electrocompetent cells. The pBAD (A^R) plasmid DNA was purchased from Invitrogen (Carlsbad, CA). QIAquick spin columns and QIAprep Spin Miniprep kit were purchased from Qiagen (Valencia, CA). Wide Range protein ladder, DNAse, and RNAse were purchased from Sigma Aldrich (St. Louis, MO). All other chemical reagents were from Fisher Scientific (Pittsburgh, PA).

Cloning and Molecular Biology

The large subunit of [NiFe]-hydrogenase 1 was amplified using Q5®-High Fidelity polymerase (New England Biolabs) from the genomic DNA of BL21(DE3) *E. coli*. The resulting PCR product was digested with DpnI, purified using a QIAquick spin column (Qiagen), and digested with NcoI and BamHI restriction enzymes (RE). The

restriction fragment was then inserted into the multiple cloning site of pRSFDuet-1 (EMD Millipore) using T4 DNA ligase. The gene for the truncated SP was amplified using PCR from a previous assembler plasmid(*59*), purified, and digested with BamHI and SacI RE. The resulting fragment was ligated into the pRSFDuet-1 (K^R) containing the gene for the large subunit of the hydrogenase. The ligation reaction was transformed into chemically competent XL2-Blue Ultracompetent *E. coli* cells (Agilent Technologies). Plasmid DNA was isolated by QIAprep Spin Miniprep (Qiagen), and sequenced. Plasmid DNA was isolated and sequenced. The CP was amplified using PCR from a previous P22 assembler plasmid(*59*) and ligated into the pBAD/HisA (A^R) (Life Technologies) plasmid. The ligation reaction was transformed into XL2-Blue Ultracompetent *E. coli* cells. Plasmid DNA was isolated and sequenced. The small subunit of [NiFe]-hydrogenase 1 was amplified using PCR from the genomic DNA of BL21(DE3) *E. coli.* The resulting PCR product purified and digested with NdeI and BglII RE. The resulting fragment was ligated into the pRSFDuet-1 (K^R) plasmid containing hyaB-SP. The ligation reaction was electroporated at 1450V (5 ms) into homemade electrocompetent *E. coli* TOP10 using a BTX™ ECM399 electroporator. Plasmid DNA was isolated and sequenced. The DNA with positive sequences was co-transformed into BL21(DE3) *E. coli* cells with the pBAD/HisA (A^R) plasmid containing the CP and expressed. The truncated scaffold protein (SP) was amplified from a previous assembler plasmid(*59*), purified, and digested with BglII and XhoI RE. The resulting fragment was then ligated into the pRSFDuet-1 (K^R) plasmid containing the large (hyaB-SP) and small subunit (hyaA) hydrogenase that had been previously cut with BglII and

XhoI, and purified. The ligation reaction was transformed into chemically competent XL2-Blue Ultracompetent *E. coli* cells. Plasmid DNA was isolated and sequenced. The DNA with positive sequences were co-transformed into BL21(DE3) *E. coli* cells with the pBAD/HisA (A^R) plasmid containing the CP and expressed.

Protein Purification and Characterization

Recombinantly Expressed hyaB-SP, hyaA-SP, and CP. For both P22-Hyd_{opt} and P22-Hyd, cells were harvested by centrifugation at 4,500 rpm for 10 minutes. The cell pellets were stored at -20 °C overnight and then resuspended in 100 mM Trizma base, 100 mM NaCl (pH 8) with lysozyme (15 mg/mL), RNAse (30 mg/mL), and DNAase (20 mg/mL) at room temperature and incubated for 30 minutes. The cell suspension was lysed by sonication and centrifuged at 12,000 rpm for 45 minutes at 4˚C. The supernatant was then loaded onto a 35% (w/v) sucrose cushion and ultracentrifuged at 45,000 rpm for 50 minutes using a FiberLite F50L-9X39 rotor on a Sorvall WX Ultra 80 Series Centrifuge. The resulting pellet was resuspended in 100 mM Trizma base, 100 mM NaCl (pH 8), purified by an isopycnic 1.20-1.40 (g/mL) CsCl density gradient, followed by SEC on a Sephacryl S-500 column using a Biologic DuoFlow FPLC (Bio-Rad, Hercules, CA) running at 0.5 mL/min. Fractions were pooled, concentrated by ultracentrifugation and resuspended in the same buffer.

Recombinantly Expressed 6xHis-hyaA-SP and 6xHis-hyaB-SP. An *E. coli* strain containing the pRSFDuet-1 (K^R) plasmid with the 6xHis-hyaA-SP and 6x-His-hyaB-SP genes was grown in LB medium supplemented with 1 mM ammonium iron (II) sulfate

hexahydrate and 1 mM nickel(II) chloride monohydrate in the presence of ampicillin (50 mg/mL) and kanamyacin (15 mg/mL). The expression of 6xHis-hyaA-SP and 6xHis-hyaB-SP was induced by addition of IPTG to a final concentration of 40 μM once the cells reached early log phase (OD_{600}=0.6). Cultures were grown for 4 hours after addition of IPTG, and cells were then harvested by centrifugation at 4,500 rpm for 10 minutes. The cell pellets were stored at -20 °C overnight. The cell pellets were resuspended in 100 mM Trizma base, 100 mM NaCl (pH 8) supplemented with lysozyme (15 mg/mL), RNase (30 mg/mL) and DNase (20 mg/mL) at room temperature and incubated for 30 minutes. The cell suspension was lysed by sonication, subjected to further centrifugation at 8,000 rpm for 20 minutes, and treated with Pierce™ (Rockford, IL) EDTA-free protease inhibitor mini tablets at the manufacturers' recommended concentration. The supernatant was then loaded onto a 5-mL cOmplete His-tag purification column using a Biologic DuoFlow FPLC (BioRad, Hercules, CA) running at 2.5 mL/min. The column was equilibrated with 100 mM Trizma base, pH 8, 300 mM NaCl (buffer A). The column was washed with 5 column volumes of buffer A and the protein was eluted using a linear gradient with 100 mM Trizma base, 300 mM NaCl, 250 mM imidazole (buffer B). Fractions were collected from a single peak and concentrated using a 0.5 mL Amicon Ultra centrifugal filter with a 3 kDa MWCO.

Recombinantly Expressed hyaB-SP and CP. *E. coli* strains containing both plasmids were grown in iron and nickel supplemented LB medium with ampicillin and kanamycin, as described earlier. The expression of the hyaB-SP was induced by addition of isopropyl β-D-thiogalactopyranoside (IPTG) to a final concentration of 1 μM at

OD_{600}=0.6. Cultures were grown for 4 hours after addition of IPTG, and then the expression of the pBAD /HisA (A^R) vector containing the CP was induced with L-arabinose (0.02%, final) and grown for 2 hours. Cells were harvested by centrifugation at 3,700 rpm for 20 minutes. The cell pellets were stored at -20 °C overnight and then resuspended in 100 mM phosphate, 100 mM NaCl (pH 7) with lysozyme, RNase, and DNase at room temperature and incubated for 30 minutes. The cell suspension was lysed by sonication and centrifuged at 12,000 rpm for 45 minutes at 4˚C. The supernatant was then loaded onto a 35% (w/v) sucrose cushion and ultracentrifuged at 45,000 rpm for 50 minutes using a FiberLite F50L-9X39 rotor on a Sorvall WX Ultra 80 Series Centrifuge. The resulting pellet was resuspended in 50 mM phosphate, 25 mM NaCl (pH 8) and purified by size exclusion chromatography on a Sephacryl S-500 column using an ÄKTA Pharmacia FPLC (GE Healthcare) running at 1 mL/min. The flow rate for the purification was 1 mL/min. Fractions were pooled, concentrated by ultracentrifugation at the conditions stated above and resuspended in the same buffer.

Recombinantly Expressed hyaB-SP, hyaA and CP. Expressed and purified using the methods described for the large subunit-SP fusion (hyaB-SP) and CP.

SEC-MALS/QELS and Refractive Index Detection

Samples were separated over a WTC-200S5 or WTC-100S5 (Wyatt Technologies) size-exclusion column utilizing an Agilent 1200 HPLC to maintain a 0.7 mL/min flow rate in 50 mM sodium phosphate (pH 7.2)100 mM NaCl and 200 ppm sodium azide. Samples (25 μL) were injected onto the column and the total run time was 30 minutes. Samples were detected using a UV detector (Agilent), a Wyatt HELEOS

Multi Angle Laser Light Scattering (MALS) detector, a Wyatt Quasi Elastic Light Scattering detector and Wyatt Optilab rEX differential refractometer (Wyatt Technology Corporation). Using the elution-profile data, the number-averaged molecular mass was calculated using Astra 5.3.14 software (Wyatt Technologies) using a dn/dc for protein of 0.185.

ICP-MS

50-200 µL (2-7 mg/mL) of purified protein (P22-Hyd_{opt}, P22-Hyd, and free hyaA-SP hyaB-SP), and their buffer (100 mM Trizma base, 100 mM NaCl, pH 8) was added to 2.5% v/v nitric acid (Ultrapure, Sigma Aldrich) for a final volume of 5 mL. Iron and nickel analysis was completed with a Perkin Elmer ELAN DRCII ICP-MS with a Microflow PFA-ST concentric nebulizer using a 100 µL/min self-aspiration capillary, cyclonic spray chamber, a quartz touch and platinum sample, and skimmer cones. For the iron analysis, DRC mode was used with ammonia as the reaction gas. Utilizing an EzyFit glass mixing chamber, Germanium (50 ppb) was added as an internal standard and SmartTune (Elan DRC/Plus/II) was used as an external standard (Perkin Elmer, Waltham, MA).

Transmission Electron Microscopy

The samples (4 µL, 0.1 mg/mL protein) were applied to a formvar coated grid for 30 seconds then excess protein was wicked away with a filter paper. Then 4 µL of DDH_2O was added to the grids for 30 seconds, wicked away and the grids were stained for 30 seconds with 4 µL 2% uranyl acetate. Images for P22-Hyd, P22-$Hyd_{hyaB\text{-}SP}$, and P22-$Hyd_{hyaB\text{-}SP\ hyaA}$ were collected on a LEO 912AB transmission electron microscope

and a JEOL JEM 1010 transmission electron microscope was used for P22-Hyd_{opt}, both microscopes were used at an accelerating voltage of 100 kV.

SDS-PAGE

The SEC purified sample was mixed with 4X loading buffer containing DTT, heated in a boiling water bath for 6 minutes, removed, and spun down on a bench top centrifuge. Samples were separated on a gel containing a 5% acrylamide stacking gel and a 12% acrylamide running gel using a constant voltage of 125 volts for approximately 1 hour. Gels were stained with Coomassie blue stain, rinsed with water, and destained using methanol/acetic acid/water mix and imaged using a UVP MultiDoc-IT Digital Imaging System.

Characterization of Free Heterodimer

Recombinantly expressed 6xHis-hyaA-SP 6xHis-hyaB-SP (500 μL, 5 mg/mL) was loaded onto a Superose 12 10/300 GL size-exclusion column at a flow rate of 1 mL/min. The column was equilibrated with 100 mM Trizma base, pH 8, 300 mM NaCl. Fractions were collected and concentrated 0.5 mL Amicon Ultra centrifugal filter with a 3 kDa MWCO. Select fractions were pooled, analyzed by SEC under the same conditions, and concentrated as before. Fractions were subjected to SDS-PAGE (10%), transferred to a nitrocellulose membrane. Followed by Western immunoblotting using antibodies raised against Hyd-1 using Pierce Fast Western Blot Kit, ECL(*158*).

Hydrogenase Activity Assays using Dithionite

The protein sample (0.5 mL, 1-5 mg/mL) in buffer (100 mM Trizma base, 100 mM NaCl pH 8) was combined with 2 mL methyl viologen (50 mM, final) and degassed using vacuum and flushed with argon. Sodium dithionite (500 μL, 500 mM) was added anaerobically to the samples for a total reaction volume of 3 mL. The sample was incubated at 37˚C and hydrogen evolution was measured in the headspace of a crimp top vial using a Shimadzu GC-8A TCD with a 0.61 m x 0.64 cm 40/60 Carboxen 1000 Supelco column using argon as carrier gas. Bulk H_2 gas was used as a standard to quantify the sample H_2 production. The effects of reaction vial headspace were tested by varying this volume from 1.5-33mL using the P22-Hyd_{opt} under the same assay conditions.

Effect of pH on Activity with Methyl Viologen (MV) and Chemical Reductant

The protein solution (0.5 mL, 1-5 mg/mL) in buffer, as described previously(*82*) (citrate, pH 5-6; MOPS, pH7; Trizma Base, pH 8) was combined with 2 mL of methyl viologen (50 mM, final) and degassed using vacuum and flushed with argon. Sodium dithionite (500 μL, 500 mM) in the buffers described was added anaerobically to the samples for a total reaction volume of 3 mL. The sample was assayed as before.

Effects of pH on Activity with MV Reduced by Controlled Potential Coulometry

Controlled potential coulometry of methyl viologen (oxidized) was completed using a BASi CV-50W Voltammetric Analyzer using air tight crimped vials containing a

small stir bar using silver wire for the working and auxillary electrodes and a Ag/AgCl reference electrode. Solutions of methyl viologen (50-250 mM) in buffer (pH 4: 50 mM sodium acetate, 50 mM NaCl; pH 5-6: 50 mM sodium citrate, 50 mM NaCl; pH 6.2-7.0: 50 mM sodium phosphate, 50 mM NaCl; 50 mM Trizma Base, 50 mM NaCl, pH 8) were degassed with vacuum, purged with argon, and reduced with a constant potential (-482 mV vs Ag/AgCl or -275 mV vs SHE). Concentrations of reduced methyl viologen were obtained by directly measuring the total charge (Q), converting the number of electrons to the concentration of reduced methyl viologen while accounting for the minimal hydrogen produced through proton reduction at the electrode and subtracting this value from the total charge. After the controlled reduction of the methyl viologen, the solution was extensively degassed under vacuum and purged with argon to remove residual hydrogen. The previously degassed protein solution was added to the vial under argon, and hydrogen production was measured using gas chromatography as previously described.

Determination of $K_{m,\,app}$ Using MV/DT and MV
Reduced by Controlled Potential Coulometry

The protein solution (0.5 mL, 1-5 mg/mL) in buffer (100 mM Trizma base, 100 mM NaCl pH 8) with 2 mL of methyl viologen (variable from 1.5-50 mM, final) was degassed using vacuum and flushed with argon. Sodium dithionite (500 μL, 500 mM) was added anaerobically to the samples for a total reaction volume of 3 mL. The sample was assayed as previously described. Specific activity (P22-Hyd_{opt}, free hydrogenase) vs. [MV^{2+}] was fit using a standard Michaelis-Menten model.

MV^{2+} (2mL, variable from 5-300 mM) was degassed using vacuum and flushed

with argon. Controlled potential coulometry using a BASi CV-50W Voltammetric Analyzer using air tight crimped vials containing a small stir bar using silver wire for the working and auxillary electrodes and a Ag/AgCl reference electrode was used to reduce MV^{2+} to $MV^{+\bullet}$ at pH 5 (50 mM citrate, 50 mM sodium chloride) through controlled electrolysis (0.2-200C). Concentrations of reduced methyl viologen were obtained by directly measuring total charge (Q), converting the number of electrons to the concentration of reduced methyl viologen (1-240 mM $MV^{+\bullet}$) while accounting for the minimal hydrogen produced at the electrode surface and subtracting this value from the total charge. After the controlled reduction of the methyl viologen, the solution was extensively degassed under vacuum and purged with argon to remove residual hydrogen. Previously degassed protein solution was added to the vial under argon, and hydrogen production was measured using gas chromatography as previously described. In order to estimate an apparent K_m of P22-Hyd_{opt} for $MV^{+\bullet}$ at pH 5 (19.6 mM), specific activity at a range of $MV^{+\bullet}$ concentrations was plotted and fit using a standard Michaelis-Menten model.

Hydrogen Oxidation

Hydrogen oxidation activity of the P22-Hyd_{opt} was tested using methods described previously(*159*) using methyl viologen as a redox indicator. We found a specific activity of 34.5 ± 7 μmol $MV^{+\cdot}$•mg^{-1}•min^{-1}, which corresponds to a turnover of 208 s^{-1}.

Oxygen Exposure With Reactivation

P22-Hyd_{opt} and free hydrogenase (1-5 mg/mL) were exposed to air at 4˚C

overnight, placed under vacuum, purged with argon, reduced with additional dithionite, and assayed for activity (pH 8) using MV/DT described above.

Trypsin Proteolysis

P22-Hyd_{opt} and free hydrogenase (1-5 mg/mL) were treated with immobilized trypsin, TPCK treated (Pierce, Rockford, IL) following the manufacturers recommendations. Protein was assayed for activity (pH 8) using MV/DT described above.

Thermal Treatment

P22-Hyd_{opt} and free hydrogenase (1-5 mg/mL) were placed in a water bath at 60˚C for 30 minutes, briefly centrifuged, and assayed for activity (pH 8) using MV/DT described above.

Number and Concentration of hyaA-SP hyaB-SP Within the P22 Capsid

The number and total concentration of the hyaA-SP hyaB-SP heterodimer was determined by size exclusion chromatography coupled to multiangle light scattering using methods described previously(*61, 62*). The total absorbance (A_{280}) of the P22-Hyd_{Opt} and P22-Hyd was found by diluting samples 30-50X in denaturating buffer (6M Guanidine HCl, 100 mM Trizma Base, 100 mM NaCl, pH 8) and a UV spectrum was measured approximately 5 minutes later using an Agilent 8453 UV-Vis spectrophotometer assuming molar extinction coefficients of ε_{280} = 44,620 M^{-1} cm^{-1} for coat; ε_{280} = 63,390 $M^{-1}cm^{-1}$ for hyaA-SP; ε_{280} = 120,760 $M^{-1}cm^{-1}$ for hyaB-SP (Calculated using Peptide Property Calculator, Center for Biotechnology, Northwestern

University). Identical procedures were followed for: (1) the recombinantly expressed large subunit-scaffold protein fusion (hyaB-SP) and coat protein, and (2) the recombinantly expressed large subunit-scaffold protein fusion (hyaB-SP), small subunit (hyaA), and coat protein.

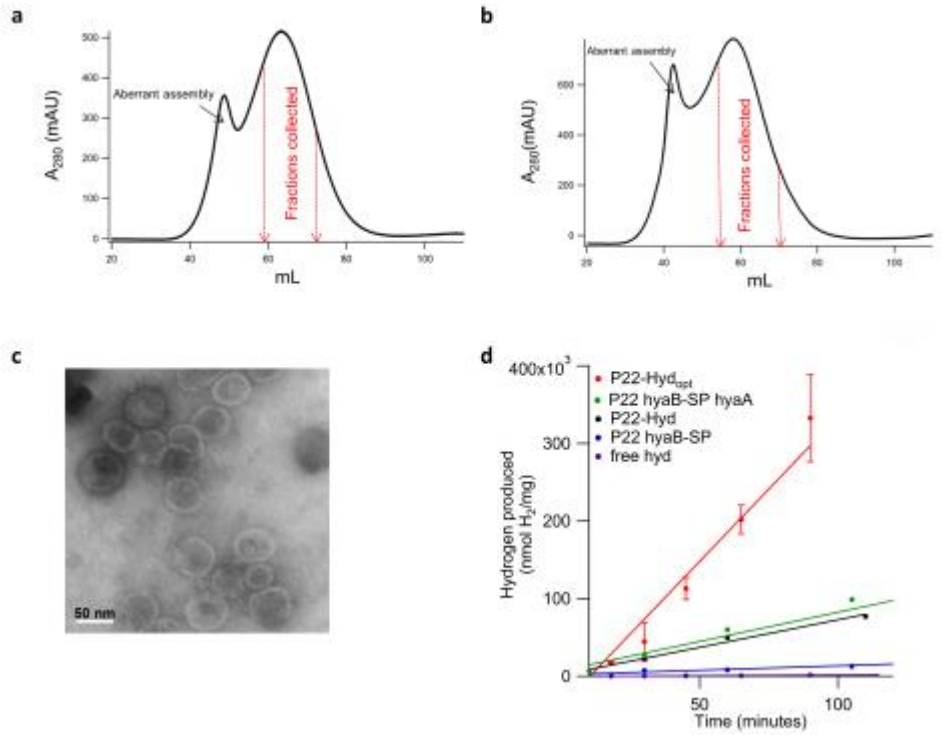

Supplementary Figure A.1 Characterization of Other P22 Hydrogenase Constructs **a,** SEC (Sephacryl S-500) of hyaB-SP encapsulated within the P22 capsid (fractions were isolated as indicated to separate a population of correctly assembled T=7 P22 capsid particles from a population of aberrantly assembled P22 capsids) **b,** SEC (Sephacryl S-500) of hyaB-SP hyaA expressed with in the P22 capsid **c,** TEM (negative stain) of hyaB-SP hyaA expressed in P22 **d,** Specific activity comparison between hydrogenase constructs: P22-Hyd$_{Opt}$ (red circle), P22-hyaB-SP hyaA (green circle), P22-Hyd (black circle), P22-hyaB-SP (blue circle), free hyaA-SP hyaB-SP (purple circle).

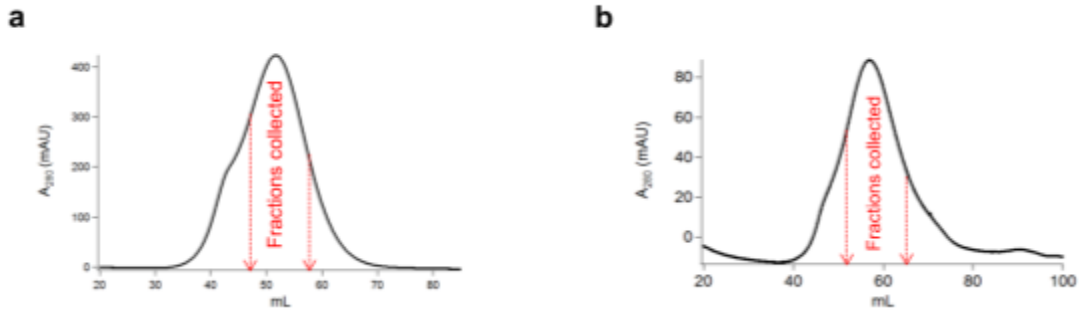

Supplementary Figure A.2. Size-Exclusion Chromatography (SEC) Purification (Sephacryl S-500) of **a,** P22-Hyd$_{Opt}$ and **b,** P22-Hyd

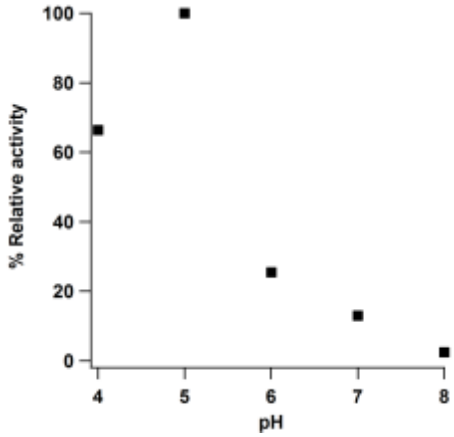

Supplementary Figure A.3. % Relative Activity After Electrochemical Reduction of Methyl Viologen

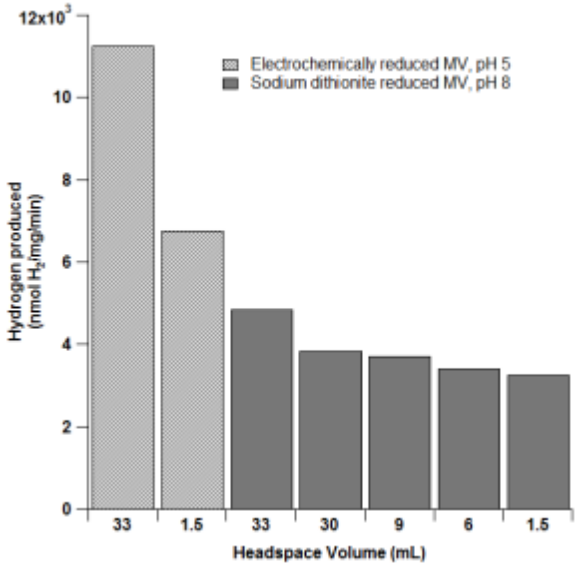

Supplementary Figure A.4. The Effects of Headspace Reaction Vial Volume. The

effects of headspace reaction vial volume on the specific activity of the P22-Hyd_{opt} using dithionite reduced methyl viologen (e- mediator) pH 8 (dark gray) and at pH 5 using electrochemically reduced viologen (light gray).

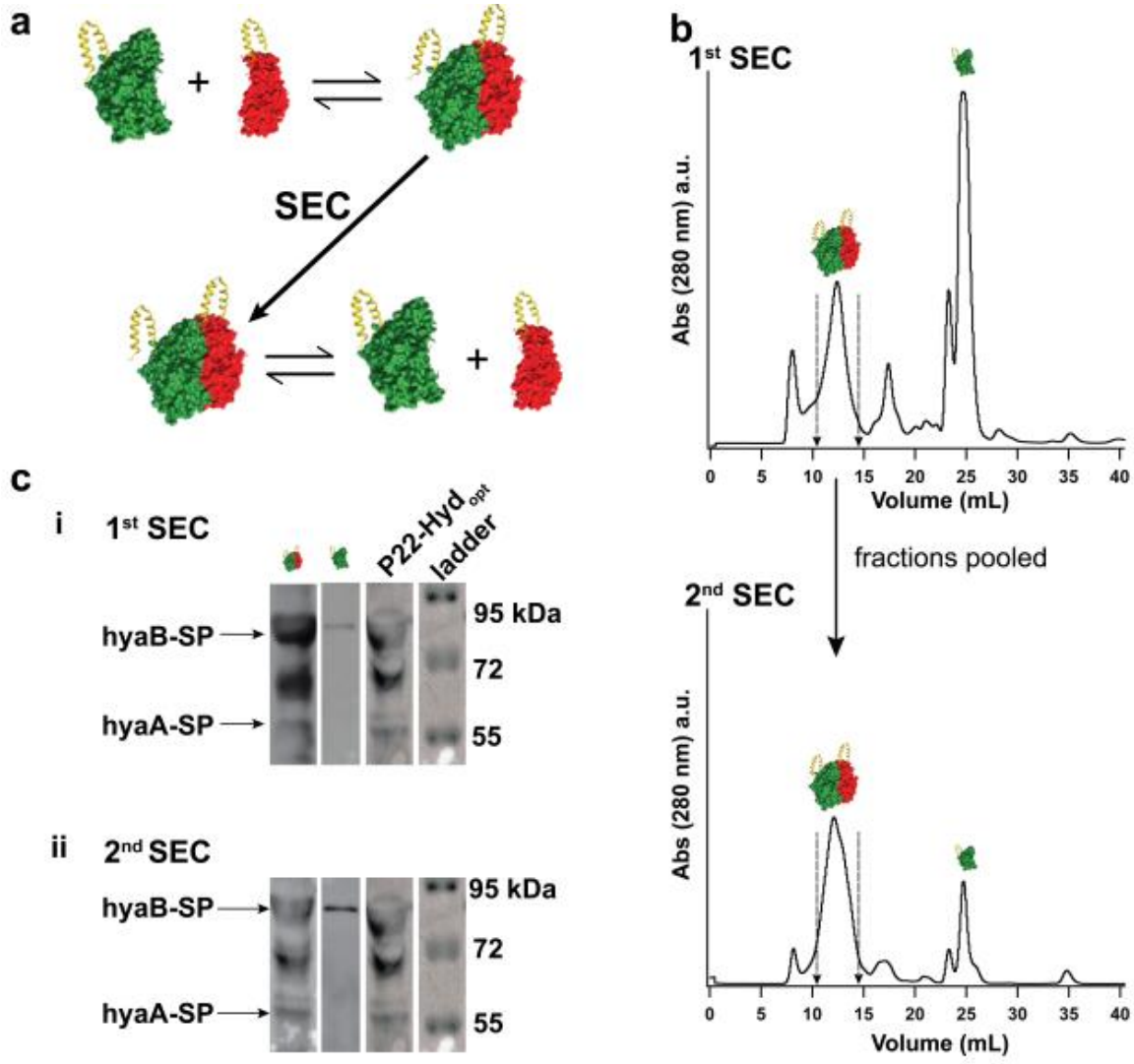

Figure A.5. Characterization of the EcHyd-1 Heterodimer. The small (hyaA-SP) and large (hyaB-SP) subunits of the rEcHyd-1 exist in dynamic equilibrium with the heterodimer. The dynamic equilibrium can be re-established through size-exclusion chromatography (SEC). **a,** The rEcHyd-1 heterodimer (hyaB in green, hyaA in red, SP in yellow) was separated by SEC and subsequently re-establishes the equilibrium between the heterodimer and the monomers. **b**, The free hyaA-SP, hyaB-SP was subjected to SEC, and fractions associated with the heterodimer (hyaA-SP, hyaB-SP) were well separated from the large subunit-scaffold protein (hyaB-SP). Fractions containing the heterodimer

were pooled and a second SEC was performed and an elution profile closely resembling the first SEC was recorded. **c**, Fractions from the two SEC steps were probed in a Western blot, using EcHyd-1 antibodies, and revealed bands corresponding to the heterodimer, and the large subunit-scaffold protein alone,. The P22-Hyd_{opt} was probed using EcHyd-1 antibodies showing bands associated with hyaA-SP and hyaB-SP. The structures are derived from PDB entries 3USE and 2GP8[28,56].

Purification and Characterization of hyaB-SP + CP

The capsids were pelleted using ultracentrifugation and subjected to further purification by SEC (Supplementary Fig. A6) followed by analysis by SDS-PAGE, which showed the presence of both hyaB-SP and CP (Fig. A6a). Subsequent analysis by SEC-MALS/QELS showed an average particle molecular weight of 33.0 MDa corresponding to a packaging of 157 copies of hyaB-SP within the P22 capsid (Fig. A4). The particle size of this material was similar to wild-type capsids (R_{rms} 24.7 ± 0.05 nm; R_h 29.4 ± 0.2 nm; R_{rms}/R_h = 0.84) and TEM showed monodisperse particles with diameters of 58 ± 4 nm (Fig. A1). These capsids, packaged with only the large subunit hydrogenase, were assayed for hydrogenase activity as described previously.

Purification and Characterization of hyaB-SP + hyaA+ CP

Analysis by SEC-MALS/QELS showed an average particle molecular weight of 30.0 MDa (Fig. A1) with particle sizes similar to wild-type and the other P22-Hyd capsids (R_{rms} 25.0 ± 0.06 nm; R_h 29.4 ± 0.2 nm; R_{rms}/R_h = 0.85).

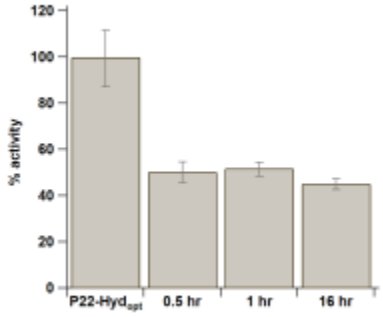

Supplementary Figure A.6. Trypsin Proteolysis of P22-Hyd$_{opt}$. Percent activity remaining after trypsin proteolysis of P22-Hyd$_{opt}$ at 0.5 hr, 1 hr, and 16 hr timepoints.

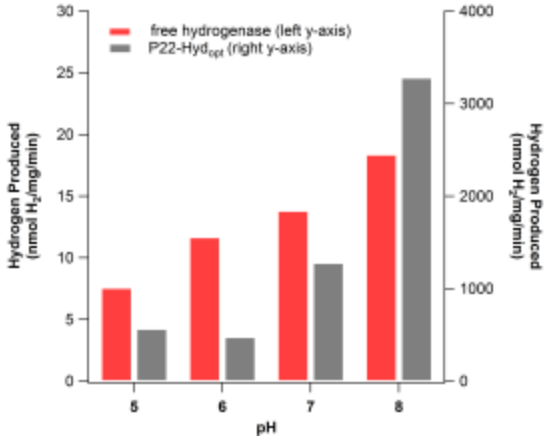

Supplementary Figure A.7. Specific Activity for P22-Hyd$_{opt}$ and Free Hydrogenase for pH 5-8 Using Methyl Viologen (e^- mediatior) and Sodium Dithionite (reductant)

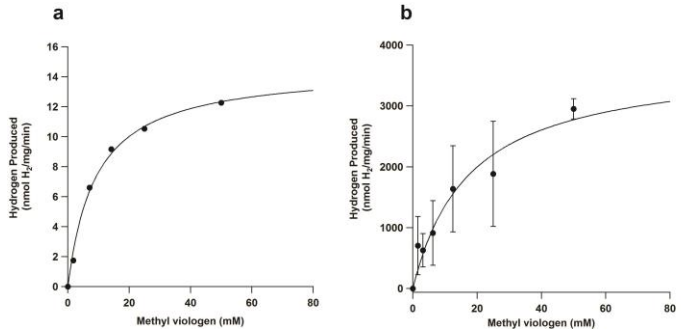

Supplementary Figure A.8. Determination of Apparent K_m for Free Hydrogenase (a) and P22-Hyd$_{opt}$ (b) Using MV/DT at pH 8. We have used pH of the solution and [MV^{2+}] to probe how these conditions in the encapsulated and unencapsulated EcHyd-1 affect activity. We tested the specific activity of the encapsulated hydrogenase in the pH range from 5-8 using dithionite reduced methyl viologen(*82*, *160*). Specific activity was maximal at pH 8, with decreasing activity down to pH 5, for both the free, purified hydrogenase (hyaA-SP, hyaB-SP) and P22-Hyd$_{opt}$ (Fig. A4). We found an apparent K_m for MV^{2+} of 9.1 mM for free hydrogenase and 17.5 mM for P22-Hyd$_{opt}$.

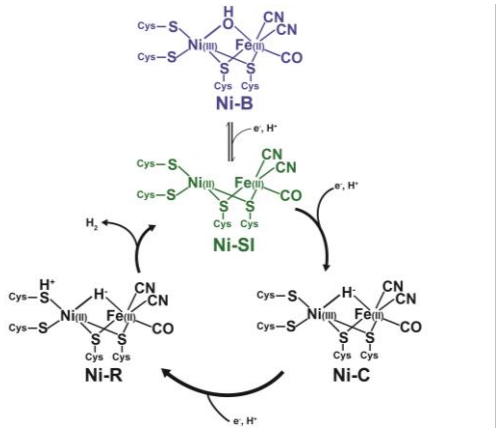

Supplementary Figure A.9. The General Catalytic Cycle for [NiFe] Hydrogenases. (adapted from references (*63*, *68*, *74*)).

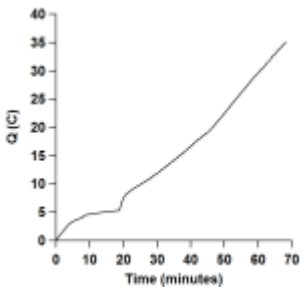

Supplementary Figure A.10. Controlled Potential Coulometry. Controlled Potential

Coulometry (-482 mV vs Ag/AgCl) of oxidized methyl viologen (MV^{2+}) at pH 5 in buffer (50 mM sodium citrate, 50 mM NaCl).

Amino Acid Sequences

P22 Coat Protein in pBAD/HisA (A^R) Plasmid

MALNEGQIVTLAVDEIIETISAITPMAQKAKKYTPPAASMQRSSNTIWMPVEQESP
TQEGWDLTDKATGLLELNVAVNMGEPDNDFFQLRADDLRDETAYRRRIQSAARK
LANNVELCVANMAAEMGSLVITSPDAIGTNTADAWNFVADAEEIMFSRELNRDM
GTSYFFNPQDYKKAGYDLTKRDIFGRIPEEAYRDGTIQRQVAGFDDVLRSPKLPVL
TKSTATGITVSGAQSFKPVAWQLDNDGNKVNVDNRFATVTLSATTGMKRGDKISF
AGVKFLGQMAKNVLAQDATFSVVRVVDGTHVEITPKPVALDDVSLSPEQRAYAN
VNTSLADAMAVNILNVKDARTNVFWADDAIRIVSQPIPANHELFAGMKTTSFSIPD
VGLNGIFATQGDISTLSGLCRIALWYGVNATRPEAIGVGLPGQTA

6xHis-hyaA-SP in pRSFDuet-1 (K^R) Plasmid

MGGSHHHHHHGAGNNEETFYQAMRRQGVTRRSFLKYCSLAATSLGLGAGMAP
KIAWALENKPRIPVVWIHGLECTCCTESFIRSAHPLAKDVILSLISLDYDDTLMAA
AGTQAEEVFEDIITQYNGKYILAVEGNPPLGEQGMFCISSGRPFIEKLKRAAAGAS
AIIAWGTCASWGCVQAARPNPTQATPIDKVITDKPIIKVPGCPPIPDVMSAIITYM
VTFDRLPDVDRMGRPLMFYGQRIHDKCYRRAHFDAGEFVQSWDDDAARKGYC
LYKMGCKGPTTYNACSSTRWNDGVSFPIQSGHGCLGCAENGFWDRGSFYSRVV
DIPQMGTGRSCRSNAVAEQGRKTQEFTQQSAQYVEAARKHYDAAEKLNIPDYQ
EKEDAFMQLVPPAVGADIMRLFPEKSAALMYHLGANPEKARQLLAMDGQSALI
ELTRLSERLTLKPRGKQISSAPPADQPITGDVSAANKDAIRKQMDAAASKGDVET
YRKLKAKLKGIR

6xHis-hyaB-SP in pRSFDuet-1 (K^R) Plasmid

MAHHHHHHMSTQYETQGYTINNAGRRLVVDPITRIEGHMRCEVNINDQNVITNA
VSCGTMFRGLEIILQGRDPRDAWAFVERICGVCTGVHALASVYAIEDAIGIKVPD
NANIIRNIMLATLWCHDHLVHFYQLAGMDWIDVLDALKADPRKTSELAQSLSS
WPKSSPGYFFDVQNRLKKFVEGGQLGIFRNGYWGHPQYKLPPEANLMGFAHYL
EALDFQREIVKIHAVFGGKNPHPNWIVGGMPCAINIDESGAVGAVNMERLNLVQ
SIITRTADFINNVMIPDALAIGQFNKPWSEIGTGLSDKCVLSYGAFPDIANDFGEKS
LLMPGGAVINGDFNNVLPVDLVDPQQVQEFVDHAWYRYPNDQVGRHPFDGITD
PWYNPGDVKGSDTNIQQLNEQERYSWIKAPRWRGNAMEVGPLARTLIAYHKGD
AATVESVDRMMSALNLPLSGIQSTLGRILCRAHEAQWAAGKLQYFFDKLMTNL
KNGNLATASTEKWEPATWPTECRGVGFTEAPRGALGHWAAIRDGKIDLYQCVV
PTTWNASPRDPKGQIGAYEAALMNTKMAIPEQPLEILRTLHSFDPCLACSTHVLG
DDGSELISVQVRGSLVPRGSCRSNAVAEQGRKTQEFTQQSAQYVEAARKHYDA

AEKLNIPDYQEKEDAFMQLVPPAVGADIMRLFPEKSAALMYHLGANPEKARQLL
AMDGQSALIELTRLSERLTLKPRGKQISSAPPADQPITGDVSAANKDAIRKQMDA
AASKGDVETYRKLKAKLKGIR

APPENDIX B

SUPPORTING INFORMATION FOR CHAPTER 5

Supplementary Information

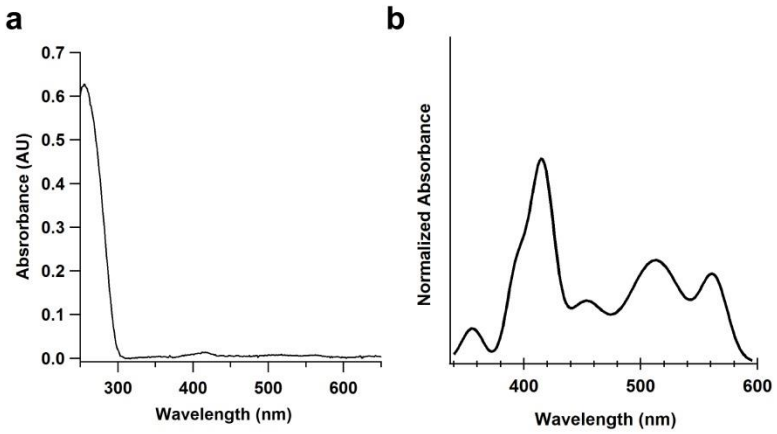

Supplementary Figure B.1. The UV/VIS Spectrum of the P22-Hyd_{cyt}. The full UV/Vis spectrum of the as-isolated P22-Hyd_{cyt} with a baseline corrected and enlarged portion from 340-600 nm showing Soret and Q-bands of the cytochrome b5 heme consistent with literature spectra for similar cyotchromes.

APPENDIX C

SUPPORTING INFORMATION FOR CHAPTER SIX

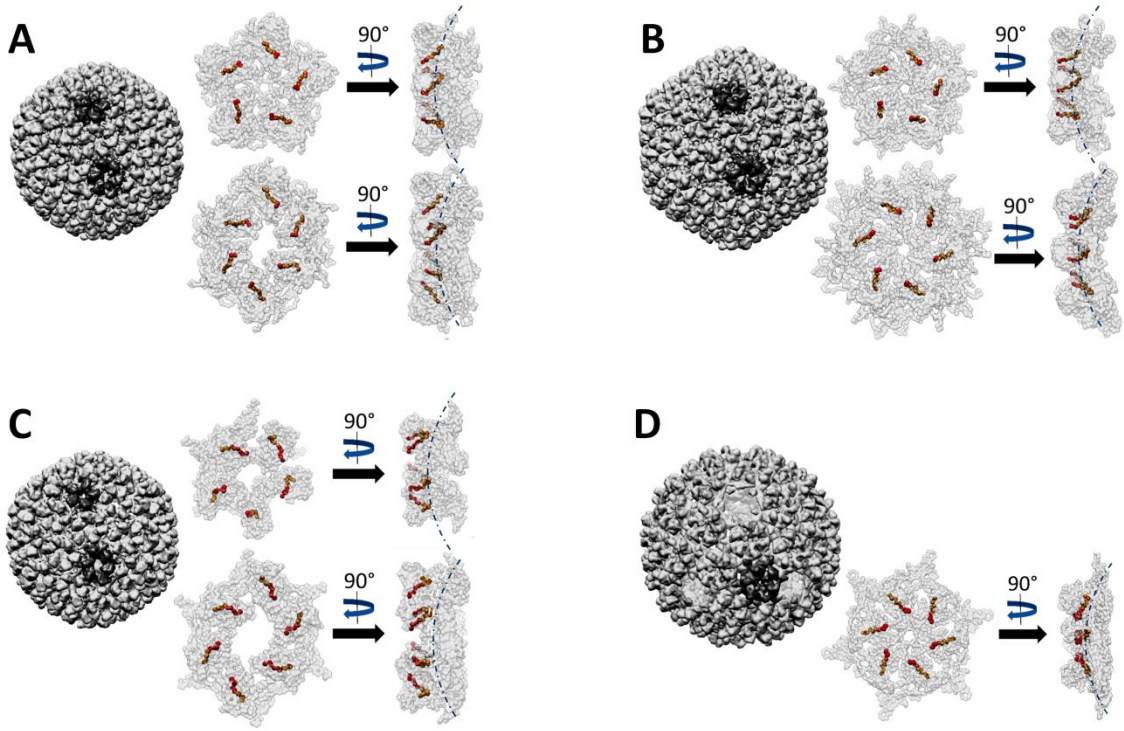

Figure C.1. Images of the *Samonella* Enterobacteria Phage P22 Capsid based upon cryo electron microscopy models published by Chen et al(*145*) and Parent et al(*146*) are shown above. The P22 procapsid coat protein (A: PDB 2XYY as also shown in Figure 1 of the manuscript) can be assembled in vivo from 425 copies of a 430 amino acid coat protein (CP). The P22 procapsid has been previously shown to undergo thermally induced morphological transformations(*144*, *161*) to an expanded morphology (B: PDB 2XYZ for virion coat protein and C: PDB 3IYI for expanded head coat protein) and wiffleball morphology (D: PBD 3IYH). Zoomed versions of the pentamer and hexamer units shaded on the whole capsid are shown as viewed from the capsid exterior.

On the pentamer and hexamer units, the last seven C-terminal residues present each model are highlighted (shaded orange to red). This corresponds to amino acid residues 419-425 for the models published by Chen et al(*145*, *162*) (A and B), and residues 422-428 for the models published by Parent et al(*146*) (C and D). The relative position of residues on the capsid interior (right of dashed line indicating capsid curvature) or exterior (left of dashed line) can be more clearly observed upon rotation of these zoomed images 90°. The CP C-terminus extends toward the capsid exterior in each model. Since the five residues on the C-terminus of the procapsid coat protein structure (A) are not included in the model, we focused the manuscript on probing the location of the procapsid CP C-terminus biochemically. Future experiments will investigate the capcity for exterior display of the CP C-terminus in the other two P22 morphologies. Images were created using UCSF Chimera (version 1.6.2) from the Resource for Biocomputing, Visualization, and Informatics at the University of California, San Francisco(*156*).

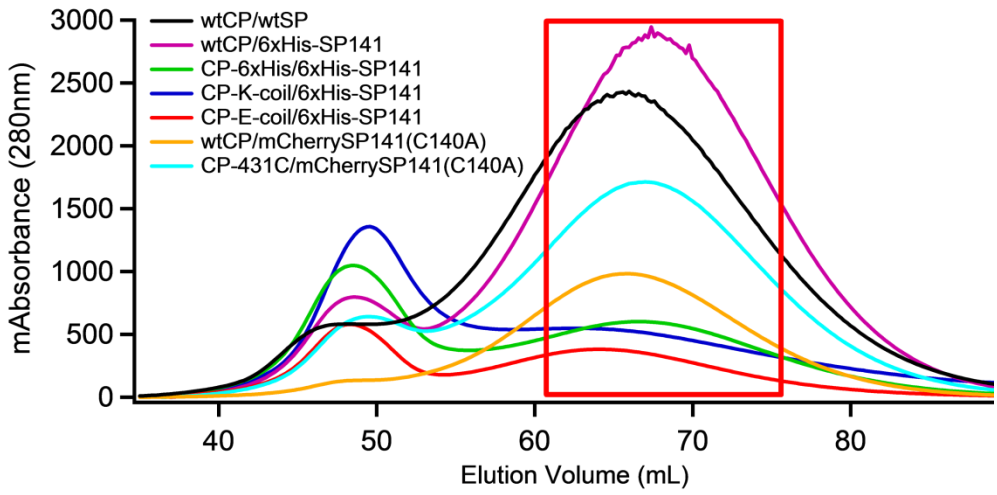

Figure C.2. Size exclusion chromatography (Sephacryl 500 column) was used as the final purification step for the P22 procapsids. The elution fractions from the peak at 65mL (red box), corresponding to the assembled P22 procapsids, were collected and pooled for each sample. The elution peak at observed at approximately 48 mL in the purifications typically corresponds to aberrant assemblies of the P22 coat protein(*163*), and was therefore discarded.

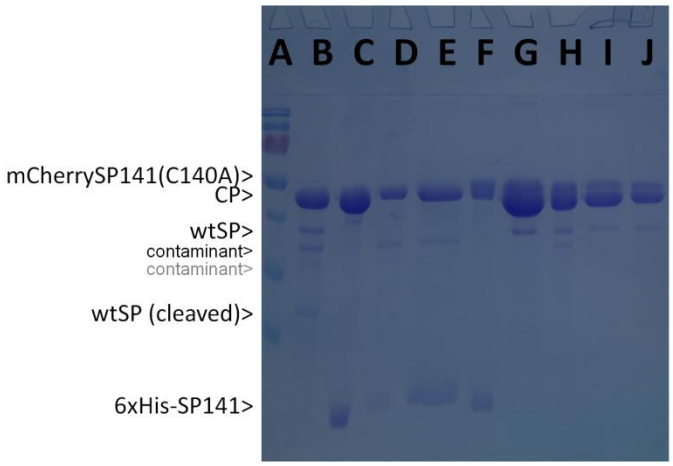

Figure C.3. SDS-PAGE analysis of purified P22 constructs. An E.col protein, OmpF, has been previously documented to co-purify with our P22 capsids(*164*). A) Molecular

Weight Marker, B) wtCP/wtSP, C) wtcP/6xHis-SP141, D) CP-6xHis/6xHis-SP141, E) CP-K-coil/6xHis-SP141, F) CP-E-coil/6xHis-SP141, G) wtCP/mCherrySP141(C140A), H) CP-431C/mCherrySP141(C140A), I) wtCP/mCherrySP141(C140A) + NEM, and J) CP-431C/mCherrySP141(C140A) + NEM.

Letter of Chromatogram	P22 Construct	Mass (MDa)	RMS Radius (nm)	Hydrodynamic Radius (nm)
A	wtCP/wtSP	22.35 ± 0.54	26.0 ± 0.8	28.6 ± 1.0
B	wtCP/6xHis-SP141	27.72 ± 0.07	24.2 ± 0.7	28.0 ± 1.7
C	CP-6xHis/6xHis-SP141	27.85 ± 0.38	27.7 ± 0.7	31.5 ± 1.0
D	CP-K-coil/6xHis-SP141	29.54 ± 0.32	29.1 ± 0.7	32.2 ± 1.0
E	CP-E-coil/6xHis-SP141	29.20 ± 0.17	24.1 ± 0.8	30.0 ± 1.0
F	wtCP/mCherrySP141(C140A)	26.35 ± 0.26	24.2 ± 0.8	27.7 ± 2.0
G	CP-431C/mCherrySP141(C140A)	29.92 ± 0.07	23.7 ± 0.9	28.4 ± 1.0
H	wtCP/mCherrySP141(C140A) + NEM	26.40 ± 0.07	24.2 ± 1.0	26.5 ± 2.0
I	CP-431C/mCherrySP141(C140A) + NEM	29.63 ± 0.27	23.8 ± 1.0	26.6 ± 2.0

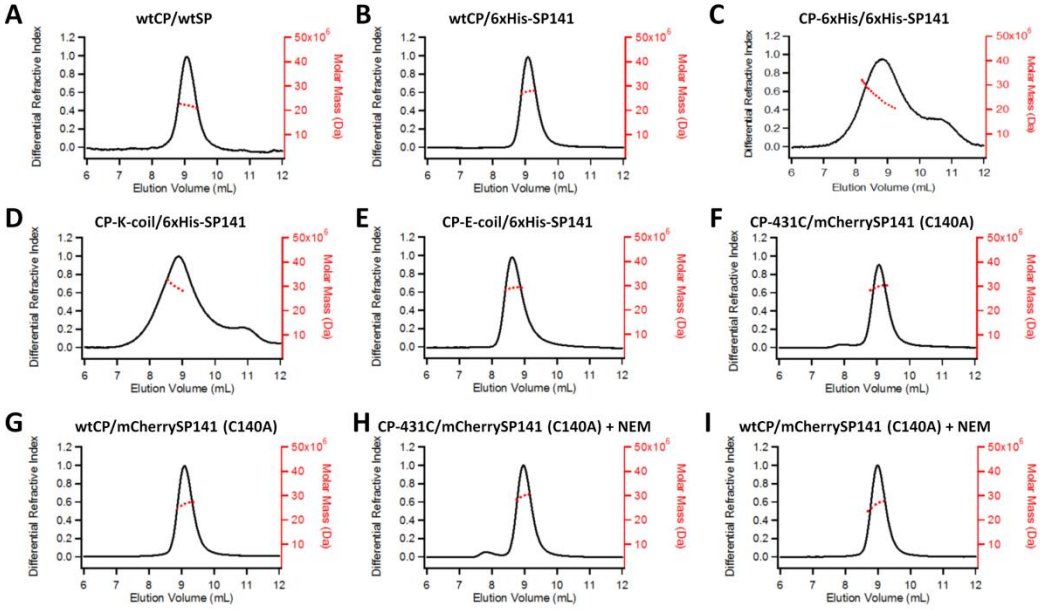

Figure C.4. Size exclusion chromatography coupled to multi-angle light scattering and quasi elastic light scattering. Data on each novel P22 procapsid construct indicates the presence of monodisperse, intact capsids with similar dimensions and molecular weight to wtP22. The wtCP/mCherrySP141(C140A) and CP-431C/mCherrySP141(C140A) constructs are shown prior and subsequent to reaction with N-ethylmaleimide (NEM).

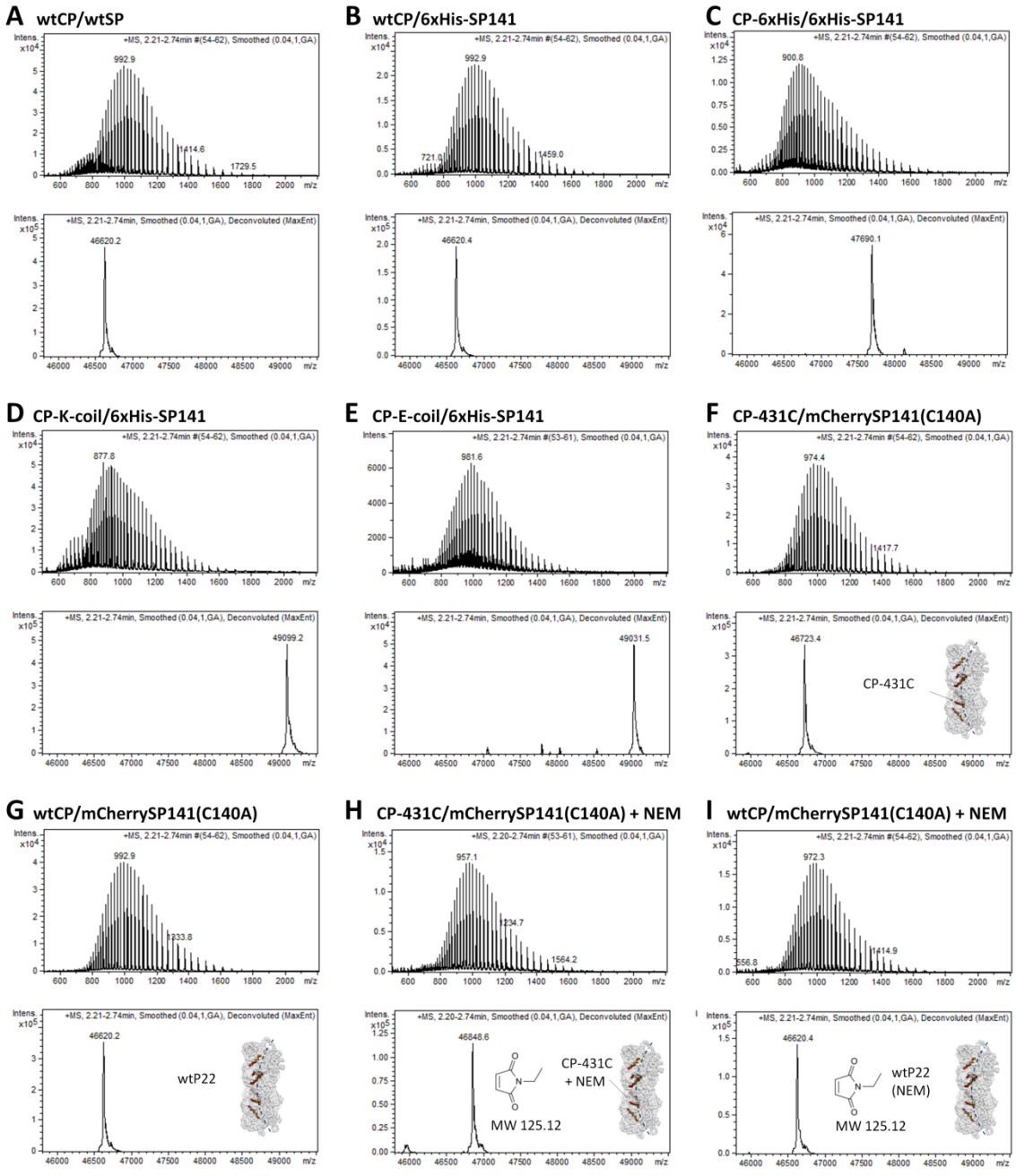

Figure C.5. Liquid Chromatography-Mass Spectroscopy (LC-MS) data from each purified P22 constructs, including wtCPmCherrySP141(C140A) and CP-431C/mCherrySP141(C140A) after reaction with N-ethymaleimide (NEM). The raw m/z data as well as each deconvoluted spectrum is shown.

Letter of Spectrum	P22 Construct (Coat Protein/Scaffold Protein)	CP Expected Mass (Da)	CP Observed Mass (Da)
A	wtCP/wtSP	46621	46620
B	wtCP/6xHis-SP141	46621	46620
C	CP-6xHis/6xHis-SP141	47689	47690
D	CP-K-coil/6xHis-SP141	49098	49099
E	CP-E-coil/6xHis-SP141	49031	49032
F	wtCP/mCherrySP141 (C140A)	46621	46620
G	CP-431C/mCherrySP141 (C140A)	46724	46723
H	wtCP/mCherrySP141 (C140A) + NEM	46746*	46620 (no label)
I	CP-431C/mCherrySP141 (C140A) + NEM	46849*	46849

* indicates expected CP mass when labeled with N-ethyl maleimide (NEM)

Figure C6. Summary of the Liquid Chromatography-Mass Spectroscopy (LC-MS) Mass spectroscopy data shown in Figure S5. The mass measured for each P22 coat protein (CP) on the ESI-TOF instrument matches the mass of the coat protein as calculated from the expected amino acid sequence for each purified or N-ethylmaleimide (NEM) labeled construct.

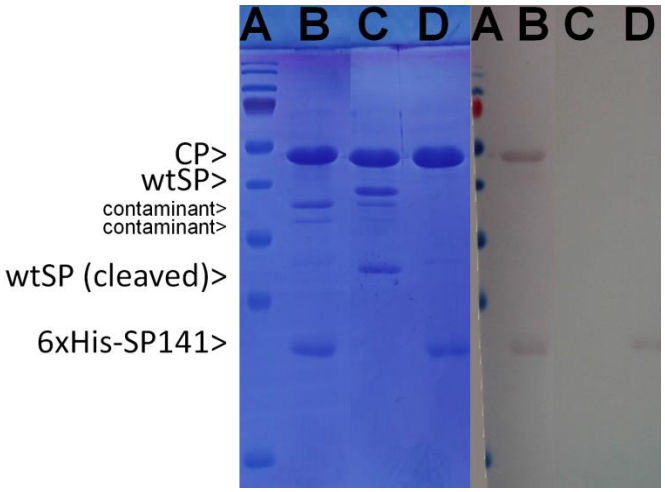

Figure C.7. SDS-PAGE gel (left) and Western blot analysis (right) of the following: A) Molecular weight standard, B) CP-6xHis/6xHis-SP141, C) wtCP/wtSP, and D) wtCP/6xHis-SP141. The right panel shows a western blot of the same samples with detection for the 6xHis epitope.

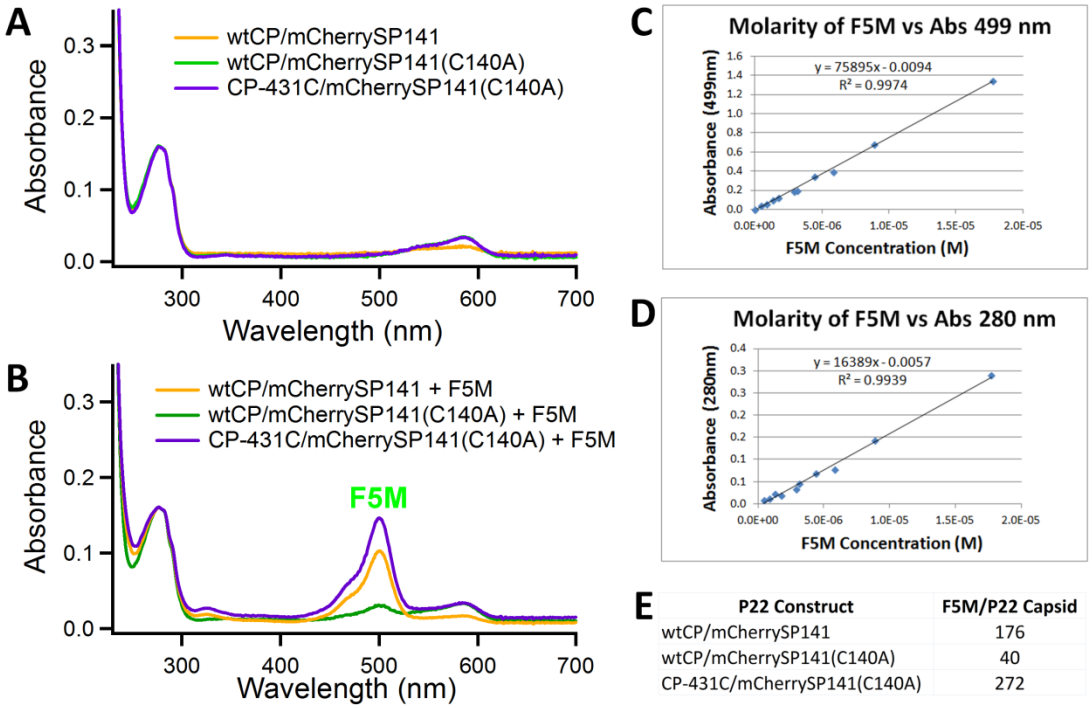

P22 Construct	F5M/P22 Capsid
wtCP/mCherrySP141	176
wtCP/mCherrySP141(C140A)	40
CP-431C/mCherrySP141(C140A)	272

Figure C.8. UV-visible spectra of wtCP/mCherrySP141, wtCP/mCherrySP141(C140A), and CP-431C/mCherrySP141(C140A) A) unmodified P22 procapsids prior to flourescein-5-maleimide (F5M) labeling and B) capsids after labeling with F5M. Spectra were measured in a denaturing solution of 6M Guanidine HCl, 50mM Phosphate, 100mM NaCl @ pH 7.7. The UV-visible absorbance spectra of F5M solutions at a series of concentrations were recorded and the absorbance values at 499 nm (C) and 280 nm (D) were plotted vs concentration to calculate the F5M extinction coefficients for F5M under these conditions. The extinction coefficients for F5M (shown as the slope of the line) were utilized in combination with the recorded absorbance values of P22 capsid (Ex 280, 0.98) to calculate the number of F5M/P22 capsid as shown in the table (E).

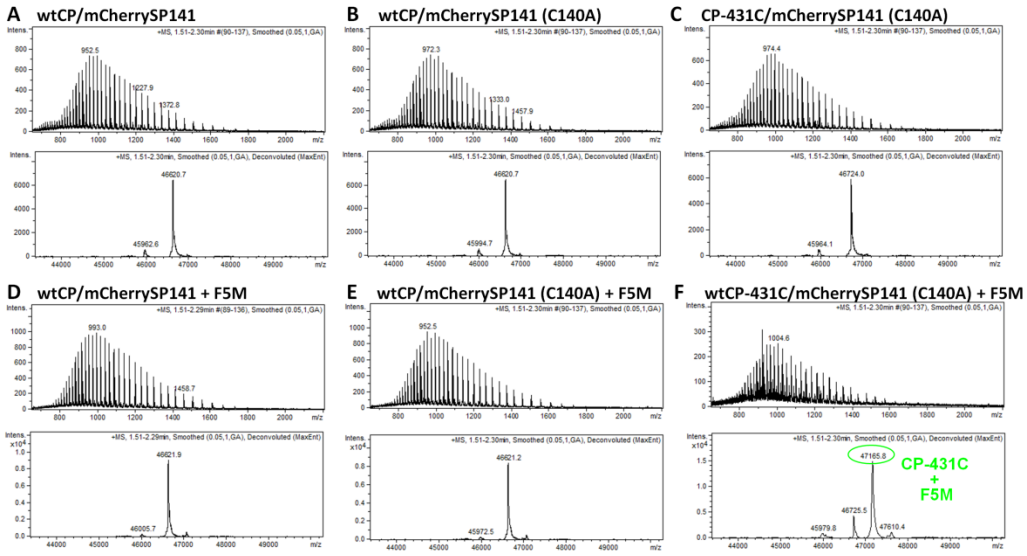

Figure C.9. Liquid Chromatography-Mass Spectroscopy (LC-MS) Mass spectroscopy data showing the CP subunit mass from each mCherry construct prior to labeling with Flourescein-5-Maleimide(F5M, A-C) and subsequent to labeling with F5M (D-F). The raw m/z data as well as each deconvoluted spectrum are shown. The expected addition of 427 Da, corresponding to F5M labeling of the CP, is observed by mass spectroscopy on the CP-431C/mCherrySP141(C140A), but not on the wtCP/ mCherrySP141 or wtCPmCherrySP141(C140A) coat proteins.

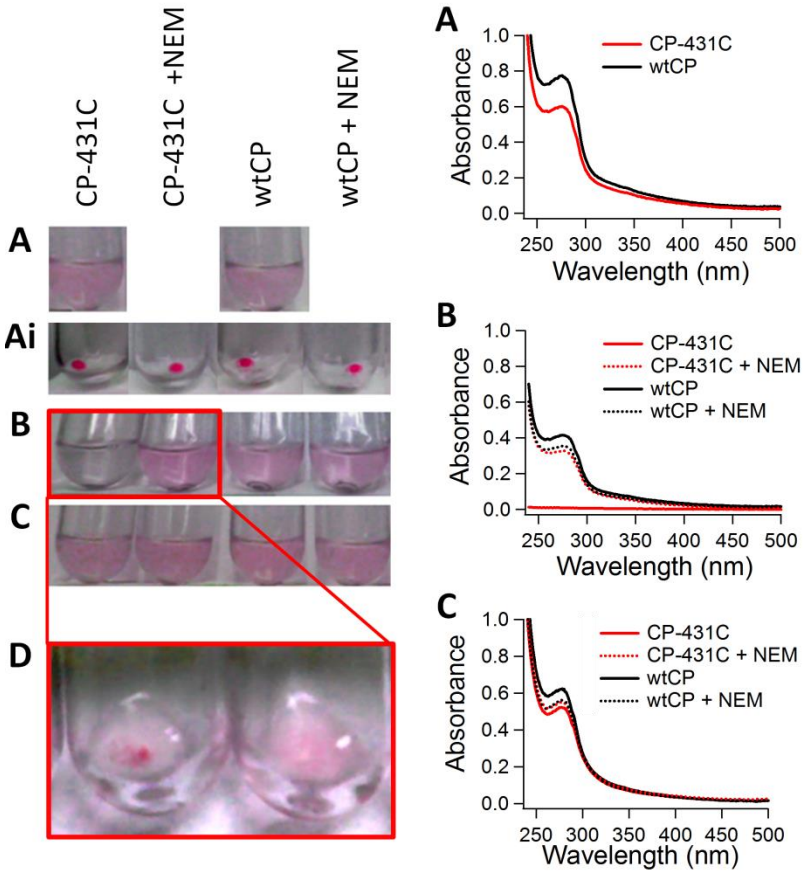

Figure C.10. Pictures of wtCP/mCherrySP141(C140A) and CP-431C/mCherrySP141(C140A): A) prior to labeling with N-ethylmaleimide (NEM), Ai) after pelleting of both NEM labeled and unmodified constructs, B) after resuspension in PBS, and C) after resuspension in PBS with 5mM DTT. Image D shows a close up image of the insoluble pink particulate observed in the CP-431C/ mCherrySP141(C140A) sample upon resuspension in PBS. The yield of resupended protein at each step was quantified by UV-visible spectroscopy. When resuspended in PBS (B), approximately 54% of wtCP/ mCherrySP141(C140A) and 46% of CP-431C/ mCherrySP141(C140A) +NEM were recovered. In contrast, only 2% recovery was observed for the unmodified CP-431C/mCherrySP141(C140A) construct (B). Upon addition of dithioltheatol (DTT, 5mM), 88% of the CP-431C/mCherrySP141(C140A) was recovered, compared to 82%

of the wtCP/ mCherrySP141(C140A) capsid, and 91% of the CP-431C/ mCherrySP141(C140A) + NEM(C).

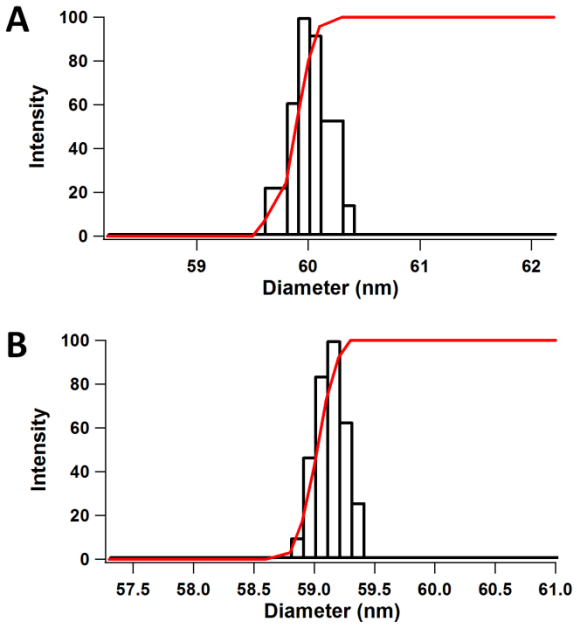

Figure C11. Representative dynamic light scattering data resuspended A) wtCP/mCherrySP141(C140A), and B) CP-431C/mCherrySP141(C140A) after addition of DTT to 5 mM. In both cases, the calucated particle diameter is ~60 nm, indicative of assembled P22 procapsids.

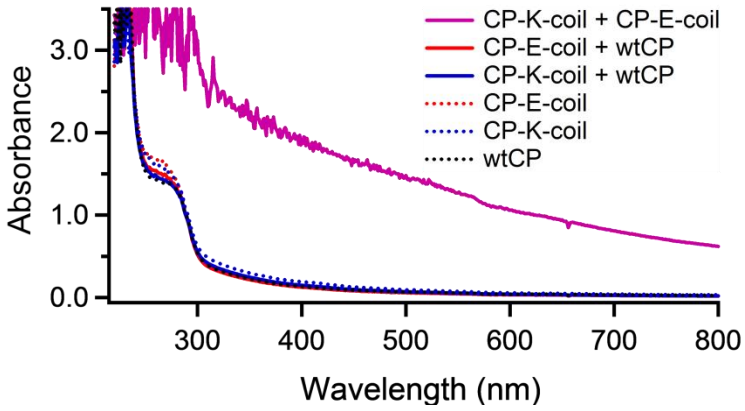

Figure C12. UV-visible spectra of the CP-E-coil/6xHis-SP141 and CP-K-coil/6xHis-SP141 capsids mixed at 1mg/mL, showing a dramatic increase in scattering when compared with each sample individually or when mixed with capsid with wtCP/6xHis-SP141.

APPENDIX D

ADDITIONAL SUPPORTING INFORMATION

Cloning, Expression, and Activity of
hyaB-SP, hyaA-SP, hyaCDEF, and P22 CP

EcHyd-1 is encoded by a six gene operon, *hyaABCDEF*. hyaA and hyaB encode for the small and large subunits, respectively, which form a heterodimer. The remaining genes (*hyaCDEF*) mature and aid in the loading of the core enzyme subunits when basally expressed in BL21(DE3) *E. coli*. We have shown the fusion of each core subunit to a P22 scaffold protein (hyaA-SP, hyaB-SP) using molecular biology in a single plasmid in two multiple cloning sites. Previous experiments showed importance of maturing the core enzyme subunits found in the *E. coli* expression host prior to the expression of the P22 coat protein. The absence of the maturation step results in lower activity.

In order to understand if recombinant overexpression of the remaining maturation proteins would result in increased activity, *hyaCDEF* were amplified from the genomic DNA of BL21(DE3) *E. coli* using PCR and cloned as a NcoI/XhoI fragment into the pACYC plasmid. The pACYC plasmid is chloramphenicol resistant and under the control of IPTG. The hypothesis was that upon induction with IPTG there would be recombinant overexpression of the core enzyme subunits (hyaA-SP; hyaB-SP) and overexpression of hyaCDEF prior to expression of the P22 coat protein and the resultant packaging within the P22 capsid.

The pACYC plasmid containing *hyaCDEF* was transformed into BL21(DE3) *E. coli* and induced with IPTG (40 μM, final) in a 1 mL culture. The total cell lysate was subjected to analysis by SDS-PAGE, stained with coomassie, and destained to reveal bands corresponding to the expected molecular weights of hyaC, hyaD, hyaE, and hyaF.

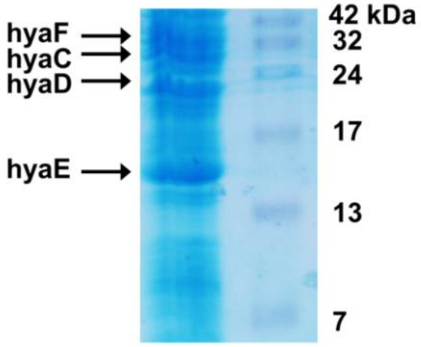

Figure D1. SDS-PAGE analysis of the gene products of *hyaCDEF*. The pACYC plasmid containing the genes encoding for hyaCDEF was induced with IPTG and the total cell lysate was analyzed for expression using SDS-PAGE. The resultant bands corresponding to the expected molecular weights of the proteins: hyaC (27.6 kDa), hyaD (21.5 kDa), hyaE (14.9 kDa), hyaF (31.5 kDa).

Three plasmids (pRSF containing the genes encoding for hyaA-SP, hyaB-SP; pACYC containing the genes encoding for hyaCDEF; and pBad containing the genes encoding for the P22 coat protein (CP)) were co-transformed into BL21(DE3) *E. coli*. As a control two plasmids (pRSF containing the genes encoding for hyaA-SP, hyaB-SP; and pBad containing the genes for the CP) were co-transformed into BL21(DE3) *E. coli*. A colony was picked and deposited into 1 mL of LB growth with appropriate antibiotics and grown overnight at 37˚C with shaking. 40μL of overnight growth was diluted into 4 mL of LB supplemented with 1 mM (final) nickel chloride monohydrate and 1 mM (final) ammonium iron(II) sulfate hexahydrate. The cultures was grown to OD_{600} = 0.6 and then induced with IPTG (40 μM, final). The cultures were grown 1, 2, 4, or 12 hours prior to induction with L-arabinose (20% w/v) for 1 hour. After induction, the 1 mL cultures were spun down at max speed on the bench top centrifuge and resuspended in buffer (100 mM Trizma Base, 100 mM NaCl, pH 8). The cell lysates were assayed for

activity using methyl viologen and dithionite, as described previously. The activity of the 3 plasmid expression was nearly 5x less active in all growth time conditions than the 2 plasmid hydrogenase expression, and therefore there was no clear reason to pursue the 3 plasmid expression.

REFERENCES CITED

1. T. O. Yeates, C. S. Crowley, S. Tanaka, Bacterial microcompartment organelles: protein shell structure and evolution. *Annu. Rev. Biophys.* **39**, 185-205 (2010).

2. C. M. Agapakis, P. M. Boyle, P. A. Silver, Natural strategies for the spatial optimization of metabolism in synthetic biology. *Nat. Chem. Biol.* **8**, 527-535 (2012).

3. D. C. Ducat, G. Sachdeva, P. A. Silver, Rewiring hydrogenase-dependent redox circuits in cyanobacteria. *Proceedings of the National Academy of Sciences* **108**, 3941-3946 (2011).

4. S. Tanaka, M. R. Sawaya, T. O. Yeates, Structure and mechanisms of a protein-based organelle in *Escherichia coli*. *Science* **327**, 81-84 (2010).

5. S. Tanaka *et al.*, Atomic-level models of the bacterial carboxysome shell. *Science* **319**, 1083-1086 (2008).

6. C. A. Kerfeld *et al.*, Protein structures forming the shell of primitive bacterial organelles. *Science* **309**, 936-938 (2005).

7. A. Chessher, R. Breitling, E. Takano, Bacterial microcompartments: biomaterials for synthetic biology-based compartmentalization strategies. *ACS Biomaterials Science & Engineering* **1**, 345-351 (2015).

8. C. Chowdhury, S. Sinha, S. Chun, T. O. Yeates, T. A. Bobik, Diverse bacterial microcompartment organelles. *Microbiol. Mol. Biol. Re.v* **78**, 438-468 (2014).

9. E. Gantt, S. F. Conti, Ultrastructure of blue-green algae. *Journal of Bacteriology* **97**, 1486-1493 (1969).

10. E. I. Tocheva *et al.*, Structure and expression of propanediol utilization microcompartments in *Acetonema longum*. *Journal of Bacteriology* **196**, 1651-1658 (2014).

11. Jeffrey C. Cameron, Steven C. Wilson, Susan L. Bernstein, Cheryl A. Kerfeld, Biogenesis of a bacterial organelle: the carboxysome assembly pathway. *Cell* **155**, 1131-1140 (2013).

12. J. B. Parsons *et al.*, Biochemical and structural insights into bacterial organelle form and biogenesis. *Journal of Biological Chemistry* **283**, 14366-14375 (2008).

13. M. Sutter *et al.*, Structural basis of enzyme encapsulation into a bacterial nanocompartment. *Nat Struct Mol Biol* **15**, 939-947 (2008).

14. S. Kang, T. Douglas, Some enzymes just need a space of their own. *Science* **327**, 42-43 (2010).

15. G. J. Bedwell *et al.*, Selective biotemplated synthesis of TiO_2 inside a protein cage. *Biomacromolecules* **16**, 214-218 (2015).

16. M. Uchida, S. Qazi, E. Edwards, T. Douglas, in *Protein Cages: Methods and Protocols*, B. P. Orner, Ed. (2015), vol. 1252, pp. 17-25.

17. R. J. Usselman *et al.*, Gadolinium-Loaded Viral Capsids as magnetic resonance imaging contrast agents. *Applied Magnetic Resonance* **46**, 349-355 (2015).

18. T. Douglas, M. Uchida, P. E. Prevelige, C. Reichhardt, Virus particles as templates for mineral nanoparticle synthesis. *Abstracts of Papers of the American Chemical Society* **247**, (2014).

19. S. Qazi *et al.*, Manganese(III) porphyrins complexed with P22 virus-like particles as T-1-enhanced contrast agents for magnetic resonance imaging. *Journal of Biological Inorganic Chemistry* **19**, 237-246 (2014).

20. S. Qazi, J. Lucon, M. Uchida, T. Douglas, Protein cage nanoparticles for hybrid inorganic-organic materials. *Coordination Chemistry in Protein Cages: Principles, Design, and Applications*, 275-304 (2013).

21. A. Servid, P. Jordan, A. O'Neil, P. Prevelige, T. Douglas, Location of the bacteriophage P22 coat protein C-terminus provides opportunities for the design of capsid-based materials. *Biomacromolecules* **14**, 2989-2995 (2013).

22. M. Uchida *et al.*, Site-directed coordination chemistry with P22 virus-like particles. *Langmuir* **28**, 1998-2006 (2012).

23. Y. J. Kang, M. Uchida, H.-H. Shin, T. Douglas, S. Kang, Biomimetic FePt nanoparticle synthesis within *Pyrococcus furiosus* ferritins and their layer-by-layer formation. *Soft Matter* **7**, 11078 (2011).

24. C. Reichhardt *et al.*, Templated assembly of organic-inorganic materials using the core shell structure of the P22 bacteriophage. *Chem Commun (Camb)* **47**, 6326-6328 (2011).

25. J. Lucon *et al.*, A click chemistry based coordination polymer inside small heat shock protein. *Chemical Communications* **46**, 264-266 (2010).

26. M. T. Klem, M. Young, T. Douglas, Biomimetic synthesis of β-TiO_2 inside a viral capsid. *Journal of Materials Chemistry* **18**, 3821 (2008).

27. M. T. Klem, J. Mosolf, M. Young, T. Douglas, Photochemical mineralization of europium, titanium, and iron oxyhydroxide nanoparticles in the ferritin protein cage. *Inorganic Chemistry* **47**, 2237-2239 (2008).

28. D. Ensign, M. Young, T. Douglas, Photocatalytic synthesis of copper colloids from Cu(II) by the ferrihydrite core of ferritin. *Inorganic Chemistry* **43**, 3441-3446 (2004).

29. H. A. Hosein, D. R. Strongin, M. Allen, T. Douglas, Iron and Cobalt oxide and metallic nanoparticles prepared from ferritin. *Langmuir* **20**, 10283-10287 (2004).

30. M. Allen, D. Willits, M. Young, T. Douglas, Constrained synthesis of cobalt oxide nanomaterials in the 12-subunit protein cage from *Listeria innocua*. *Inorganic Chemistry* **42**, 6300-6305 (2003).

31. T. Douglas, M. Young, Host-guest encapsulation of materials by assembled virus protein cages. *Nature* **393**, 152-155 (1998).

32. R. Kim, K. K. Kim, H. Yokota, S. H. Kim, Small heat shock protein of Methanococcus jannaschii, a hyperthermophile. *Proc. Natl. Acad. Sci. U S A* **95**, 9129-9133 (1998).

33. Z. Varpness, J. W. Peters, M. Young, T. Douglas, Biomimetic Synthesis of a H_2 catalyst using a protein cage architecture. *Nano Letters* **5**, 2306-2309 (2005).

34. S. Kang *et al.*, Monitoring biomimetic platinum nanocluster formation using mass spectrometry and cluster-dependent H_2 production. *Angew. Chem. Int. Ed. Engl.* **47**, 7845-7848 (2008).

35. L. O. Liepold *et al.*, Structural transitions in cowpea chlorotic mottle virus (CCMV). *Phys. Biol.* **2**, S166-172 (2005).

36. M. Comellas-Aragones *et al.*, A virus-based single-enzyme nanoreactor. *Nat Nanotechnol* **2**, 635-639 (2007).

37. I. J. Minten *et al.*, Catalytic capsids: the art of confinement. *Chemical Science* **2**, 358-362 (2011).

38. I. J. Minten, L. J. A. Hendriks, R. J. M. Nolte, J. J. L. M. Cornelissen, Controlled encapsulation of multiple proteins in virus capsids. *Journal of the American Chemical Society* **131**, 17771-17773 (2009).

39. F. P. Seebeck, K. J. Woycechowsky, W. Zhuang, J. P. Rabe, D. Hilvert, A simple tagging system for protein encapsulation. *Journal of the American Chemical Society* **128**, 4516-4517 (2006).

40. B. Worsdorfer, K. J. Woycechowsky, D. Hilvert, Directed evolution of a protein container. *Science* **331**, 589-592 (2011).

41. T. Inoue *et al.*, Engineering of SV40-based nano-capsules for delivery of heterologous proteins as fusions with the minor capsid proteins VP2/3. *J. Biotechnol.* **134**, 181-192 (2008).

42. T. M. Kozlovska *et al.*, Recombinant rna phage Qβ capsid particles synthesized and self-assembled in *Escherichia coli*. *Gene* **137**, 133-137 (1993).

43. J. D. Fiedler, S. D. Brown, J. L. Lau, M. G. Finn, RNA-directed packaging of enzymes within virus-like particles. *Angew. Chem. Int. Ed. Engl.* **49**, 9648-9651 (2010).

44. W. Earnshaw, S. Casjens, S. C. Harrison, Assembly of head of bacteriophage P22 - X-Ray - diffraction from heads, proheads and related structures *J. Mol. Biol.* **104**, 387-410 (1976).

45. G. C. Lander *et al.*, The structure of an infectious P22 virion shows the signal for headful DNA packaging. *Science* **312**, 1791-1795 (2006).

46. J. Tang *et al.*, Peering down the barrel of a bacteriophage portal: the genome packaging and release valve in p22. *Structure* **19**, 496-502 (2011).

47. M. G. Rossmann, V. B. Rao, *Viral Molecular Machines*. (Springer New York, 2011).

48. Y. Sun *et al.*, Structure of the coat protein-binding domain of the scaffolding protein from a double-stranded DNA virus. *Journal of Molecular Biology* **297**, 1195-1202 (2000).

49. R. Tuma *et al.*, A helical coat protein recognition domain of the bacteriophage P22 scaffolding protein. *J Mol. Biol.* **281**, 81-94 (1998).

50. J. R. Cortines, P. R. Weigele, E. B. Gilcrease, S. R. Casjens, C. M. Teschke, Decoding bacteriophage P22 assembly: identification of two charged residues in scaffolding protein responsible for coat protein interaction. *Virology* **421**, 1-11 (2011).

51. M. H. Parker, S. Casjens, P. E. Prevelige, Jr., Functional domains of bacteriophage P22 scaffolding protein. *J. Mol. Biol.* **281**, 69-79 (1998).

52. B. Greene, J. King, In vitro unfolding/refolding of wild type phage P22 scaffolding protein reveals capsid-binding domain. *Journal of Biological Chemistry* **274**, 16135-16140 (1999).

53. J. Lucon *et al.*, Use of the interior cavity of the P22 capsid for site-specific initiation of atom-transfer radical polymerization with high-density cargo loading. *Nat. Chem.* **4**, 781-788 (2012).

54. D. P. Patterson, K. McCoy, C. Fijen, T. Douglas, Constructing catalytic antimicrobial nanoparticles by encapsulation of hydrogen peroxide producing enzyme inside the P22 VLP. *Journal of Materials Chemistry B* **2**, 5948-5951 (2014).

55. D. P. Patterson, B. Schwarz, R. S. Waters, T. Gedeon, T. Douglas, Encapsulation of an enzyme cascade within the bacteriophage P22 virus-like particle. *ACS Chem. Biol.* **9**, 359-365 (2014).

56. A. O'Neil, P. E. Prevelige, T. Douglas, Stabilizing viral nano-reactors for nerve-agent degradation. *Biomaterials Science* **1**, 881 (2013).

57. D. P. Patterson, B. LaFrance, T. Douglas, Rescuing recombinant proteins by sequestration into the P22 VLP. *Chemical Communications* **49**, 10412-10414 (2013).

58. M. Uchida, B. LaFrance, C. C. Broomell, P. E. Prevelige, T. Douglas, Higher order assembly of virus-like particles (VLPs) mediated by multi-valent protein linkers. *Small* **11**, 1562-1570 (2015).

59. A. O'Neil, C. Reichhardt, B. Johnson, P. E. Prevelige, T. Douglas, Genetically programmed in vivo packaging of protein cargo and its controlled release from bacteriophage P22. *Angew. Chem. Int. Ed. Engl.* **50**, 7425-7428 (2011).

60. A. O'Neil, P. E. Prevelige, G. Basu, T. Douglas, Coconfinement of fluorescent proteins: spatially enforced communication of GFP and mCherry encapsulated within the P22 capsid. *Biomacromolecules* **13**, 3902-3907 (2012).

61. D. P. Patterson, P. E. Prevelige, T. Douglas, Nanoreactors by programmed enzyme encapsulation inside the capsid of the bacteriophage P22. *ACS Nano* **6**, 5000-5009 (2012).

62. D. P. Patterson *et al.*, Virus-like particle nanoreactors: programmed encapsulation of the thermostable CelB glycosidase inside the P22 capsid. *Soft Matter* **8**, 10158-10166 (2012).

63. W. Lubitz, H. Ogata, O. Rudiger, E. Reijerse, Hydrogenases. *Chem. Rev.* **114**, 4081-4148 (2014).

64. K. D. Swanson *et al.*, [FeFe]-hydrogenase oxygen inactivation is initiated at the H cluster 2Fe subcluster. *J Am Chem Soc* **137**, 1809-1816 (2015).

65. J. W. Peters, W. N. Lanzilotta, B. J. Lemon, L. C. Seefeldt, X-ray crystal structure of the Fe-only hydrogenase (CpI) from *Clostridium pasteurianum* to 1.8 angstrom resolution. *Science* **282**, 1853-1858 (1998).

66. S. Shima *et al.*, The crystal structure of [Fe]-hydrogenase reveals the geometry of the Active Site. *Science* **321**, 572-575 (2008).

67. A. Volbeda *et al.*, Crystal Structure of the O_2-tolerant membrane-bound hydrogenase 1 from *Escherichia coli* in complex with its cognate cytochrome b. *Structure* **21**, 184-190 (2013).

68. T. Goris *et al.*, A unique iron-sulfur cluster is crucial for oxygen tolerance of a [NiFe]-hydrogenase. *Nat. Chem. Biol.* **7**, 310-318 (2011).

69. M. J. Lukey *et al.*, Oxygen-tolerant [NiFe]-hydrogenases: the individual and collective importance of supernumerary cysteines at the proximal Fe-S cluster. *J Am Chem Soc* **133**, 16881-16892 (2011).

70. J. A. Cracknell, A. F. Wait, O. Lenz, B. Friedrich, F. A. Armstrong, A kinetic and thermodynamic understanding of O_2 tolerance in [NiFe]-hydrogenases. *Proc. Natl. Acad. Sci. U S A* **106**, 20681-20686 (2009).

71. A. Volbeda *et al.*, X-ray crystallographic and computational studies of the O_2-tolerant [NiFe]-hydrogenase 1 from *Escherichia coli*. *Proc. Natl. Acad. Sci. U S A* **109**, 5305-5310 (2012).

72. A. Volbeda *et al.*, Structure of the [NiFe] hydrogenase active site: evidence for biologically uncommon Fe ligands. *Journal of the American Chemical Society* **118**, 12989-12996 (1996).

73. F. A. Armstrong, S. P. Albracht, [NiFe]-hydrogenases: spectroscopic and electrochemical definition of reactions and intermediates. *Philos Trans A Math Phys Eng Sci* **363**, 937-954; discussion 1035-1040 (2005).

74. R. Hidalgo, P. A. Ash, A. J. Healy, K. A. Vincent, Infrared Spectroscopy During Electrocatalytic Turnover Reveals the Ni-L Active Site State During H2Oxidation by a NiFe Hydrogenase. *Angewandte Chemie* **127**, 7216-7219 (2015).

75. L. Forzi, P. Hellwig, R. K. Thauer, R. G. Sawers, The CO and CN(-) ligands to the active site Fe in [NiFe]-hydrogenase of Escherichia coli have different metabolic origins. *FEBS Lett.* **581**, 3317-3321 (2007).

76. A. J. Pierik *et al.*, Redox properties of the iron-sulfur clusters in activated Fe-hydrogenase from *Desulfovibrio vulgaris* (Hildenborough). *Eur. J. Biochem.* **209**, 63-72 (1992).

77. B. Soboh *et al.*, [NiFe]-hydrogenase maturation in vitro: analysis of the roles of the HybG and HypD accessory proteins1. *Biochem. J.* **464**, 169-177 (2014).

78. B. Friedrich, J. Fritsch, O. Lenz, Oxygen-tolerant hydrogenases in hydrogen-based technologies. *Curr. Opin. Biotechnol.* **22**, 358-364 (2011).

79. L. Forzi, R. G. Sawers, Maturation of [NiFe]-hydrogenases in *Escherichia coli*. *Biometals* **20**, 565-578 (2007).

80. B. J. Murphy, F. Sargent, F. A. Armstrong, Transforming an oxygen-tolerant [NiFe] uptake hydrogenase into a proficient, reversible hydrogen producer. *Energy & Environmental Science* **7**, 1426 (2014).

81. S. G. Mayhew, The redox potential of dithionite and SO^{-2} from equilibrium reactions with flavodoxins, methyl viologen and hydrogen plus hydrogenase. *European Journal of Biochemistry* **85**, 535-547 (1978).

82. M. Adams, L. Mortenson, The physical and catalytic properties of hydrogenase II of *Clostridium pasteurianum*. A comparison with hydrogenase I. *Journal of Biological Chemistry* **259**, 7045-7055 (1984).

83. B. J. Murphy *et al.*, Discovery of dark pH-Dependent H(+) migration in a [NiFe]-hydrogenase and its mechanistic relevance: mobilizing the hydrido ligand of the Ni-C intermediate. *J Am Chem Soc* **137**, 8484-8489 (2015).

84. I. Yacoby *et al.*, Photosynthetic electron partitioning between [FeFe]-hydrogenase and ferredoxin:NADP+-oxidoreductase (FNR) enzymes in vitro. *Proceedings of the National Academy of Sciences* **108**, 9396-9401 (2011).

85. O. A. Zadvornyy *et al.*, Photo-induced H_2 production by [NiFe]-hydrogenase from *T. roseopersicina* covalently linked to a Ru(II) photosensitizer. *J Inorg Biochem* **106**, 151-155 (2012).

86. Z. H. Zhou, D. B. McCarthy, C. M. O'Connor, L. J. Reed, J. K. Stoops, The remarkable structural and functional organization of the eukaryotic pyruvate dehydrogenase complexes. *Proceedings of the National Academy of Sciences* **98**, 14802-14807 (2001).

87. G. C. Cannon *et al.*, Microcompartments in prokaryotes: carboxysomes and related polyhedra. *Applied and Environmental Microbiology* **67**, 5351-5361 (2001).

88. J. M. Shively, F. Ball, D. H. Brown, R. E. Saunders, Functional organelles in prokaryotes: polyhedral inclusions (carboxysomes) of *Thiobacillus neapolitanus*. *Science* **182**, 584-586 (1973).

89. M. R. Badger, CO_2 concentrating mechanisms in cyanobacteria: molecular components, their diversity and evolution. *Journal of Experimental Botany* **54**, 609-622 (2003).

90. X. Zhang *et al.*, Multiple assembly states of lumazine synthase: a model relating catalytic function and molecular assembly. *J. Mol. Biol.* **362**, 753-770 (2006).

91. R. R. Crichton, Structure and function of ferritin. *Angew. Chem. Int. Ed. Engl.* **12**, 57-65 (1973).

92. D. M. Vriezema *et al.*, Self-assembled nanoreactors. *Chem. Rev.* **105**, 1445-1489 (2005).

93. B. Y. Lee *et al.*, Virus-based piezoelectric energy generation. *Nat. Nanotechnol.* **7**, 351-356 (2012).

94. Z. Niu *et al.*, Biological templated synthesis of water-soluble conductive polymeric nanowires. *Nano Lett* **7**, 3729-3733 (2007).

95. K. T. Nam *et al.*, Virus-enabled synthesis and assembly of nanowires for lithium ion battery electrodes. *Science* **312**, 885-888 (2006).

96. M. Li, R. L. Harbron, J. V. Weaver, B. P. Binks, S. Mann, Electrostatically gated membrane permeability in inorganic protocells. *Nat. Chem.* **5**, 529-536 (2013).

97. P. E. Prevelige Jr, D. Thomas, J. King, Scaffolding protein regulates the polymerization of P22 coat subunits into icosahedral shells in vitro. *J. Mol. Biol.* **202**, 743-757 (1988).

98. P. R. Weigele, L. Sampson, D. Winn-Stapley, S. R. Casjens, Molecular genetics of bacteriophage P22 scaffolding protein's functional domains. *J. Mol. Biol.* **348**, 831-844 (2005).

99. M. Frey, Hydrogenases: hydrogen-activating enzymes. *Chembiochem* **3**, 153-160 (2002).

100. G. Buurman, S. Shima, R. K. Thauer, The metal-free hydrogenase from methanogenic archaea: evidence for a bound cofactor. *FEBS Lett.* **485**, 200-204 (2000).

101. S. Krishnan, F. A. Armstrong, Order-of-magnitude enhancement of an enzymatic hydrogen-air fuel cell based on pyrenyl carbon nanostructures. *Chemical Science* **3**, 1015 (2012).

102. N. K. Menon *et al.*, Cloning and sequencing of a putative *Escherichia coli* [NiFe] hydrogenase-1 operon containing six open reading frames. *Journal of Bacteriology* **172**, 1969-1977 (1990).

103. N. K. Menon, J. Robbins, J. C. Wendt, K. T. Shanmugam, A. E. Przybyla, mutational analysis and characterization of the *Escherichia Coli* hya operon,

which encodes [Nife] hydrogenase-1. *Journal of Bacteriology* **173**, 4851-4861 (1991).

104. A. Dubini, How bacteria get energy from hydrogen: a genetic analysis of periplasmic hydrogen oxidation in *Escherichia coli*. *International Journal of Hydrogen Energy* **27**, 1413-1420 (2002).

105. J. Hotz, W. Meier, Vesicle-templated polymer hollow spheres. *Langmuir* **14**, 1031-1036 (1998).

106. S. U. Egelhaaf, P. Schurtenberger, Shape transformations in the lecithin-bile salt system: from cylinders to vesicles. *The Journal of Physical Chemistry* **98**, 8560-8573 (1994).

107. E. C. Hatchikian, N. Forget, V. M. Fernandez, R. Williams, R. Cammack, Further characterization of the [Fe]-hydrogenase from *Desulfovibrio desulfuricans* ATCC 7757. *European Journal of Biochemistry* **209**, 357-365 (1992).

108. T. Lissolo, S. Pulvin, D. Thomas, Reactivation of the hydrogenase from *Desulfovibrio gigas* by hydrogen - influence of redox potential. *Journal of Biological Chemistry* **259**, 11725-11729 (1984).

109. J.-P. Bélaich, M. Bruschi, J.-L. Garcia, *Microbiology and biochemistry of strict anaerobes involved in interspecies hydrogen transfer*. FEMS symposium: no. 54 (New York : Plenum Press, c1990., 1990).

110. J. Y. Kim, B. H. Jo, H. J. Cha, Production of biohydrogen by recombinant expression of [NiFe]-hydrogenase 1 in *Escherichia coli*. *Microb. Cell. Fact.* **9**, 54 (2010).

111. R. G. Sawers, D. H. Boxer, Purification and properties of membrane-bound hydrogenase isoenzyme 1 from anaerobically grown Escherichia coli K12. *Eur. J. Biochem.* **156**, 265-275 (1986).

112. S. Kang, P. E. Prevelige, Jr., Domain study of bacteriophage P22 coat protein and characterization of the capsid lattice transformation by hydrogen/deuterium exchange. *J. Mol. Biol.* **347**, 935-948 (2005).

113. D. J. Hartman, B. P. Surin, N. E. Dixon, N. J. Hoogenraad, P. B. Hoj, Substoichiometric amounts of the molecular chaperones GroEL and GroES prevent thermal denaturation and aggregation of mammalian mitochondrial malate dehydrogenase in vitro. *Proceedings of the National Academy of Sciences* **90**, 2276-2280 (1993).

114. D.-H. Chen *et al.*, Structural basis for scaffolding-mediated assembly and maturation of a dsDNA virus. *Proceedings of the National Academy of Sciences* **108**, 1355-1360 (2011).

115. K. T. Kim, S. A. Meeuwissen, R. J. Nolte, J. C. van Hest, Smart nanocontainers and nanoreactors. *Nanoscale* **2**, 844-858 (2010).

116. A. Volbeda *et al.*, X-ray crystallographic and computational studies of the O_2-tolerant [NiFe]-hydrogenase 1 from *Escherichia coli*. *Proceedings of the National Academy of Sciences*, (2012).

117. J. Simon, R. J. M. van Spanning, D. J. Richardson, The organisation of proton motive and non-proton motive redox loops in prokaryotic respiratory systems. *Biochimica et Biophysica Acta (BBA) - Bioenergetics* **1777**, 1480-1490 (2008).

118. Y. Hirano, S. Kimura, T. Tamada, High-resolution crystal structures of the solubilized domain of porcine cytochrome b_5. *Acta Crystallographica Section D: Biological Crystallography* **71**, 1572-1581 (2015).

119. M. Yamada *et al.*, Elucidations of the Catalytic Cycle of NADH-cytochrome b_5 reductase by x-ray crystallography: new insights into regulation of efficient electron transfer. *J. Mol. Biol.*. **425**, 4295-4306 (2013).

120. E. Arslan, H. Schulz, R. Zufferey, P. Künzler, L. Thöny-Meyer, Overproduction of theBradyrhizobium japonicum c-Type Cytochrome Subunits of the cbb 3 Oxidase in *Escherichia coli*. *Biochemical and Biophysical Research Communications* **251**, 744-747 (1998).

121. A. Yantsevich, A. Gilep, S. Usanov, Mechanism of electron transfer in fusion protein cytochrome b_5—NADH-cytochrome b_5 reductase. *Biochemistry (00062979)* **73**, 1096-1107 (2008).

122. G. v. Jagow, S. Walter, b-Type cytochromes. *Annual Review of Biochemistry* **49**, 281-314 (1980).

123. A. Llauro *et al.*, Cargo-shell coupling governs the stability of individual virus-derived protein cages. *ACS Nano*, (2015) submitted.

124. S. H. W. Scheres, RELION: Implementation of a Bayesian approach to cryo-EM structure determination. *J. Struct. Bio.* **180**, 519-530 (2012).

125. X. Yan, K. A. Dryden, J. Tang, T. S. Baker, Ab initio random model method facilitates 3D reconstruction of icosahedral particles. *J. Struct. Biol.* **157**, 211-225 (2007).

126. Y. Ji *et al.*, A model-based parallel origin and orientation refinement algorithm for cryoTEM and its application to the study of virus structures. *J. Struct. Biol.* **154**, 1-19 (2006).

127. E. F. Pettersen *et al.*, UCSF Chimera--a visualization system for exploratory research and analysis. *J. Comput. Chem.* **25**, 1605-1612 (2004).

128. C. Chen *et al.*, Nanoparticle-templated assembly of viral protein cages. *Nano Lett.* **6**, 611-615 (2006).

129. Y. J. Ma, R. J. M. Nolte, J. Cornelissen, Virus-based nanocarriers for drug delivery. *Adv. Drug Delivery Rev.* **64**, 811-825 (2012).

130. R. de la Rica, H. Matsui, Applications of peptide and protein-based materials in bionanotechnology. *Chem. Soc. Rev.* **39**, 3499-3509 (2010).

131. I. S. Carrico, K. Kirshenbaurn, Nanoparticles - Designer labels for virus coats. *Nat. Nanotechnol.* **4**, 14-15 (2009).

132. K. Kirshenbaum, R. N. Zuckermann, K. A. Dill, Designing polymers that mimic biomolecules. *Curr. Opin. Struct. Biol.* **9**, 530-535 (1999).

133. S. E. Aniagyei *et al.*, Synergistic effects of mutations and nanoparticle templating in the self-assembly of cowpea chlorotic mottle virus capsids. *Nano Lett.* **9**, 393 (2009).

134. Y. Huang *et al.*, Programmable assembly of nanoarchitectures using genetically engineered viruses. *Nano Lett.* **5**, 1429-1434 (2005).

135. E. Royston, A. Ghosh, P. Kofinas, M. T. Harris, J. N. Culver, Self-assembly of virus-structured high surface area nanomaterials and their application as battery electrodes. *Langmuir* **24**, 906-912 (2008).

136. N. Stephanopoulos *et al.*, Immobilization and one-dimensional arrangement of virus capsids with nanoscale precision using DNA origami. *Nano Lett.* **10**, 2714-2720 (2010).

137. Q. Wang, T. Lin, J. E. Johnson, M. Finn, Natural supramolecular building blocks: cysteine-added mutants of cowpea mosaic virus. *Chem. Biol.* **9**, 813-819 (2002).

138. P. J. Yoo *et al.*, Controlling surface mobility in interdiffusing polyelectrolyte multilayers. *ACS Nano* **2**, 561-571 (2008).

139. M. A. Kostiainen, P. Hiekkataipale, Á. Jose, R. J. Nolte, J. J. Cornelissen, Electrostatic self-assembly of virus–polymer complexes. *J. Mater. Chem.* **21**, 2112-2117 (2011).

140. M. Uchida *et al.*, Biological Containers: Protein Cages as Multifunctional Nanoplatforms. *Advanced Materials* **19**, 1025-1042 (2007).

141. S. L. Capehart, M. P. Coyle, J. E. Glasgow, M. B. Francis, Controlled Integration of Gold Nanoparticles and Organic Fluorophores Using Synthetically Modified MS2 Viral Capsids. *J. Am. Chem. Soc.*, (2013).

142. D. P. Patterson, P. E. Prevelige, T. Douglas, Nanoreactors by Programmed Enzyme Encapsulation Inside the Capsid of the Bacteriophage P22. *ACS Nano* **6**, 5000-5009 (2012).

143. S. Kang, G. C. Lander, J. E. Johnson, P. E. Prevelige, Development of bacteriophage P22 as a platform for molecular display: genetic and chemical modifications of the procapsid exterior surface. *Chembiochem* **9**, 514-518 (2008).

144. S. Kang *et al.*, Implementation of P22 Viral Capsids as Nanoplatforms. *Biomacromolecules* **11**, 2804-2809 (2010).

145. D. H. Chen *et al.*, Structural basis for scaffolding-mediated assembly and maturation of a dsDNA virus. *Proc. Natl. Acad. Sci. U. S. A.* **108**, 1355-1360 (2011).

146. K. N. Parent *et al.*, Cryo-reconstructions of P22 polyheads suggest that phage assembly is nucleated by trimeric interactions among coat proteins. *Phys. Biol.* **7**, (2010).

147. A. Altunbas, D. J. Pochan, in *Peptide-Based Materials*. (Springer, 2012), pp. 135-167.

148. M. Pechar *et al.*, Coiled Coil Peptides as Universal Linkers for the Attachment of Recombinant Proteins to Polymer Therapeutics. *Biomacromolecules* **12**, 3645-3655 (2011).

149. I. J. Minten, R. J. M. Nolte, J. Cornelissen, Complex assembly behavior during the encapsulation of green fluorescent protein analogs in virus derived protein capsules. *Macromolecular Bioscience* **10**, 539-545 (2010).

150. D. P. Patterson, A. M. Desai, M. M. B. Holl, E. N. G. Marsh, Evaluation of a symmetry-based strategy for assembling protein complexes. *Rsc Advances* **1**, 1004-1012 (2011).

151. J. Kopecek, J. Y. Yang, Smart self-assembled hybrid hydrogel biomaterials. *Angew. Chem., Int. Ed.* **51**, 7396-7417 (2012).

152. J. M. Fletcher *et al.*, Self-assembling cages from coiled-coil peptide modules. *Science* **340**, 595-599 (2013).

153. B. Apostolovic, M. Danial, H. A. Klok, Coiled coils: attractive protein folding motifs for the fabrication of self-assembled, responsive and bioactive materials. *Chem. Soc. Rev.* **39**, 3541-3575 (2010).

154. A. Frey, B. Meckelein, D. Externest, M. A. Schmidt, A stable and highly sensitive 3, 3′, 5, 5′-tetramethylbenzidine-based substrate reagent for enzyme-linked immunosorbent assays. *J. Immunol. Methods* **233**, 47-56 (2000).

155. M. Pechar, R. Pola, The coiled coil motif in polymer drug delivery systems. *Biotechnol. Adv.* **31**, 90-96 (2013).

156. E. F. Pettersen *et al.*, UCSF chimera - A visualization system for exploratory research and analysis. *J. Comput. Chem.* **25**, 1605-1612 (2004).

157. R. D. Kirsch, E. Joly, An improved PCR-mutagenesis strategy for two-site mutagenesis or sequence swapping between related genes. *Nucleic Acids Res.* **26**, 1848-1850 (1998).

158. C. Pinske, J. S. McDowall, F. Sargent, R. G. Sawers, Analysis of hydrogenase 1 levels reveals an intimate link between carbon and hydrogen metabolism in Escherichia coli K-12. *Microbiology* **158**, 856-868 (2012).

159. B. J. Murphy, F. Sargent, F. A. Armstrong, Transforming an oxygen-tolerant [NiFe] uptake hydrogenase into a proficient, reversible hydrogen producer. *Energy & Environmental Science* **7**, 1426-1433 (2014).

160. L. Mortenson, J. Chen, J. Neilands, Microbial Iron Metabolism. *Academic Press, New York*, 231-282 (1974).

161. Z. X. Zhang *et al.*, Visualization of the maturation transition in bacteriophage P22 by electron cryomicroscopy. *J. Mol. Biol.* **297**, 615-626 (2000).

162. D. H. Chen *et al.*, Structural basis for scaffolding-mediated assembly and maturation of a dsDNA virus. *Proc. Natl. Acad. Sci. U S A* **108**, 1355-1360 (2011).

163. A. Zlotnick, M. M. Suhanoysky, C. M. Teschke, The energetic contributions of scaffolding and coat proteins to the assembly of bacteriophage procapsids. *Virology* **428**, 64-69 (2012).

164. B. L. Johnson, Monitoring protien cage nanopaticle morphology for applications in medicines and materials. Montana State University, Bozeman, MT (2011).